Experimental Study of the Wake Flow and Thrust Coefficient of Porous Actuator Discs

Sindre Øye

Master's Thesis in Ocean Technology

University of Bergen

Department of Physics and Technology

June 2022

Preface

This master's thesis is written at the Department of Physics and Technology (IFT) at the University of Bergen (UiB). The thesis is part of the two-year master's program in Ocean Technology – Marine installations, which is a collaborative master's program between the University of Bergen (UiB) and the Western Norway University of Applied Sciences (HVL).

Several people have contributed to this master's thesis. I would therefore like to extend my gratitude towards supervisors, lab engineers and fellow students.

First and foremost, I would like to thank my supervisors, David Roger Lande-Sudall, Jan Michael Simon Bartl and Harald Totland, for many constructive discussions and feedback and for always being available when I needed guidance.

Furthermore, I would like to thank the lab engineers Robert Larsson, Harald Moen, Kjetil Gravelsæter and Nafez Ardestani from HVL for guidance in the workshop at HVL, for assisting with welding and machining of parts, and for helping with assembly and disassembly of the experimental setup in the MarinLab towing tank.

Finally, I would like to thank my fellow students from HTEK for interesting and enlightening discussions during the last year. Special thanks to HTEK student, Morten Skoland, for helping with installation and adjustment of equipment during the experimental testing in the MarinLab.

Abstract

Understanding turbine loads and flows around turbines is essential for maximising power output and designing suitable support structures. In laboratory turbine investigations, actuator discs are commonly used to represent rotating turbine rotors due to the complexity of constructing and controlling model turbines. Further research on actuator discs is needed, as it is still being established how well the wake of a rotating turbine can be represented by using these discs.

In this thesis, experimental investigations of two porous actuator discs with diameters of 0.7 m and 0.2 m have been conducted in the MarinLab towing tank at Høgskulen på Vestlandet under laminar inflow conditions. The disc setups are different, as only the largest disc is mounted with a nacelle. The aim is to assess whether actuator discs can be used to represent the wake of a turbine. Furthermore, tower, nacelle and potential blockage effects are investigated. Measurement equipment such as an acoustic Doppler velocimeter and two strain gauge load cells are used to measure the flow velocities in the wake and the axial force on the discs, respectively. These data are processed to create profiles of velocity deficit and turbulence kinetic energy, and to determine the thrust coefficients of the actuator discs.

A slightly higher thrust coefficient was found for the largest disc, probably due to its larger blockage ratio. The half-wake width development downstream of the discs was shown to be similar except at the furthest downstream position, where the wake expansion of the largest disc was constrained by the tank side walls. The results from the conducted experiments indicate that the velocity deficit in the far wake of actuator discs follows a self-similar Gaussian curve if the disc wake is unconstrained by bounding surfaces.

Recirculation regions were observed in the near wake of both actuator discs, which does not correspond with a turbine wake. Vertical velocity profiles were shown not to be symmetric around the disc axis, as expected due to the presence of a tower. A faster wake recovery was observed for the largest disc, which was apparent both from a smaller velocity deficit in the wake and a faster breakdown of the disc edge vortices compared to the other disc. The faster wake recovery could be associated with the significantly higher turbulence level observed in the near wake of the largest disc, likely caused by the nacelle. The results of this thesis indicate that actuator discs can effectively represent the far wake region of a rotating turbine.

Sammendrag

Å forstå turbinbelastninger og strømninger rundt turbiner er avgjørende for å maksimere energiuttaket og utforme passende støttestrukturer. I laboratorieturbinundersøkelser brukes ofte aktuatordisker for å representere roterende turbinrotorer på grunn av kompleksiteten ved å konstruere og kontrollere modellturbiner. Videre forskning på aktuatordisker er nødvendig, siden det fortsatt er usikkerhet med tanke på hvor godt vaken til en roterende turbin kan representeres ved bruk av slike disker.

I denne oppgaven er det utført eksperimentelle undersøkelser av to porøse aktuatordisker med diametere på 0.7 m og 0.2 m i MarinLab slepetanken ved Høgskulen på Vestlandet under laminære innstrømningsforhold. Diskoppsettene er forskjellige, da kun den største disken er montert med en nacelle. Målet er å vurdere om aktuatordisker kan brukes til å representere vaken til en turbin. Videre undersøkes tårn-, nacelle- og potensielle blokkeringseffekter. Måleutstyr som en akustisk Doppler hastighetsmåler og to strekklapp-lastceller brukes til å måle henholdsvis strømningshastighetene i vaken og aksialkraften på diskene. Disse dataene prosesseres for å lage profiler for hastighetsunderskudd og turbulent kinetisk energi, og for å bestemme skyvekraftskoeffisientene til aktuatordiskene.

En noe høyere skyvekraftskoeffisient ble funnet for den største disken, sannsynligvis på grunn av dens større blokkeringsforhold. Utviklingen av halvvakebredden nedstrøms for diskene ble vist å være lik bortsett fra ved den lengste nedstrømsposisjonen, hvor vakeekspansjonen til den største disken ble begrenset av tanksideveggene. Resultatene fra de utførte eksperimentene indikerer at hastighetsunderskuddet i fjernvaken til aktuatordisker følger en egenlik Gauss-kurve hvis vaken til disken er ubegrenset av avgrensende flater.

Resirkulasjonsregioner ble observert i nærvaken til begge aktuatordiskene, noe som ikke samsvarer med en turbinvake. Vertikale hastighetsprofiler ble vist å ikke være symmetriske rundt diskaksen, som forventet på grunn av tilstedeværelsen av et tårn. En raskere vakegjenoppretting ble observert for den største disken, noe som viste seg både fra et lavere hastighetsunderskudd i vaken og en raskere nedbrytning av disk-kantvirvlene sammenlignet med den andre disken. Den raskere vakegjenopprettingen kan være assosiert med det betydelig høyere turbulensnivået som ble observert i nærvaken til den største disken, sannsynligvis forårsaket av nacellen. Resultatene fra denne oppgaven indikerer at aktuatordisker effektivt kan representere fjernvaken til en roterende turbin.

Contents

List of Figures

List of Tables

1 Introduction

1.1 Background

Global warming is an increasing threat to the world that can only be managed through a collective effort. The Paris Agreement [1] ensured commitment from all involved countries to reducing greenhouse gas emissions substantially so that the global average temperature increase is limited to well below 2 °C above pre-industrial levels.

The International Energy Agency (IEA) [2] reported a growth in global energy consumption of 2.3% in 2018, nearly twice the average growth rate since 2010. A doubling of the global energy demand is expected over the next decades as the population of the world increases [3]. Today, renewable energy production is not sufficient to solely cover the high energy demand of the world. The "Renewables 2019 Global Status Report" [4] published by REN21 states that renewable energy accounted for 18.1% of the total final energy consumption worldwide in 2017. Further development in the renewable technologies is therefore essential in the transition from fossil fuels to renewable energy. In this transition, wind energy is expected to have a significant role [5].

Wind turbines extract kinetic energy from wind and converts it into electricity. Wind energy is one of the fastest-growing renewable energy sources worldwide [6]. The total global wind power capacity was doubled over the period from 2014 to 2020, reaching a total global capacity of 743 GW in 2020 [7]. The Global Wind Energy Council (GWEC) [8] estimates an additional wind power capacity of 557 GW over the period from 2021 to 2026, i.e., more than 110 GW each year. In order to stay on the path towards net-zero emissions by 2050, this growth needs to quadruple by the end of the decade according to GWEC [8].

Turbines can also be used to generate power from the tides. However, energy production from tidal turbines is not as established as wind turbines. Tidal energy represents a small share of the renewable energy market [7]. Currently, the cost of tidal energy is relatively high compared to other renewables, such as wind and solar. However, tidal energy is steadily advancing towards commercialisation as costs are reduced. Further research on tidal turbines is necessary if this energy source is to become an important part of the energy system of the future. A study by Lande-Sudall [9] investigated co-location of offshore wind and tidal stream turbines as way to

increase the power output and reduce the cost of electricity compared to either technology alone.

1.2 Need for further research

Understanding turbine loads and flows around turbines is essential for maximising power output and designing suitable support structures. This is particularly important in regard to wind farms and tidal stream arrays, where interactions between turbines affect the overall efficiency of the farm and the loadings on each turbine [10]. The wake flow of turbines, which is characterised by a velocity deficit and an increased turbulence level, plays a major role in this context. Although extensive research has been devoted to this topic, further research is needed to improve this knowledge.

Excellent predictions of turbine loads and wakes can be achieved through numerical modelling tools, such as computational fluid dynamics (CFD) and blade element momentum (BEM) [11]. However, these results have no value without validation against real data. Conducting experiments on full scale turbines is often infeasible. As such, turbine investigations are generally performed in wind tunnels or water tanks with downscaled model turbines. Various conditions, such as incoming flow velocity, turbulence level and blockage, affect the loadings and performance of turbines [12]. Conducting experiments in the well-controlled environment of a wind tunnel or a water tank enables more accurate investigations of the effects of such conditions.

Actuator discs are commonly used in laboratory experiments to represent rotating turbine rotors due to the complexity of constructing and controlling model turbines [12]. It is still being established how well these discs are able to capture the characteristics of a rotating turbine. Therefore, more research on actuator discs is needed. Generally, actuator discs are shown to effectively represent the mean flow characteristics of turbines in the far wake region. In the near wake, discrepancies are found between discs and turbines, particularly in the areas which are strongly affected by the turbine rotation. An experimental study by Helvig et al. [12] found that actuator discs can capture mean flow properties of rotating turbines adequately, however the discs are not suited for capturing instantaneous phenomena in the wake.

Multiple studies have demonstrated that the power and thrust coefficients of turbines are significantly increased when blockage ratios, i.e., the ratio of turbine swept area to cross-sectional area of a confined channel, exceed 5-10% [13-15]. The blockage ratio of the two actuator discs regarded in this thesis, with diameters of 0.7 m and 0.2 m, is 5.8% and 0.5%, respectively. Accordingly, blockage effects could potentially be significant for the 0.7 m diameter disc, and so this will be investigated.

A three-bladed horizontal-axis hydrokinetic turbine with a diameter of 0.7 m is under development at the Western Norway University of Applied Sciences (HVL). Experimental data from the 0.7 m diameter actuator disc regarded in this thesis will therefore be valuable for comparison with this turbine to assess how well the actuator disc represents the turbine. The actuator disc experiments will also reveal whether blockage effects should be accounted for when conducting experiments with the HVL turbine in the future.

1.3 Aim of thesis

This thesis will investigate the wake flow and thrust coefficient of two different actuator disc setups through physical testing in the MarinLab towing tank at HVL. The aim is to assess whether porous actuator discs can be used to represent the wake of a turbine. Herein, the disc diameter and its effect on the wake flow, will be investigated. Specifically, tower, nacelle and potential blockage effects are studied.

2 Theory

2.1 One-dimensional momentum theory

One-dimensional momentum theory is a model for investigating the effects when fluid passes through a turbine rotor [16]. In this model, the turbine rotor is represented by an ideal actuator disc, which simplifies the calculations considerably. Actuator discs have no blades and no rotation, as opposed to turbine rotors. Therefore, the wake of a disc will have no tip or root vortices caused by vortex shedding from blades, and the wake will experience no rotation. Actuator discs are further described in chapter 2.2. Using an ideal disc representation of a turbine means that the following assumptions must be made for the model to be valid:

- The fluid flow is homogenous, frictionless, steady and incompressible.
- The thrust over the disc/rotor area is uniform.
- The flow outside the stream tube is not affected by any other forces.
- There is no rotation in the wake.
- Both far upstream and far downstream of the disc/rotor, the static pressure is equal to the undisturbed ambient static pressure.

Applying one-dimensional momentum theory, the power output and thrust force of a turbine rotor can be estimated using equations that will be derived in this chapter.

Effects on flow when passing through an actuator disc

Figure 1 [17] illustrates the effects of an actuator disc on the fluid flow as it passes through the disc. The flow experiences a velocity deficit as is passes through the disc. The flow velocity is reduced from the far upstream flow velocity, U_0, to the velocity in the disc plane, U_D, and is further reduced to the wake velocity, U_W, downstream of the disc. A pressure drop across the disc can also be observed in figure 1. The pressure far upstream of the disc, p_0, increases to p_D^+ as the flow approaches the disc. When the flow passes through the disc, there is a significant pressure drop, Δp, from p_D^+ to p_D^-. As the flow moves further downstream of the disc, the pressure increases until it recovers its original value, p_0, far downstream of the disc.

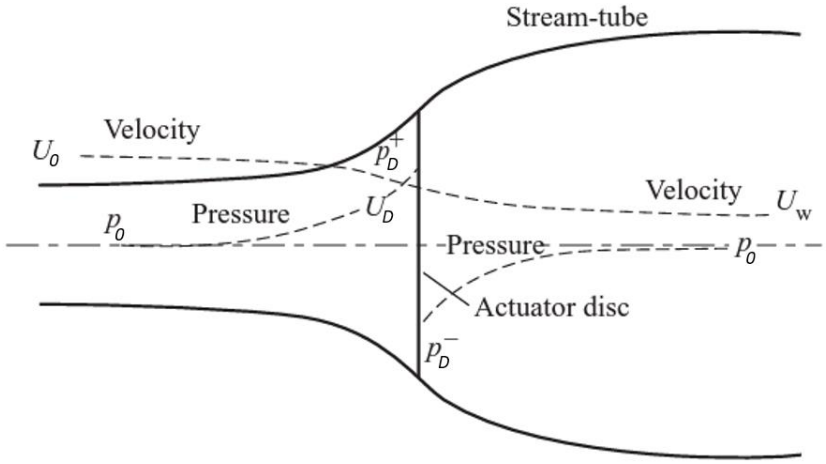

Figure 1: Representation of the effects when fluid passes an actuator disc [17].

The assumption of a frictionless, steady and incompressible flow, unaffected by any forces outside the stream tube, enables the Bernoulli equation to be applied separately to the upstream and downstream sections of the stream tube [17].

Thus, the following equation can be derived for the upstream section of the stream tube:

$$\frac{1}{2}\rho U_0^2 + p_0 = \frac{1}{2}\rho U_D^2 + p_D^+ \tag{2.1}$$

where ρ is the density of the fluid.

Similarly, for the downstream section:

$$\frac{1}{2}\rho U_D^2 + p_D^- = \frac{1}{2}\rho U_W^2 + p_0 \tag{2.2}$$

Combining equations (2.1) and (2.2) yields the pressure drop across the disc, Δp:

$$\Delta p = p_D^+ - p_D^- = \frac{1}{2}\rho(U_0^2 - U_W^2) \tag{2.3}$$

The assumption of a steady flow means that conservation of mass applies for the stream tube. Thus, the mass flow rate, $\dot{m}$, must be equal in all the different sections of the stream tube, which yields:

$$\dot{m} = \rho A_0 U_0 = \rho A_D U_D = \rho A_W U_W \tag{2.4}$$

where A_0, A_D and A_W are the cross-sectional areas of the stream tube upstream, in the disc plane and downstream, respectively. Notably, A_D is the area of the disc and is given by $A_D=\pi R^2$.

Dividing equation (2.4) by the fluid density, ρ, yields:

$$A_0 U_0 = A_D U_D = A_W U_W \tag{2.5}$$

Equation (2.5) explains why the cross-sectional area of the stream tube is larger downstream of the disc compared to upstream, as illustrated in figure 1. Due to the reduced flow velocity downstream of the disc, the cross-sectional area of the stream tube must be larger for the mass flow rate to be constant.

The principle of momentum conservation can also be applied, and yields:

$$\rho A_0 U_0^2 = \rho A_W U_W^2 + \Delta p A_D = \rho A_W U_W^2 + \frac{1}{2}\rho A_D (U_0^2 - U_W^2) \tag{2.6}$$

The flow velocity in the disc plane, U_D, can be found by dividing equation (2.6) with the mass flow rate expressions from equation (2.4), which yields:

$$U_0 = U_W + \frac{1}{2}\frac{U_0^2 - U_W^2}{U_D} \rightarrow U_D = \frac{1}{2}(U_0 + U_W) \tag{2.7}$$

The axial induction factor, a, is a parameter describing the fractional decrease in fluid velocity between the far upstream position and the disc plane [16]. Thus, the axial induction factor is given by

$$a = \frac{U_0 - U_D}{U_0} \tag{2.8}$$

The flow velocity in the disc plane, U_D, can be expressed by rearranging equation (2.8) as follows:

$$U_D = U_0(1 - a) \tag{2.9}$$

By combining equations (2.9) and (2.7) the wake velocity, U_W, can be expressed as:

$$U_W = U_0(1 - 2a) \tag{2.10}$$

By evaluating equation (2.10), the wake velocity, U_W, will be zero if a = 0.5. The momentum theory, as described in this chapter, can only be applied if the wake velocity is greater than zero, i.e., if $a < 0.5$. An empirical modification has to be made if $a \geq 0.5$ [17]. This empirical modification will not be further described in this thesis.

Thrust and power

Due to the pressure drop across the disc, Δp, given by equation (2.3), a force acts on the disc in the streamwise direction [17]. This force is called the thrust force, F_T, and can be expressed as shown in equation (2.11):

$$F_T = \Delta p A_D = \frac{1}{2}\rho(U_0^2 - U_W^2)A_D \tag{2.11}$$

By combining equations (2.10) and (2.11) the thrust force, F_T, can be expressed accordingly:

$$F_T = \frac{1}{2}\rho A_D U_0^2(4a(1-a)) \tag{2.12}$$

The thrust can be characterised by a non-dimensional parameter called the thrust coefficient, C_T, given by

$$C_T = \frac{F_T}{F_{dynamic}} = \frac{\frac{1}{2}\rho A_D U_0^2(4a(1-a))}{\frac{1}{2}\rho A_D U_0^2} = 4a(1-a) \tag{2.13}$$

where $F_{dynamic}$ is the dynamic force of the fluid flow, in the absence of the actuator disc, for a cross-section equal to the area of the disc, A_D [16].

By combining equations (2.12) and (2.13) the thrust force, F_T, can be expressed in terms of the thrust coefficient, C_T:

$$F_T = \frac{1}{2}\rho A_D U_0^2 C_T \tag{2.14}$$

The power extraction of the disc from the fluid flow is the work done by the thrust force, F_T, on the flow [17]. Thus, the power extraction of the disc, P, is given by

$$P = F_T U_D = \frac{1}{2}\rho A_D U_0^3 C_T(1-a) \tag{2.15}$$

Furthermore, the power extraction of the disc can be expressed as the non-dimensional parameter power coefficient, C_P, expressed as

$$C_P = \frac{P}{P_{available}} = \frac{\frac{1}{2}\rho A_D U_0^3 C_T(1-a)}{\frac{1}{2}\rho A_D U_0^3} = C_T(1-a) = 4a(1-a)^2 \tag{2.16}$$

where $P_{available}$ is the available power in the fluid flow, in the absence of the actuator disc, for a cross-section equal to the area of the disc, A_D.

By combining equations (2.15) and (2.16) the power extraction of the disc, P, can be expressed in terms of the power coefficient, C_P:

$$P = \frac{1}{2}\rho A_D U_0^3 C_P \tag{2.17}$$

The aim when designing a turbine for power production is a large power coefficient, C_P, as this means that a large portion of the available kinetic energy in the flowing fluid is converted into

mechanical energy turning the turbine rotor. The theoretical maximum value of C_P for an ideal turbine can be found by differentiating C_P with respect to the axial induction factor, a, and setting this derivative equal to zero:

$$\frac{dC_P}{da} = 4(1-a)(1-3a) = 0 \tag{2.18}$$

Solving equation (2.18) yields a = [1, 1/3]. The maximum C_P will not occur when a = 1, as this yields a C_P equal to zero.

Thus, the maximum power coefficient, $C_{P_{max}}$, is found when a = 1/3, which yields:

$$C_{P_{max}} = \frac{16}{27} = 0.593 \tag{2.19}$$

The theoretical maximum C_P for an ideal turbine is therefore 0.593. Accordingly, a maximum of 59.3% of the kinetic energy from the flowing fluid can be converted into mechanical energy turning the turbine rotor. This maximum value is referred to as the Betz limit.

In figure 2, the power and thrust coefficients are plotted as a function of the axial induction factor, a, based on equations (2.16) and (2.13), respectively. The dashed sections of the curves illustrate the circumstances where momentum theory is no longer valid, i.e., when $a \geq 0.5$.

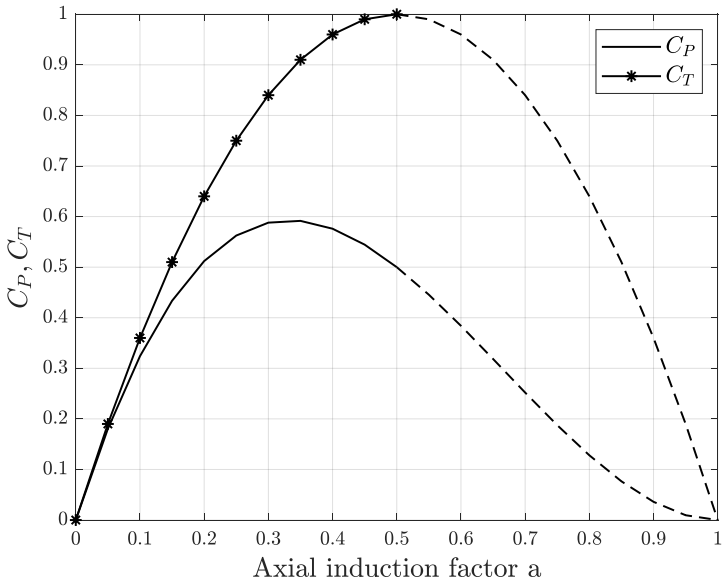

Figure 2: Variation of power and thrust coefficients with axial induction factor, a. The dashed sections of the two curves indicate where the momentum theory is no longer valid, i.e., when $a \geq 0.5$.

2.2 Actuator disc

Conducting field tests of turbines is expensive, and the test conditions are impossible to fully control [12]. Performing experiments on downscaled model turbines in wind tunnels or water tanks in laboratories is cost-beneficial, whilst allowing investigations in a controlled environment. Thus, the of effect of conditions, such as incoming flow velocity, blockage and turbulence level, on the performance, loadings and wake of a turbine can be studied more accurately.

Downscaled model turbine investigations in laboratories are commonly simplified by using static actuator discs to represent turbine rotors. Actuator discs are cheaper and easier to manufacture, and generally less susceptible to damage, compared to a turbine rotor with rotating parts. Still, there are uncertainties regarding how well the behaviour of rotating turbines is represented by actuator discs, and to what extent the geometries of the discs influence the results.

Notably, the axial force on an actuator disc, resulting from the incoming fluid flow, is referred to both as a drag force and a thrust force in literature. In this thesis, the drag force from the discs will be referred to as a thrust force, as the discs represent a turbine rotor where thrust is the more appropriate term.

The design of an actuator disc is usually made to resemble a specific turbine rotor by matching both the diameter and thrust coefficient of the rotor. There are, however, no standards for actuator disc design. Uniformity and comparability between experimental investigations of actuator discs would be significantly improved by developing a standard actuator disc design which is able to produce the desired wake.

2.2.1 Comparison of actuator disc and free rotating wind turbine

In the search of an actuator disc capable of representing a turbine rotor, various disc designs have been developed. A study by Helvig et al. [12] investigated the comparability between a well-matched actuator disc and a two-bladed rotating turbine through experiments in a wind tunnel. Two different actuator disc designs with various solidities were compared to the turbine rotor in terms of thrust coefficient, mean velocity and mean vorticity in the wake. In addition, a solid disc was tested as a reference. One of the disc designs had uniform circular holes and

was tested with solidities of 40% and 60%. The other disc design had nonuniform trapezoidal holes with a greater solidity near the centre, and was tested with solidities of 35%, 40% and 60%.

A significant recirculation area, i.e., an area of reversed flow, was observed in the wake of both the solid disc and the 60% solidity circular holed disc. These areas of reversed flow were not found in the wake of the rotating turbine. The other discs were also shown to have a recirculation region, however, this region was only present less than one disc diameter downstream. A reasonable explanation for the reversed flow observed behind the discs was found in the upstream measurements which showed that all the discs imposed more of a blockage to the incoming flow compared to the turbine.

Increased intensity of vorticity was observed along the edges of the wake of both the turbine and the actuator discs. However, the areas of increased vorticity were more significant for the high solidity discs, covering large parts of the wake. The high solidity discs were therefore not representative of the turbine. The low solidity discs differed slightly from the turbine by experiencing high intensity vorticity in the immediate wake. This was likely caused by interaction between flow jets passing through the holes in the discs.

As a result of the measurements, Helvig et al. concluded that the trapezoidal holed disc with a 35% solidity was the closest match to the two-bladed turbine in regard to thrust coefficient and mean wake vorticity, as well as showing good agreement in terms of mean velocity. This disc was therefore studied in further detail to see how well the disc represents the instantaneous flow phenomena in the wake of the turbine. These analyses showed that there were instantaneous tip vortices present in the wake of the turbine which were not found in the wake of the disc. In addition, high intensity swirl was observed in the near wake of the disc, in contrast to the turbine. This was believed to be caused by mixing of flow jets through the holes in the disc.

Helvig et al. therefore concluded that actuator discs are capable of capturing mean flow properties of a rotating turbine adequately, however the discs are not suited for capturing instantaneous phenomena in the wake. In addition, the measurements showed that the immediate wake, i.e., less than 1D downstream, and the upstream blockage effects of the actuator discs are not representative of a rotating turbine.

The two actuator discs regarded in this thesis are trapezoidal holed discs with a solidity of 57%, designed to emulate the velocity distribution behind a three-bladed rotating turbine. These discs are further described in chapter 3.1.2. Helvig et al. [12] measured a thrust coefficient of

approximately 1.10 for the 60% solidity trapezoidal holed disc, and observed a recirculation area that was only present less than 1D downstream. Due to the slightly higher solidity of the disc investigated by Helvig et al. compared to the discs regarded in the present thesis, the thrust coefficients obtained through this thesis are expected to be lower than 1.10. This is also supported by experimental investigations performed by Hansen et al. [18] in the MarinLab towing tank on a disc with a design and solidity identical to the discs regarded in this thesis. Hansen et al. measured the thrust coefficient of the disc to be 0.88. The results from the experiments of Helvig et al [12] and Hansen et al. [18] will therefore be interesting for comparison with the results obtained through the experiments of this thesis.

2.2.2 Reynolds independence for thrust coefficient

In figure 3, the drag coefficient of circular and square plates is plotted as a function of Reynolds number [19]. The figure shows that drag coefficients are independent of the Reynolds number approximately when Re>1000. Results from several experimental investigations of porous actuator discs, such as studies conducted by Helvig et al. [12] and Hansen et al. [18], validates Reynolds independence for actuator discs. The theory of Reynolds independence will therefore also be investigated through the measurements of thrust coefficients for the porous actuator discs regarded in this thesis.

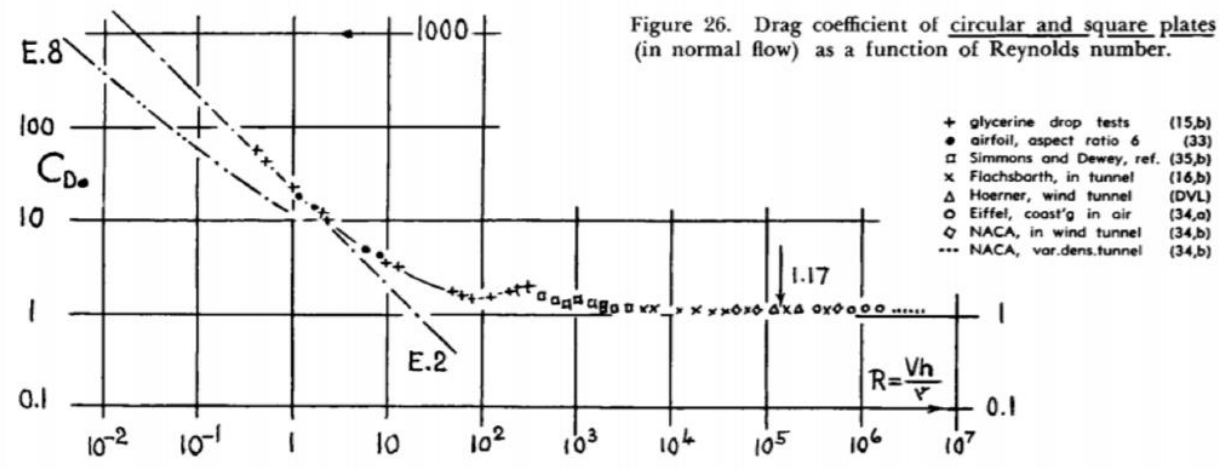

Figure 3: Drag coefficient as a function of Reynolds number for circular and square plates [19].

2.3 Turbine wakes

It is important to have a thorough understanding of the wake effects occurring downstream of a turbine, especially in terms of installing turbines within a wind farm. In wind farms, turbines are usually arranged in several rows. Therefore, the turbines located downstream of the first-row turbines will be influenced by the wakes of the turbines located upstream relative to them.

A turbine extracts energy from the flowing fluid, meaning that the fluid is lower on energy downstream of the turbine. Accordingly, there is less energy available for a downstream turbine to extract. In addition, there will be increased levels of turbulence in the wake of a turbine which can impose fatigue loads on downstream turbines [20]. Understanding turbine wake effects is therefore essential in order to optimise wind farms, i.e., arranging turbines in a way that maximises power output, whilst considering turbine lifetime and need for maintenance.

2.3.1 Near wake

The near wake of a turbine is a region in the wake typically defined between 1-3 rotor diameters downstream of the turbine [21, 22]. As described through the one-dimensional momentum theory in chapter 2.1, the turbine rotor causes a velocity deficit to the fluid flow as it passes through the rotor, and there is a pressure drop across the rotor. In the immediate wake, whilst moving downstream, the velocity inside the wake continues decreasing and the pressure increases until the pressure in the wake recovers to the ambient pressure [21]. At this point, the maximum velocity deficit is found.

Due to the difference in velocity between the fluid inside and outside the wake, a shear layer is formed [23]. The one-dimensional momentum theory is based on the assumption that the flow within the wake is unaffected by the free stream flow outside the wake. This is not the case for an actual turbine. In the region of the wake where the pressure is recovering, as described above, turbulent mixing will occur, driven by the pressure and velocity gradients between the low-pressure flow within the wake and the ambient pressure flow outside the wake [9]. Thus, the low-velocity flow in the wake is mixed with the free stream flow, i.e., momentum is transferred into the wake, causing the wake flow to recover towards the free stream velocity whilst moving further downstream of the turbine [23].

When the pressure in the wake has recovered to the ambient pressure, the mixing of momentum is driven by turbulent diffusion [21]. A higher ambient turbulence level yields a faster recovery of the wake. Turbulent diffusion causes the shear layer to expand with downstream distance. When the shear layer has expanded so much that it reaches the wake axis, the end of the near wake region is reached. The end of the near wake is illustrated with an orange vertical line in figure 4.

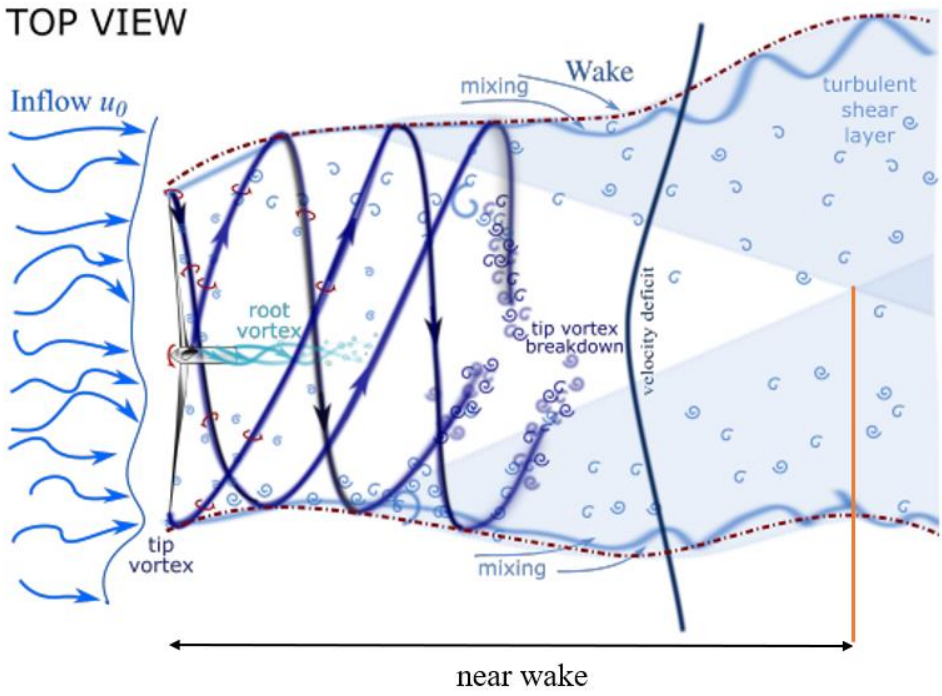

Figure 4: Sketch of the development of the turbulent wake of a turbine, showing the near wake [24].

Both tip and root vortices are shed from the blades of a rotating turbine, and will be present in the near wake, as illustrated in figure 4 [24]. The tip vortices, which are highly turbulent, surround the wake and follow a helical path, before breaking down a certain distance downstream of the rotor. The root vortices, however, are less stable and break down close to the turbine rotor.

The flow passing through a turbine rotor exerts torque on the turbine blades [23]. Thus, a reaction torque acts on the flow, leading to a rotation of the wake in the opposite direction of the turbine rotation.

Static actuator discs are used to represent a turbine rotor in the experiments regarded in this thesis. Accordingly, no tip or root vortices will be present in the wakes, and the wakes will experience no rotation. The nacelle and tower of a turbine induces mechanical turbulence in the wake [23]. This turbulence is of high frequency and decays relatively fast. Nacelle-induced

turbulence will be an interesting aspect regarding the wake investigations of this thesis, as only one of the discs is mounted with a nacelle.

2.3.2 Far wake

The near wake is followed by a transition region which leads to the far wake, as shown in figure 5 [23].

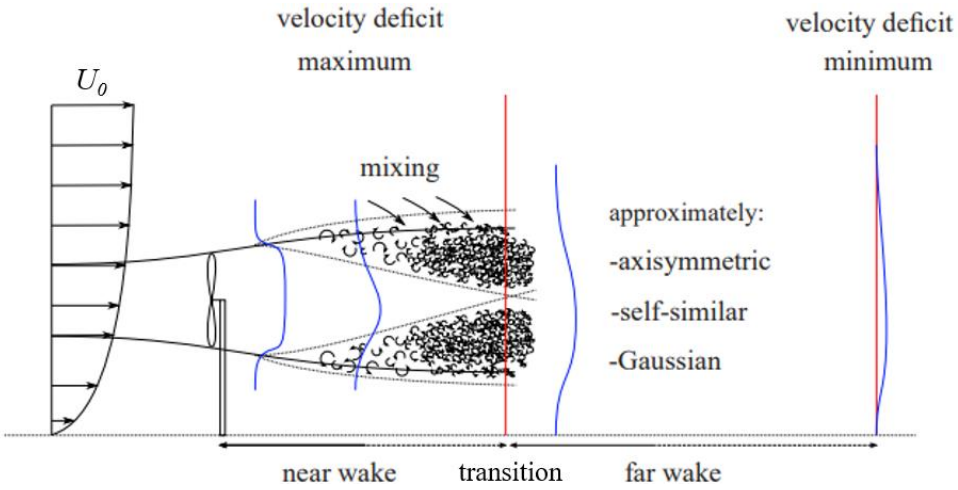

Figure 5: Sketch of the wake of a turbine [23]. The blue curves illustrate the velocity deficit profiles.

In the far wake region, the wake is completely developed, and the cross-section profiles of both the velocity deficit and turbulence intensity are assumed to be axisymmetric and have self-similar distributions [21]. The velocity deficit, ΔU, can be defined as

$$\Delta U = U_0 - U_W \tag{2.20}$$

where U_0 is the free stream velocity and U_W is the fluid velocity in the wake. The scaled variable of wake width, δ, can be expressed as

$$\delta \equiv \frac{y}{y_{1/2}(x)} \tag{2.21}$$

where y is the transverse distance from the wake axis to a specific point in the wake, $y_{1/2}$ is the transverse half-wake width where the velocity deficit is half of the centreline maximum velocity deficit in the wake, ΔU_{max}, and x is the downstream position [9]. Then, the velocity deficit in the wake, ΔU, can be expressed as a function of wake width:

$$\Delta U = f(\delta) \tag{2.22}$$

ΔU can be shown to be independent of downstream position, x, by considering conservation of momentum [25]. Thus, at all downstream distances within the far wake region, the velocity

deficit profile of the wake follows the same distribution and can therefore be defined as self-similar [9]. The velocity deficit, ΔU, in the far wake of a turbine follows a Gaussian curve and can be expressed as follows:

$$\Delta U = \Delta U_{max} \exp\left(\ln(2)\frac{y^2}{y_{1/2}^2}\right) \tag{2.23}$$

The centreline maximum velocity deficit in the far wake of a turbine, ΔU_{max}, decreases proportional to $x^{-2/3}$, whereas the transverse half-wake width, $y_{1/2}$, increases proportional to $x^{1/3}$ [25].

The assumptions of self-similar and axisymmetric distributions of velocity deficit and turbulence intensity in the far wake are not completely valid due to the presence of bounding surfaces and the shear of the ambient flow [21, 23]. Turbine investigations, both numerical and experimental, have shown that the point of maximum velocity deficit is usually located below the turbine axis, i.e., in the half of the wake where a tower is present, and the point of maximum turbulence intensity is located above the turbine axis.

2.3.3 Quantification of turbulence

Two different methods are commonly used to quantify the level of turbulence in the flow during turbine wake investigations. When considering the flow in only one dimension, the parameter turbulence intensity (TI) is used. Turbulence intensity is defined as

$$TI = \frac{u'}{u_{mean}} \tag{2.24}$$

where u' is the standard deviation of the fluid velocity in the average flowing direction and u_{mean} is the magnitude of the average fluid velocity [23].

When considering the flow in three dimensions, turbulence can be quantified by the parameter turbulence kinetic energy (TKE). TKE is measure of the kinetic energy per unit mass from the velocity fluctuations of the three velocity components. The TKE is associated with eddies in turbulent flows. Turbulence kinetic energy is defined as

$$TKE = \frac{1}{2}((u')^2 + (v')^2 + (w')^2) \tag{2.25}$$

where u', v' and w' are the standard deviations of the three velocity components.

In this thesis, the fluid velocities are measured in three directions, as will be explained in chapter 3.1.6. Turbulence is therefore quantified in terms of TKE when studying the wake of the two actuator discs regarded in this thesis, which is further described in chapter 3.3.2.

2.4 Blockage due to confined channel

When considering an isolated single rotor turbine, upstream blockage effects are accounted for by the axial induction factor, *a*, as described in chapter 2.1. However, additional blockage effects can be experienced if a turbine is operating in a confined channel. This is most relevant when considering a turbine in a tidal channel [9]. In a tidal channel, additional constraints can be imposed on the fluid flow by the free water surface, the channel walls and the seabed. Thus, the experiments of this thesis regarding actuator discs in the MarinLab tank, i.e., a confined channel, could be influenced by blockage effects. The blockage effects from a confined channel will be described in this chapter by considering an actuator disc in a confined channel, as shown in figure 6. This figure is an edited version of figure 1, applying the same symbols as explained in chapter 2.1. However, the added symbols will be explained in this chapter.

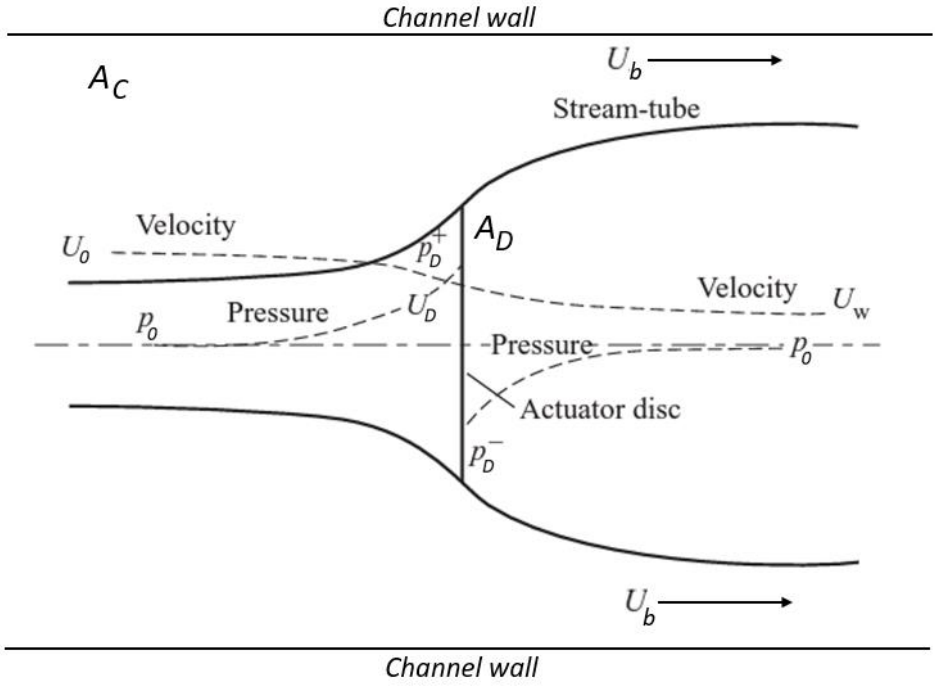

Figure 6: Representation of the effects when fluid passes an actuator disc placed in a confined channel [17].

In figure 6, A_D is the area of the disc (or swept area of a turbine) given by $A_D = \pi R^2$, and A_C is the cross-sectional area of the confined channel. Between the streamtube and the channel walls, there will exist a bypass flow velocity, U_b.

The blockage ratio, B, of an actuator disc in a confined channel is given by

$$B = \frac{A_D}{A_C} \tag{2.26}$$

Blockage causes the flow to divert around the disc, thus increasing the bypass flow velocity, U_b, and reducing the disc velocity, U_D [9]. Consequently, the pressure drop across the disc increases, which implies that both the thrust and power extraction of the disc are increased as well.

Several turbine investigations have demonstrated that the performance of a turbine, i.e., the power and thrust coefficients, is significantly changed when blockage ratios exceed 5-10% [13-15]. Blockage corrections are commonly applied to account for high blockage ratios. Glauert [26] developed the first blockage correction method based on one-dimensional momentum theory for actuator discs. Several models for blockage correction have been developed, e.g., Ewald [27] and Mikkelsen and Sørensen [28]. No blockage corrections are applied to the results of this thesis. However, the effects of blockage are illuminated and discussed.

By re-deriving the one-dimensional momentum theory for a turbine in a confined channel, Garrett and Cummins [29] showed that the maximum power extraction from a turbine occurs when $U_W = \frac{U_0}{3}$, and is given by

$$P_{max} = \frac{16}{27}(1-B)^{-2}\frac{1}{2}\rho A_D U_0^3 \tag{2.27}$$

By comparing the maximum power extraction of a turbine in a confined channel, given by equation (2.27), with the maximum power of an isolated turbine, an additional efficiency term, expressed as $(1-B)^{-2}$, occurs for the turbine influenced by channel boundaries. Accordingly, the Betz limit, as explained in chapter 2.1, can be exceeded due to blockage from a confined channel.

The one-dimensional momentum theory, as presented in chapter 2.1, states that the maximum power extraction from a turbine occurs when a=1/3. Inserting a=1/3 into equation (2.10) yields

$U_W = \frac{U_0}{3}$. Thus, the maximum power extraction from a turbine is found when a=1/3 regardless of whether the turbine is affected by blockage from a confined channel or not.

The thrust coefficient of a turbine is also increased due to the influence of channel boundaries [9]. When a turbine in a confined channel operates with maximum power extraction, i.e., $U_W = \frac{U_0}{3}$, the thrust coefficient is given by

$$C_T = \frac{8}{9}\frac{(1+B)}{(1-B)^2} \tag{2.28}$$

For an isolated turbine operating at maximum power, C_T=8/9, thus the additional thrust term due to the influence of channel boundaries is given by $\frac{(1+B)}{(1-B)^2}$.

In addition, turbine wake expansion is limited by channel boundaries. Studies performed by McTavish et al. [13] and Sarlak et al. [14] demonstrate that increasing blockage ratio causes a narrower turbine wake. In a tidal channel, the wake is constrained vertically by the free water surface which, in particular, is likely to affect the far wake [22]. For model scale experiments in water tanks, it is important to consider the influence of channel boundaries on wake expansion. An experimental study by Stallard et al. [22], investigating the wake of a tidal stream turbine in a shallow turbulent flow, found the expansion rate of the shear layer to be significantly larger in the horizontal plane compared to the vertical plane due to the depth-constraint of the free water surface and the bottom of the tank.

For a tidal turbine, the pressure changes occurring in the region of the turbine causes a drop in the free water surface across the turbine [30]. If the turbine is not at a sufficient depth, the wake may be influenced by the deformation of the water surface or by potential waves formed in the surface due to the turbine's interaction with the water flow. The proximity of a free water surface must also be considered when investigating actuator discs in a water tank. The effects of the water surface can be observed by measuring the vertical velocity component, i.e., velocity in the z-direction, in the wake of a disc. Bjørnsen [31] conducted measurements in the wake of a 0.2 m diameter trapezoidal holed actuator disc with a solidity of 57%, towed with a velocity of 0.5 m/s through the MarinLab tank at HVL, and concluded that placing the disc centre point at a depth of 30 cm was sufficient to minimise the influence of the water surface on the vertical velocity component. For the experiments regarded in this thesis, the centre points of the actuator discs were placed at a depth of 1.0 m. Free water surface effects on the vertical velocity component in the wake are therefore assumed to be insignificant.

2.5 Scaling

If model scale experiments are to represent full scale devices, it is necessary to maintain geometric, kinematic and dynamic similarity between the full scale and model scale devices [9]. Geometric similarity implies that the shape of the full scale and model devices must be identical, i.e., all dimensions must have the same scale ratio [32]. Kinematic similarity is maintained if velocities in the model have the same direction and proportional magnitude to those in the full scale [33]. For dynamic similarity to be achieved, the ratio between different forces in the full scale and model must be equal [32].

The blades of the 0.7 m diameter model turbine to be built at HVL are geometrically scaled from a tidal turbine with a diameter of 21.0 m and a rated speed of 3.0 m/s. In this thesis, two actuator discs with diameters of 0.7 m and 0.2 m are used to represent the full scale device. The subscripts f and m are used to denote the parameters of the full scale and model scale, respectively, in this chapter.

An essential requirement of geometric similarity is maintained by applying a scaling factor, λ, which is given by

$$\lambda = \frac{L_f}{L_m} \tag{2.29}$$

where L_f is the characteristic length of the full-scale (here considered as rotor diameter) and L_m is the characteristic length of the model (here considered as the disc diameter) [32].

Thus, the two actuator discs regarded in this thesis, with diameters of 0.7 m and 0.2 m, are scaled down with factors of 30 and 105, respectively, in regard to the full scale turbine. Despite the two discs having different diameter dimensions, the thickness of both discs is 5 mm, meaning that the disc thickness is not scaled correctly. This could potentially impact the results in terms of comparing the two discs. Investigating turbines by using actuator discs means that geometric similarity is not maintained, as the shape of the turbine and disc are not identical. However, the actuator discs are designed to emulate the velocity distribution behind a three-bladed rotating turbine.

When conducting experiments in a towing tank, it is important to consider gravitational, viscous and inertial forces. Scaling with regard to similarity in Reynolds number is applied when inertial forces and viscous forces are of predominant importance in the flow, which, for instance, is the case for wake development behind a body in a flow [33]. The Reynolds number, Re, is a

dimensionless number describing the ratio of inertial forces to viscous forces in a flowing fluid, and is given by

$$Re = \frac{\rho UL}{\mu} = \frac{UL}{\nu} \tag{2.30}$$

where ρ is the density of the flowing fluid, U is the flowing velocity of the fluid, L is a characteristic length (here considered as the rotor/disc diameter), μ is the dynamic viscosity of the fluid and ν is the kinematic viscosity [34].

Therefore, scaling through similarity in Reynolds number ensures that viscous forces are scaled correctly [32]. Reynolds scaling implies the following relation:

$$Re_m = \frac{U_m L_m}{\nu_m} \equiv Re_f = \frac{U_f L_f}{\nu_f} \tag{2.31}$$

The fluid velocity required in model scale experiments for similarity in Reynolds numbers to be maintained can be found by rearranging equation (2.31):

$$U_m = \frac{Re_f \nu_m}{L_m} \tag{2.32}$$

In table 1, the kinematic viscosities of the full scale fluid, i.e., salt water, and the model scale fluid, i.e., fresh water, are based on a fluid temperature of 16°C. Applying equation (2.32) for the 0.7 m and 0.2 m diameter actuator discs, yields towing velocities of 86.1 m/s and 301.4 m/s, respectively, for Reynolds similarity to be achieved. The MarinLab towing tank at HVL can be operated with a maximum towing velocity of 5.0 m/s. Therefore, these towing velocities are not achievable for the experiments of this thesis.

Hydrodynamic forces are usually scaled through similarity in Froude number when gravitational forces are important in the flow, which is the case whenever a free water surface is present [33]. The Froude number, Fr, is a dimensionless number which describes the square root of the ratio of inertial forces to gravitational forces in a flowing fluid, and is given by

$$Fr = \frac{U}{\sqrt{gL}} \tag{2.33}$$

where U is the flowing velocity of the fluid, g is the acceleration of gravity and L is a characteristic length (here considered as the rotor/disc diameter) [32].

Froude scaling ensures that gravitational forces are correctly scaled by maintaining similarity in Froude numbers between the full scale device and the model scale device, which yields:

$$Fr_m = \frac{U_m}{\sqrt{gL_m}} \equiv Fr_f = \frac{U_f}{\sqrt{gL_f}} \tag{2.34}$$

In equation (2.34) it is assumed that the acceleration of gravity, g, is identical in the full scale and model scale. Rearranging equation (2.34) yields the required fluid velocity in model scale experiments for similarity in Froude numbers to be maintained:

$$U_m = Fr_f\sqrt{gL_m} \tag{2.35}$$

Applying equation (2.35) for the 0.7 m and 0.2 m diameter actuator discs, yields towing velocities of 0.55 m/s and 0.29 m/s, respectively, for Froude similarity to be achieved. These towing velocities can be achieved in the MarinLab towing tank. However, for the wake investigations of the actuator discs regarded in this thesis, the towing velocity was limited to 0.4 m/s, as will be explained in chapter 3.1.7. This towing velocity was applied for both discs during wake measurements, meaning that Froude similarity was not fully achieved. For the axial force measurements, however, towing velocities ranged from 0.1 m/s to 0.6 m/s for both discs. The Reynolds number and Froude number of the full scale and model scale during wake investigations are presented in table 1.

Table 1: Reynolds number and Froude number of the full scale and model scale during wake investigations.

	d **[m]**	***U*** **[m/s]**	***ν*** **[m²/s]**	**Re**	**Fr**
Full scale	21.0	3.0	$1.159 \cdot 10^{-6}$	$5.436 \cdot 10^{7}$	0.209
Model scale 1	0.7	0.4	$1.109 \cdot 10^{-6}$	$2.525 \cdot 10^{5}$	0.153
Model scale 2	0.2	0.4	$1.109 \cdot 10^{-6}$	$7.214 \cdot 10^{4}$	0.286

Maintaining dynamic similarity between the full scale and model scale is impossible, as this requires both Reynolds similarity and Froude similarity to be achieved simultaneously [33]. As shown in table 1, there is a mismatch between the full scale device and two model scale devices both in terms of Reynolds number and Froude number. Therefore, there are some characteristics of the full scale device that will not be fully represented by the models.

The Reynolds number of the full scale device is significantly higher than the model scale. A general assumption is that representative turbulence and wake mixing will occur during wake

experiments, where turbulence affects the wake recovery, provided that the flow is within the turbulent regime [9]. It has been shown through several experimental studies and numerical simulations that the performance, i.e., the power and thrust coefficients, of a geometrically scaled turbine is unrepresentative of the full scale device, owing to the significantly lower Reynold number of the model turbine [35-38].

There is also a mismatch between the Reynolds numbers of the two actuator discs, which potentially could influence the results when comparing these discs. The Reynolds numbers of the 0.7 m and 0.2 m diameter discs are $2.525 \cdot 10^5$ and $7.214 \cdot 10^4$, respectively. An experimental study by Chamorra et al. [39] investigates the Reynolds dependency of the velocity deficit and turbulence intensity in the wake of a model-scale wind turbine in a wind tunnel with Reynolds numbers ranging from $1.66 \cdot 10^4$ to $1.73 \cdot 10^5$. The results from Chamorra et al. show that the velocity deficit is independent of Reynolds number when $Re \geq 4.8 \cdot 10^4$. Turbulence intensity was shown to be independent of Reynolds number when $Re \geq 4.8 \cdot 10^4$ from four to twelve rotor diameters downstream. In the near wake, however, Reynolds independence for turbulence intensity started at $Re \geq 9.3 \cdot 10^4$. Experiments were not performed with Reynolds numbers between $4.8 \cdot 10^4$ and $9.3 \cdot 10^4$, thus it is not possible to exactly determine when Reynolds independence is achieved in terms of turbulence intensity.

As previously stated, for the wake investigations on the 0.2 m diameter actuator disc regarded in this thesis, the Reynolds number is $7.214 \cdot 10^4$. As such, there is a slight possibility that Reynolds independence is not fully achieved for the wake flow of this disc. However, based on the results of Chamorra et al. [39], the mismatch between the Reynolds numbers of the two actuator discs of this thesis is expected to have insignificant impact when comparing the wake flows of these discs.

The scaling laws described in this chapter can also be applied for scaling against full scale wind turbines or if experiments are to be performed in a wind tunnel.

3 Methodology

In this chapter, the MarinLab towing tank and the experimental setups for the two actuator discs are described. Furthermore, the measurement campaign and data processing for the axial, transverse and vertical velocity profile measurements and the axial force measurements are presented. The working principles of measurement equipment are explained, and uncertainties associated with the experiments are discussed.

3.1 Experimental method

3.1.1 MarinLab towing tank

All the experiments of this thesis were performed in the MarinLab towing tank at HVL [40]. This tank is shown in figure 7. The tank is 50 m long, with a width of 3.0 m and a depth of 2.2 m. It is filled with fresh water with a temperature of approximately 16°C.

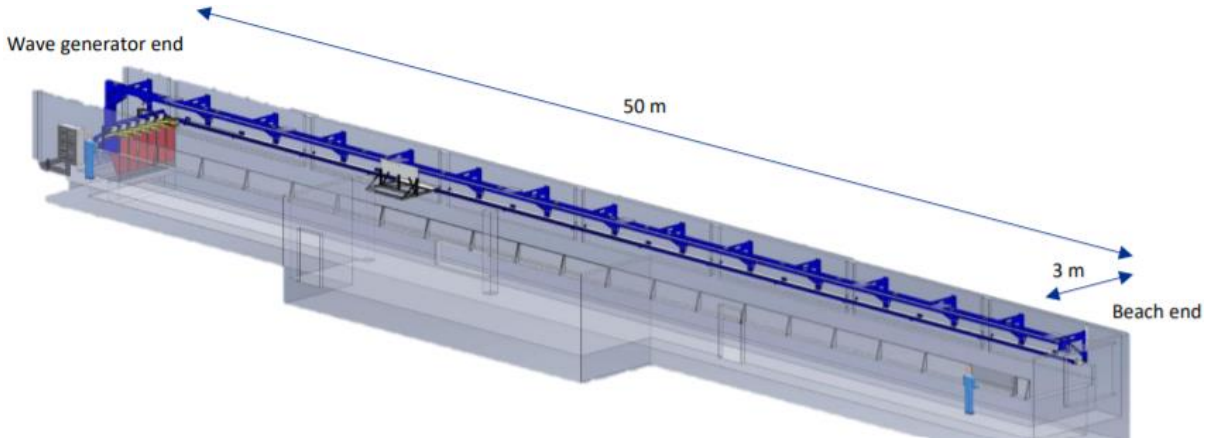

Figure 7: The MarinLab towing tank at HVL [40].

The tank is equipped with two carriages, a wave generator and a wave breaker, i.e., a beach. The carriages are wire operated with a maximum towing velocity of 5.0 m/s. The water in the tank is stationary. Therefore, the two carriages are used to move the discs and associated measurement equipment through the water at the desired velocity. If sufficient time is allowed to pass between towing runs, no turbulence will be present in the water. See [40] for additional information on the MarinLab towing tank.

No waves were applied for the experiments of this thesis. The wave generator was only used for particle mixing prior to the experiments involving wake velocity measurements with the acoustic Doppler velocimeter (ADV). This will be further explained in chapter 3.4.

3.1.2 Porous actuator discs

Two trapezoidal holed porous actuator discs with diameters of 0.7 m and 0.2 m were used for the experiments of this thesis. Both discs are made of aluminium and have a thickness of 5 mm. The two discs are identical in terms of solidity and geometry, both having a solidity of 57% and a geometry as illustrated in figure 8. The holes in the discs are arranged non-uniformly, with a greater solidity near the centre, corresponding to a turbine rotor. This design was made to emulate the velocity distribution behind a three-bladed rotating turbine.

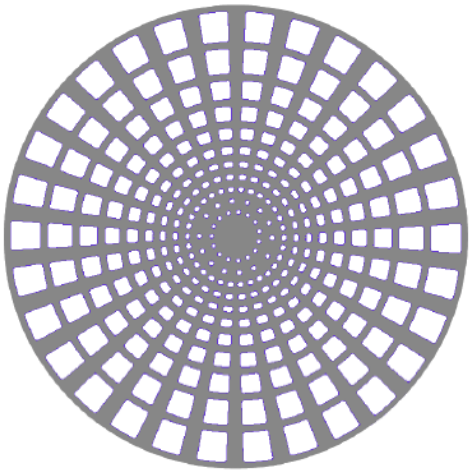

Figure 8: CAD drawing of the porous actuator discs used in this thesis.

For the remainder of this thesis, the 0.7 m diameter disc and the 0.2 m diameter disc will be referred to as AD70 (actuator disc, 70 cm diameter) and AD20 (actuator disc, 20 cm diameter), respectively.

The blockage ratios of both actuator discs were calculated using the blockage ratio expression, see equation (2.26). The blockage ratio of the AD70 and AD20 was found to be 5.8% and 0.5%, respectively.

3.1.3 Experimental setup

The longitudinal, transverse and vertical axes are in this thesis denoted as x, y and z, respectively. Actuator disc diameters are denoted as D. In figure 9, a sketch of the experimental setup for the AD70 in the MarinLab towing tank is shown to provide an overview of this setup. In the following paragraphs, the experimental setup for the AD70 and the AD20 are explained.

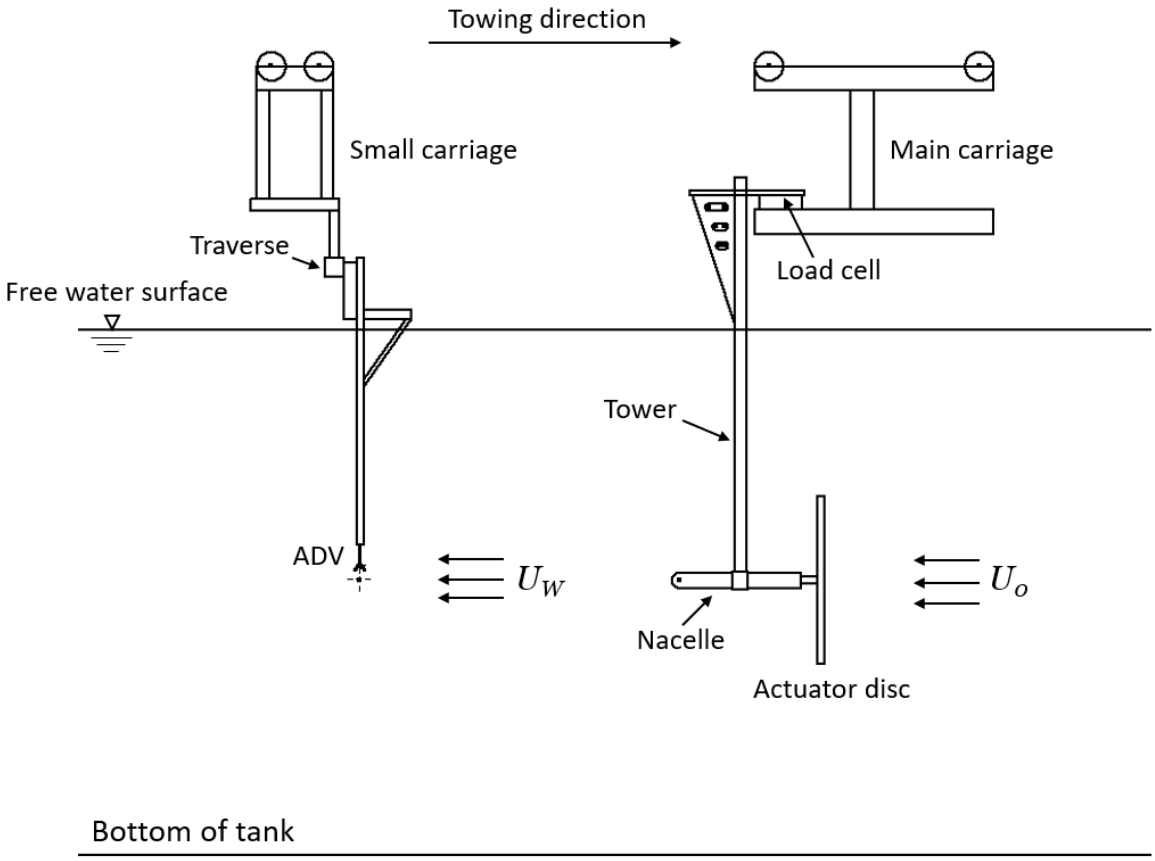

Figure 9: Sketch of the experimental setup for the AD70 in the MarinLab towing tank.

The AD70 is mounted on the nacelle and is attached to the main carriage through a tower, with a diameter of 50 mm (0.071D), and its supporting structure. The length of the nacelle is 525 mm (0.75D), which is relatively larger compared to that of a full scale device. As such, nacelle effects might be more pronounced for the experiments on the AD70 compared to a full scale turbine. A more detailed view of the nacelle is shown in figure 10.

The disc is mounted with both a yaw angle and a tilt angle of 0°, i.e., the axis of the disc is parallel to the towing direction. Axial forces exerted on the disc and tower whilst dragged through the water are measured by a strain gauge load cell mounted on the main carriage. This load cell has a capacity of 100 N. In chapter 3.1.4, the working principle of load cells will be explained.

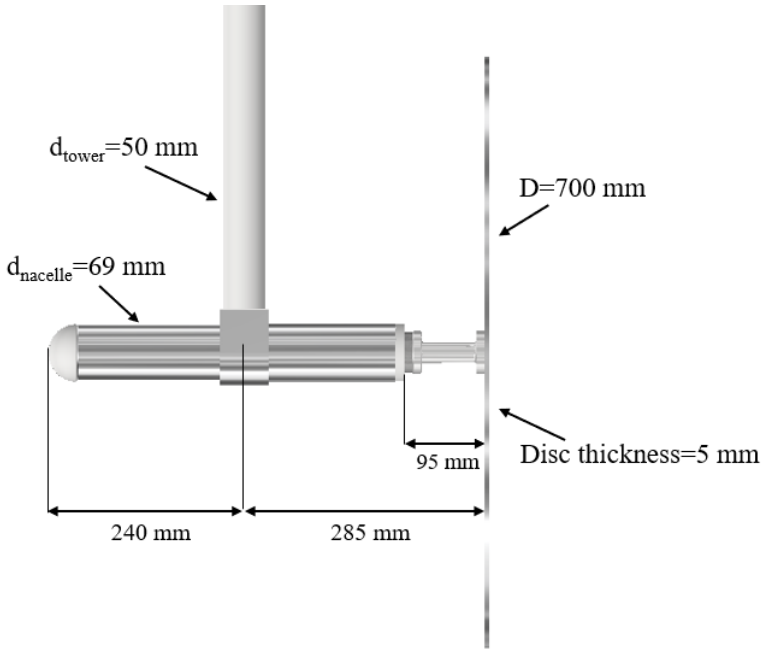

Figure 10: Nacelle of the AD70 rig modelled in Autodesk Inventor Professional 2022.

An acoustic Doppler velocimeter (ADV) of the type Vectrino+, delivered by Nortek, is utilised for velocity measurements downstream of the actuator disc. The working principle of this instrument will be elaborated in chapter 3.1.6.

The transverse position of the ADV can be adjusted by an automated electric motorised traverse, which is mounted on the small carriage, for the measuring of transverse velocity profiles. The traverse can change the position of the ADV by a controlled stepper motor with millimetre precision over the traverse length of 1980 mm. A virtual instrument (VI) in LabVIEW is used to operate the traverse. In order to ensure that the positioning of the ADV is correct, a calibration procedure for the traverse is implemented in the LabVIEW VI. This calibration is done prior to each velocity profile.

For the measuring of vertical velocity profiles, however, the vertical position of the ADV must be adjusted manually. The traverse in the MarinLab is not designed for vertical movement, as there is no brake on the traverse to withstand the weight from the ADV rig mounted on the traverse.

Ideally, the centre point of the actuator discs would be placed in the middle of the tank, both in terms of tank width and depth. This would reduce the possibility of blockage, side walls and free water surface from affecting the measurements. With a tank width of 3.0 m and a depth of 2.2 m, this means that the disc centre point should be located 1.5 m from the tank side walls at a depth of 1.1 m. The cable length of the Vectrino+ was, however, a few centimetres too short

to enable measurements at this depth. During both axial and transverse velocity profile measurements on the actuator discs, as well as the axial force measurements, the disc centre points were therefore positioned at a depth of 1.0 m.

Accordingly, the distance from the AD20 centre point to the tank walls, free surface and tank bottom is 7.50D, 5.00D and 6.00D, respectively. As such, the wake expansion of the AD20 will not be significantly constrained in any direction due to proximity of bounding surfaces. For the AD70, however, the wake will be constrained by bounding surfaces in the vertical direction, and possibly in the transverse direction as well. The distance from the AD70 centre point to the tank walls, free surface and tank bottom is 2.14D, 1.43D and 1.71D, respectively.

The experimental setup for the AD20 is similar to the AD70 setup sketched in figure 9, with a few exceptions. Firstly, the AD20 is mounted directly on the tower, i.e., there is no nacelle. Furthermore, the tower has a diameter of 16 mm (0.080D). I addition, a different strain gauge load cell with a capacity of 10 N is utilised for the AD20 rig. This load cell is mounted directly behind the actuator disc, as opposed to the setup for the AD70, where the load cell is mounted on the carriage. The experimental setups for the AD70 and AD20 are shown in figures 11 and 12, respectively.

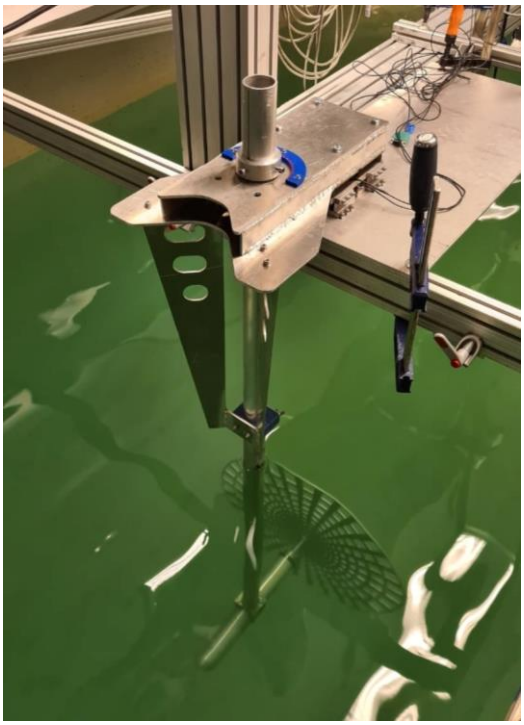

Figure 11: Photograph of the experimental setup for the AD70 in the MarinLab towing tank.

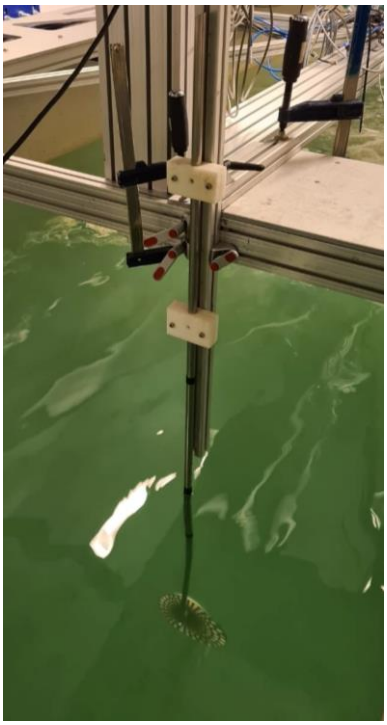

Figure 12: Photograph of the experimental setup for the AD20 in the MarinLab towing tank.

3.1.4 Load cells

Two strain gauge load cells are utilised for the axial force measurements regarded in this thesis. In the following paragraphs, the working principle of this type of load cell is explained.

A strain gauge load cell is a transducer, as it converts mechanical loads into electrical signals which can be measured [41]. For the load cell applications regarded in this thesis, mechanical loads are in the shape of drag forces from the discs.

Strain gauge load cells consist of a load column to which one or more strain gauges are attached [41]. Therefore, when forces are exerted on the load column, both the column and the strain gauges are deformed. The deformation causes a change in the resistance of the strain gauges. By applying a Wheatstone bridge configuration, as shown in figure 13, this change in resistance is returned as an output voltage, V_{out}, which is proportional to the exerted force on the load cell. Accordingly, the output voltage from the Wheatstone bridge can be used as a measure of the force exerted on the load cell.

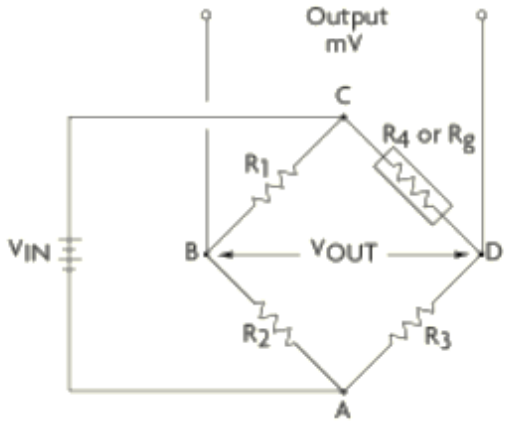

Figure 13: Wheatstone bridge with one strain gauge. The strain gauge is illustrated as R_4 or R_g [42].

Figure 13 shows a Wheatstone bridge with one strain gauge [42]. The strain gauge is illustrated as R_4 or R_g, and will be referred to at R_g in futher explanations and equations. There will be no potential difference between points B and D in the Wheatstone bridge if resistances R_1, R_2, R_3 and R_g are equal. Thus, the output voltage, V_{out}, will be zero. A change in R_g, due to forces being exerted on the load cell, causes the bridge to be unbalanced, and a potential difference will exist between points B and D. V_{out} is therefore equivalent to the voltage drop across R_1 and R_g, which yields:

$$V_{out} = V_{CD} - V_{CB} = V_{in}\left(\frac{R_3}{R_3 + R_g} - \frac{R_2}{R_1 + R_2}\right) \tag{3.1}$$

A load cell with a capacity of 100 N is utilised for the axial force measurements on the AD70. During the axial force measurements, the 100 N load cell is mounted within a construction made by the lab engineers at HVL, as shown in figure 14. Therefore, when conducting calibrations of this load cell, as will be described in chapter 3.1.5, the load cell is also mounted within this construction.

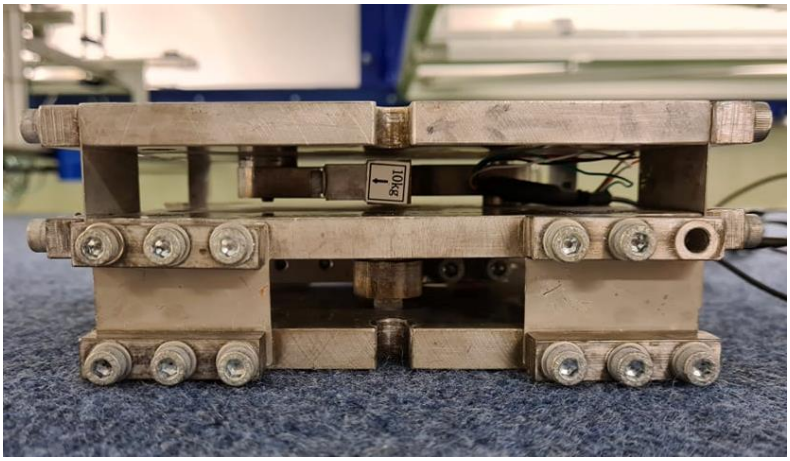

Figure 14: 100 N load cell within its construction.

For the axial force measurements on the AD20, a load cell with a capacity of 10 N was utilised. This load cell was mounted directly behind the actuator disc. Therefore, mounting the load cell within a construction, as shown in figure 14, was not required for these measurements.

3.1.5 Load cell calibrations

Three different calibrations were conducted through this thesis. Both the 100 N load cell for the AD70 rig and the 10 N load cell for the AD20 rig had to be calibrated prior to the axial force measurements. The 100 N load cell was calibrated against a 200 N HBM load cell. Therefore, the 200 N load cell had to be calibrated separately in advance.

All three load cells are designed to be linear, i.e., the force is given by a linear function, y, expressed as

$$y = ax + b \tag{3.2}$$

where a is the gain, x is the voltage readings from the strain gauges and b is the offset. The aim of the calibrations is to find the gain and offset of the different load cells. During axial force measurements, the gain and offset from the load cell calibrations are added to the LabVIEW program which is used to record the data.

The calibration of the 200 N HBM load cell was conducted by adding five known loads, one by one, before removing them in the same manner. The output from the load cell, displayed as mV/V in the LabVIEW program used for the calibration, was noted for each load case, before a new load was added or removed. Then, a linear best fit line, as expressed in equation (3.2) was calculated for the data, providing both the gain and offset of the load cell.

For the calibration of the 100 N load cell, the applied loads were read accurately by the already calibrated 200 N HBM load cell. The results from the 100 N load cell calibration are presented in table 2.

There was uncertainty as to whether the axial force measurements from the 100 N load cell would be affected by vertical loads on the load cell. In the AD70 rig, the load cell is subjected to a vertical load from the weight of the tower, the nacelle, the actuator disc and associated support structures. This weight is approximately 10 kg. Therefore, during the calibration of the 100 N load cell, a weight of 10 kg was placed on top of the load cell.

Table 2: Calibration sheet from 100 N load cell calibration. The accuracy of the measurements is not reflected by the number of digits.

	HBM calculated load (applied load) [N]	**100 N load cell output [mV/V]**	**100 N load cell calculated load [N]**	**Difference between applied and calculated load [N]**
Increasing	-0.49	-0.140	-0.83	0.338
	20.26	0.025	19.66	0.608
	40.11	0.185	39.51	0.600
	60.18	0.345	59.40	0.772
	80.05	0.507	79.58	0.469
Max load	100.05	0.667	99.37	0.682
Decreasing	80.08	0.520	81.18	-1.102
	60.23	0.360	61.24	-1.017
	40.18	0.195	40.76	-0.588
	20.22	0.034	20.73	-0.510
	-0.51	-0.135	-0.26	-0.251

As a quality control, the non-linearity and hysteresis of a load cell can be investigated. Non-linearity can be defined as the difference between the actual and ideal straight-line

behaviour [43]. Considering the load cell calibrations of this thesis, the non-linearity is the difference between the applied load and the load calculated from the linear best fit line of the load cell which is being calibrated.

Non-linearity can also be expressed as the maximum non-linearity, $\widehat{N}$, as a percentage of span, given by

$$\frac{\widehat{N}}{O_{max} - O_{min}} \times 100\% \tag{3.3}$$

where O_{max} and O_{min} are the maximum and minimum output of the load cell, respectively.

The 100 N load cell calibration showed a maximum non-linearity as a percentage of span of 1.102%. This maximum non-linearity was significantly higher than for the 200 N and 10 N load cells, i.e., 0.052% and 0.059%, respectively. It is likely that the relatively high non-linearity of the 100 N load cell is caused by the construction in which it is mounted, see figure 14.

The load cell calibrations showed that for a given applied load, the measured force from the load cells were different depending on whether the load was increasing or decreasing. This phenomenon is called hysteresis. Hysteresis can be defined as the difference between the measured force for a given applied load during increasing and decreasing of the load [43].

The hysteresis from the 100 N load cell calibration was considerably larger compared to the other load cells. Figure 15, which represents the data presented in table 2, shows the hysteresis from the 100 N load cell calibration.

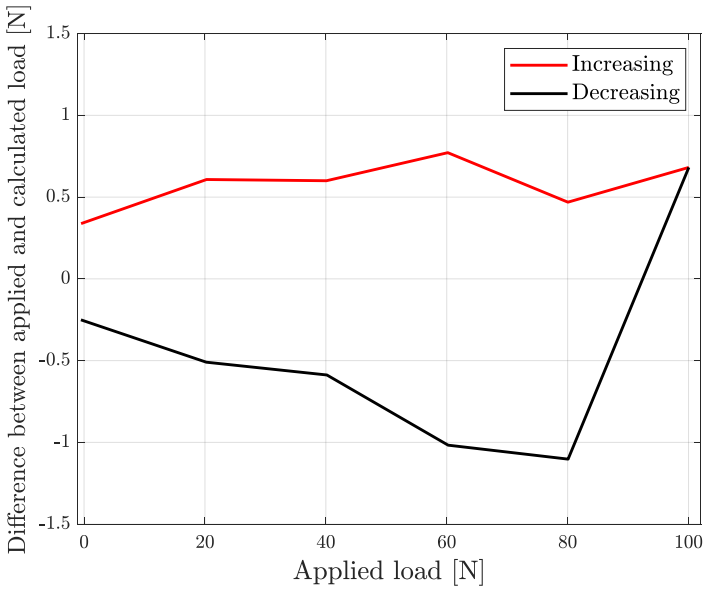

Figure 15: Hysteresis curve for calibration of 100 N load cell.

For the calibration of the 10 N load cell, the load cell was mounted between the AD20 and the tower, i.e., similar to how it would be mounted during axial force measurements. The load cell was calibrated by applying five known loads, one by one, to the centre of the disc, before removing them in the same manner.

3.1.6 Acoustic Doppler velocimeter (ADV)

An acoustic Doppler velocimeter (ADV) measures water velocities based on a physical phenomenon called the Doppler effect or the Doppler shift [44]. The Doppler shift is the change in frequency of a sound wave when an observer moves with respect to a wave source, or vice versa.

This type of velocimeters measures velocity by transmitting a pair of short sound pulses of a fixed frequency into the water. Some of the sound waves are reflected off suspended particles in the water and return to the ADV receiver arms with a relative change in frequency due to the Doppler shift. The frequency of the reflected signal will be shifted in accordance with the water velocity. Thus, the frequency shift can be utilised to find the water velocity, *V*, by using the following equation:

$$V = \frac{c f_{Doppler}}{2 f_{transmitted}} \tag{3.4}$$

where c is the speed of sound in water, $f_{Doppler}$ is the change in the received frequency (the Doppler shift), $f_{transmitted}$ is the frequency of the transmitted sound.

A Vectrino+ with a downward looking probe was used for velocity measurements downstream of the actuator discs to quantify the wake. This instrument is shown in figure 16. The Vectrino+ is a high-resolution ADV delivered by Nortek. For the experiments regarded in this thesis, the instrument was set to its maximum sampling frequency of 200 Hz. See [44] for the comprehensive manual of the Vectrino+.

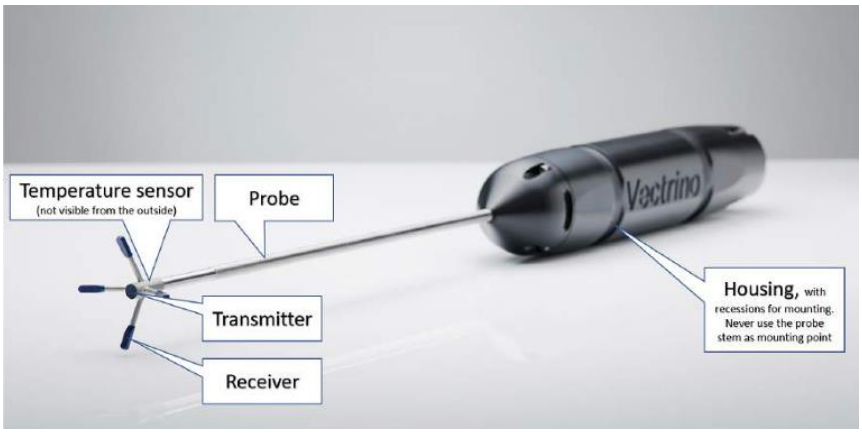

Figure 16: Vectrino+ ADV with downward looking probe from Nortek [44].

As shown in figure 16, the Vectrino+ has four receiver arms. These receiver arms are arranged as illustrated in figure 17.

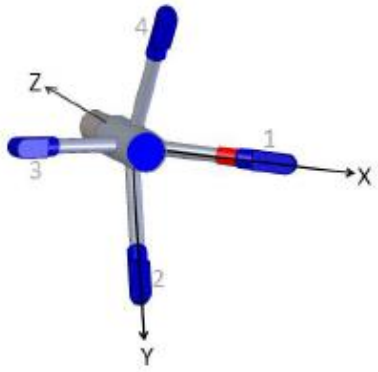

Figure 17: Vectrino+ coordinate system (XYZ) and numbering of receiver arms for downward looking probe [44].

The arrangement of the receiver arms, as shown in figure 17, enables the Vectrino+ to measure all three components of the velocity vector. Receiver arms 1 and 3 measure the X-velocity, whereas receiver arms 2 and 4 measure the Y-velocity. The Z-velocity, however, is measured twice: once from receiver arms 1 and 3 and once from 2 and 4. Thus, there are four signal outputs from the ADV: X, Y, Z_1 and Z_2.

Neutrally buoyant particles, i.e., particles with the same buoyancy as water, were suspended in the MarinLab tank to ensure that the acoustic signals from the ADV transmitter were reflected. The quality of the data from the ADV is dependent on the seeding in the MarinLab tank, i.e., the amount and degree of mixing of suspended particles in the water. Data quality can be assessed in terms of the signal strength and correlation. These two parameters are outputted by the instrument continuously during data collection.

Signal strength can be quantified as signal-to-noise ratio (SNR) in dB. SNR is a measure of the magnitude of the signal reflected from the suspended particles (received echo), A_{signal}, relative to the background noise level, A_{noise}. The SNR of the Vectrino+ is given by the following equation:

$$SNR = 20\log_{10}\left(\frac{A_{signal}}{A_{noise}}\right) \tag{3.5}$$

Nortek [44] recommends an SNR above 15 dB when collecting raw data, whereas mean data should be collected with a minimum SNR of 5 dB.

Correlation is a measure of the agreement between the two pulse echoes that are being measured. A correlation of 0 means that there is no similarity between the two echoes, whereas 100% correlation indicates exact agreement. The correlation is aimed to be high, as is gives confidence that the two measured pulses are the same pulses that were originally sent out by the instrument. Thus, the instrument is determining a valid phase shift.

Nortek [44] reports that users in the early days of the acoustic Doppler velocimeter considered the instrument to be generating good quality data if correlations were above 70%. Although this threshold is still applied by many users, Nortek will not warrant a generalisation so some universal value. The best way to determine a correlation threshold is by closely examining the data set.

3.1.7 Towing velocities

The towing velocities for the experiments conducted in this thesis were limited by two factors which will be described below.

The first limiting factor was the capacity of the load cell for the AD20, i.e., 10 N. When exerting forces on the load cell, a safety factor (SF) should be included as a precaution. For the experiments of this thesis, applying SF=2-2.5 is reasonable, considering that loading and environmental conditions are not severe, and ordinary materials are used [45].

Before any axial force measurements were conducted on the AD20, calculations were made on the expected force exerted on the load cell at different towing velocities, i.e., the drag force from the disc as it is towed through fresh water. Previous experiments conducted in the MarinLab tank by Hansen et al. [18] investigated the thrust coefficient of an identical disc to the AD20, resulting in C_T=0.88. This thrust coefficient was applied for the theoretical

estimations of disc thrust force on the AD20 and the AD70 when determining appropriate towing velocities. Thrust force calculations on the AD20 were made based on equation (2.14), using the following parameter values: $C_{T,disc}$=0.88, $\rho_{freshwater}$=998.95 kg/m^3 (freshwater density at 16°C) and d_{disc}=0.2 m. The results from these calculations are presented in table 3.

Table 3: Theoretically estimated thrust forces on the AD20 using C_T=0.88.

Tow velocity, *U* [m/s]	**Re**	**Disc thrust force [N]**
0.4	$7.214 \cdot 10^4$	2.21
0.5	$9.017 \cdot 10^4$	3.45
0.6	$1.082 \cdot 10^5$	4.97
0.7	$1.262 \cdot 10^5$	6.77
0.8	$1.443 \cdot 10^5$	8.84

The theoretically estimated disc thrust force at 0.6 m/s, i.e., 4.97 N, yields the following safety factor, *SF*:

$$SF = \frac{10\ \text{N}}{4.97\ \text{N}} = 2.01 \tag{3.6}$$

Consequently, towing velocities should be limited to 0.6 m/s for the axial force measurements on the AD20.

For the axial force measurements on the AD70, the load cell capacity is 100 N. This load cell has an integrated safety factor of 2.0, meaning that it breaks at 200 N. Therefore, the load cell can safely be loaded to 100 N, without any risk of damaging it.

Thrust force calculations on the AD70 were made based on equation (2.14), using the following parameter values: $C_{T,disc}$=0.88, $\rho_{freshwater}$=998.95 kg/m^3 and d_{disc}=0.7 m. However, this calculation only yields the thrust force on the disc. As previously explained, the load cell of the AD70 is also exerted to drag forces from the tower. The tower drag must therefore be added to the disc thrust to find the total axial forces exerted on the load cell.

No waves are applied for the experiments of this thesis, hence the drag force on the tower can be found from the drag term in Morison's equation:

$$F_{D,tower} = \frac{1}{2}\rho_{freshwater} A_{tower} u^2 C_{D,tower} \tag{3.7}$$

where $\rho_{freshwater}$ is the freshwater density, A_{tower} is the projected area of the tower immersed in water, u is the inflowing water velocity and $C_{D,tower}$ is the drag coefficient of the tower. The tower is a cylinder-shaped object with a vertical axis normal to the incoming flow. Thus, the projected area, A_{tower}, is given by $A_{tower}=L_{tower}d_{tower}$, where L_{tower} is the length of the tower which is immersed in water and d_{tower} is the diameter of the tower.

Applying equation (3.7), the tower drag of the AD70 rig was calculated using the following parameter values: $C_{D,tower}$ = 0.90 (see [46]), $\rho_{freshwater}$ = 998.95 kg/m^3, L_{tower} = 1.0 and d_{tower} = 0.05 m. The results from the force calculations on the AD70 rig are presented in table 4.

Table 4: Theoretically estimated drag forces on the AD70 rig using C_T=0.88.

Tow velocity, *U* [m/s]	**Re**	**Disc thrust force [N]**	**Tower drag [N]**	**Disc & tower drag [N]**
0.4	$2.525 \cdot 10^5$	27.06	3.60	30.66
0.5	$3.156 \cdot 10^5$	42.29	5.62	47.91
0.6	$3.787 \cdot 10^5$	60.90	8.09	68.99
0.7	$4.418 \cdot 10^5$	82.89	11.01	93.90
0.8	$5.050 \cdot 10^5$	108.26	14.38	122.64

As shown in table 4, the forces exerted on the load cell at towing velocities of 0.6 m/s and 0.7 m/s, with the actuator disc mounted on the rig, are approximately 69 N and 94 N, respectively. Thus, the load cell capacity would allow measurements up to 0.7 m/s. However, measurements on the AD70 were not taken at towing velocities above 0.6 m/s, as this was the maximum velocity for the AD20 measurements and would provide sufficient data for comparison of the two discs.

The other limiting factor on towing velocity was vibrations on the ADV probe due to hydrodynamic forces on the ADV rig. A new rig for the ADV had to be made to measure velocities at a depth of 1.0 m. In previous student projects and experiments using the ADV in

the MarinLab, measurements have been taken closer to the surface. Mounting the ADV probe so that it measures at a depth of 1.0 m means that the construction to which the probe is attached extends approximately one meter into the water and will therefore be exposed to hydrodynamic forces when it is dragged through the water.

When using the maximum towing velocity with respect to the load cell capacity, i.e., 0.6 m/s, vibrations on the ADV probe were observed. By reducing the towing velocity to 0.5 m/s, the vibrations became smaller, but they were still detectable. Therefore, the towing velocity was reduced to 0.4 m/s. At this velocity, no vibrations were observed and the ADV measurements were deemed acceptable.

Consequently, 0.4 m/s was set as the towing velocity for all the wake measurements regarded in this thesis. For the axial force measurements, however, towing velocities up to 0.6 m/s could be applied, as these tests were not dependent on ADV measurements. In other words, the axial force measurements were only limited by the capacity of the load cell for the AD20.

3.2 Measurement campaign

The measurements conducted through this project are summarised in table 5. This table provides short descriptions of the different types of measurements that were conducted, as well as stating the resultant parameters from the experiments and which instruments were used during these experiments.

Table 5: Measurement campaign.

Measurement description	**Resultant parameters**	**Method/ instruments**
Measurement (A) - Axial force measurements		
A-1: AD70 Thrust curves at velocities: 0.1 m/s - 0.6 m/s	$F_{T\,mean}$ C_T	Load cell (100 N)
A-2: AD20 Thrust curves at velocities: 0.1 m/s - 0.6 m/s	$F_{T\,mean}$ C_T	Load cell (10 N)
Measurement (B) - Axial velocity profiles		
B-1: AD70 Profiles of velocity deficit and TKE at x/D=1-10 (increments of 0.5).	U_{mean} TKE	ADV Traverse
B-2: AD20 Profiles of velocity deficit and TKE at x/D=1-10 (increments of 0.5).	U_{mean} TKE	ADV Traverse
Measurement (C) - Transverse velocity profiles		
C-1: AD70 Profiles of velocity deficit and TKE at x/D=1, 2, 4, 6, 7 and 10.	U_{mean} TKE	ADV Traverse
C-2: AD20 Profiles of velocity deficit and TKE at x/D=2, 4, 7 and 10.	U_{mean} TKE	ADV Traverse
Measurement (D) - Vertical velocity profiles		
D-1: AD70 Profiles of velocity deficit and TKE at x/D=2 and 7.	U_{mean} TKE	ADV Traverse
D-2: AD20 Profiles of velocity deficit and TKE at x/D=2 and 7.	U_{mean} TKE	ADV Traverse

As shown in table 5, there are four main types of measurements conducted through this thesis: (A) - axial force measurements, (B) - axial velocity profiles, (C) - transverse velocity profiles and (D) - vertical velocity profiles. The procedures for these measurements are elaborated in the following subchapters.

A decay test of turbulence was performed by Aasnæs [47] in 2021 to investigate how much time that was needed between each run in the MarinLab towing tank to ensure that there was no residual flow or turbulence in the tank that could considerably impact the results of the next towing run. The test was performed by collecting velocity data from the ADV as the carriage was moving back to its starting position and the following five minutes when the carriage was standing still. The rewind speed of the carriage was set to 0.5 m/s, similar to the rewind speed for the experiments regarded in this thesis. TKE was plotted as a function of time. Three minutes after the carriage reached its starting position, the TKE was considered to be insignificantly small. Therefore, Aasnæs recommended a minimum wait of three minutes between each run. A similar minimum wait was set between each run in the towing tank for the velocity measurements regarded in this thesis. However, as a precaution, the signal from the ADV was checked prior to each run to confirm that the signal was unaffected by residual flow or turbulence from the previous run.

3.2.1 Measurement (A) - Axial force measurements

Axial forces on the AD70 were measured using a load cell with a capacity of 100 N. Measurements were taken at different towing velocities, ranging from 0.1 to 0.6 m/s, both with and without the actuator disc mounted on the rig. Accordingly, the drag force on the tower (tare load) could be subtracted from the total drag force on the disc and tower, yielding the drag force on the disc, referred to as thrust force in this thesis. Furthermore, the thrust force can be used for calculation of the thrust coefficient of the disc.

A 10 N load cell was used for axial force measurements on the AD20, with towing velocities ranging from 0.1 to 0.6 m/s. As the load cell was mounted behind the disc, the disc thrust force could be measured directly, without considering tower drag.

Every towing test measuring axial force at velocities from 0.1 m/s to 0.3 m/s were conducted three times. The measurements at velocities from 0.4 m/s to 0.6 m/s were, however, conducted five times. The mean value of these measurement series was used to calculate the thrust coefficients of the discs at the associated towing velocity.

3.2.2 Measurement (B) - Axial velocity profiles

Axial velocity measurements, using the ADV, were taken at different distances downstream of the actuator discs at the disc centreline, i.e., y/D=0. Measurements were taken at downstream distances from 1D to 10D, with increments of 0.5D, giving a thorough representation of the velocity deficit and turbulence development downstream of the disc at the centreline. The towing tests for the axial velocity profiles were conducted twice for every downstream distance. The mean value of these two measurement series was used in the analysis of both axial velocity deficit and TKE profiles. In figure 18, the measurement procedure for the axial velocity profiles is illustrated.

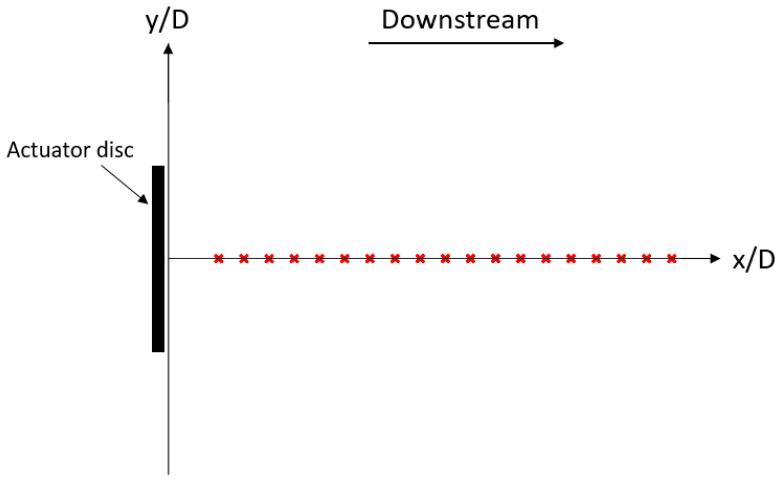

Figure 18: Illustration of measurement procedure for axial velocity profiles (seen from above). The red crosses in the figure illustrate where measurements were conducted.

3.2.3 Measurement (C) - Transverse velocity profiles

Transverse velocity profiles were measured at several distances downstream of the actuator discs using the ADV. For the AD70, transverse velocity profiles were measured at 1D, 2D, 4D, 6D, 7D and 10D downstream of the disc, whereas the AD20 was only measured at downstream distances of 2D, 4D, 7D and 10D. Thus, the velocity deficit and turbulence development downstream of the discs can be compared at four different downstream distances, i.e., at 2D, 4D, 7D and 10D.

Transverse velocity profiles were also measured for the rig of the AD70 without the actuator disc mounted on the nacelle to get an impression of the impact from the nacelle and tower on the wake of the disc. These measurements were only carried out at downstream distances of 1D, 2D and 4D, as the wake was observed to be almost fully recovered at 4D. This is apparent

from the transverse velocity deficit and TKE profiles of the nacelle and tower presented in chapter 4.3.1. For these measurements, D was defined as the diameter of the AD70, i.e., 0.7 m.

Both actuator discs were mounted with a yaw angle of 0°. Thus, the wake is assumed to be symmetrical around the centre point of the discs, i.e., y/D=0, for the transverse velocity profiles. Accordingly, only conducting measurements on half of the wake (as shown in figure 19), will be time-saving, whilst producing reliable wake profiles. Measurements are therefore taken from the centre point of the discs and outwards in the wake, in only one direction. Then, the measurements are mirrored around the disc axis to provide a full wake profile. The measurement procedure for the transverse velocity profiles is illustrated in figure 19.

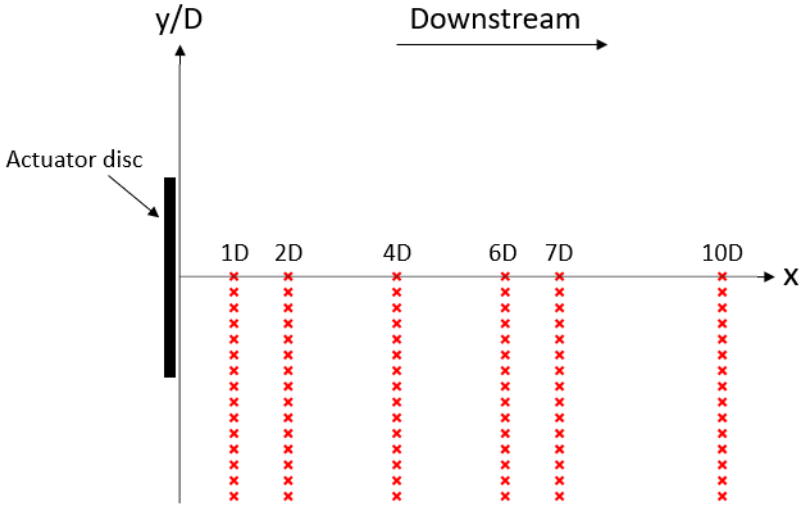

Figure 19: Illustration of measurement procedure for transverse velocity profiles (seen from above). The red crosses in the figure illustrate where measurements were conducted.

3.2.4 Measurement (D) - Vertical velocity profiles

Vertical velocity profiles were measured at 2D and 7D downstream of both actuator discs regarded in this thesis, thus quantifying both the near wake and the far wake of the discs. As opposed to the transverse velocity profiles, the vertical velocity profiles could not be assumed symmetric around the disc axis due to the impact from the tower on the upper half of the wake, i.e., the half closest to the free water surface. Therefore, measurements should ideally be taken across the entire wake.

D-1: AD70

Measuring the entire wake of the AD70, was not possible due to the limited length of the ADV cabling, as explained in chapter 3.1.3. ADV measurements could be performed at a maximum depth of 1.0 m. The AD70 could not be raised to a lower water depth, as this would mean that the wake expansion in the vertical direction would be further limited by the free water surface. This was explained in chapter 3.1.3.

Therefore, only the upper half of the wake for the AD70 could be measured. This part of the wake is affected by the tower. The measurement procedure for the vertical velocity profiles for the AD70 is illustrated in figure 20.

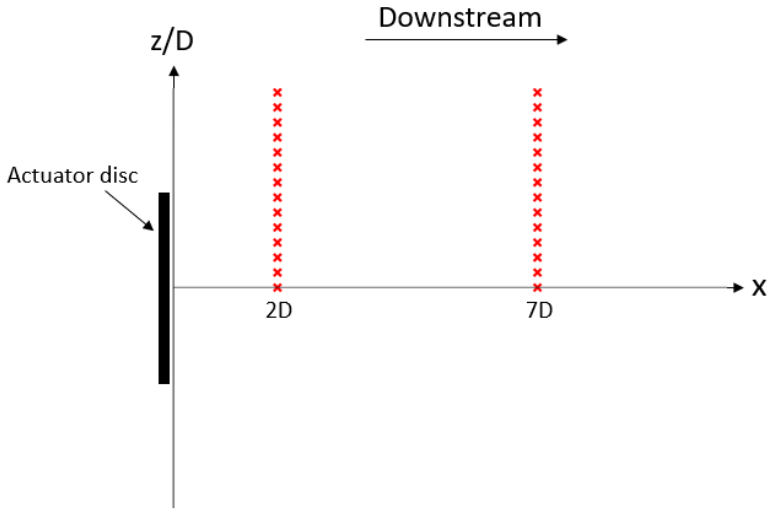

Figure 20: Illustration of measurement procedure for vertical velocity profiles of AD70 (seen from the side). The red crosses in the figure illustrate where measurements were conducted.

D-2: AD20

As explained in chapter 3.1.3, the disc centre point of both the AD70 and AD20 was located at a depth of 1.0 m for the axial and transverse velocity profiles. For the AD20, vertical velocity profiles could be measured across the entire wake. However, for this to be possible, the disc had to be raised so that the disc centre point was at a depth of 0.7 m. Accordingly, the lower half of the wake could be measured up to 1.5 disc diameters out from the disc centre point, considering the maximum measurement depth of 1.0 m. This measurement range was sufficient to give a thorough representation of the wake at 2D and 7D downstream of the disc. Raising the disc centre point to a depth of 0.7 m was assumed to have no significant impact on wake expansion in the vertical direction, as the distance from the disc centre point to the surface

would be 3.5D. The measurement procedure for the vertical velocity profiles for the AD20 is illustrated in figure 21.

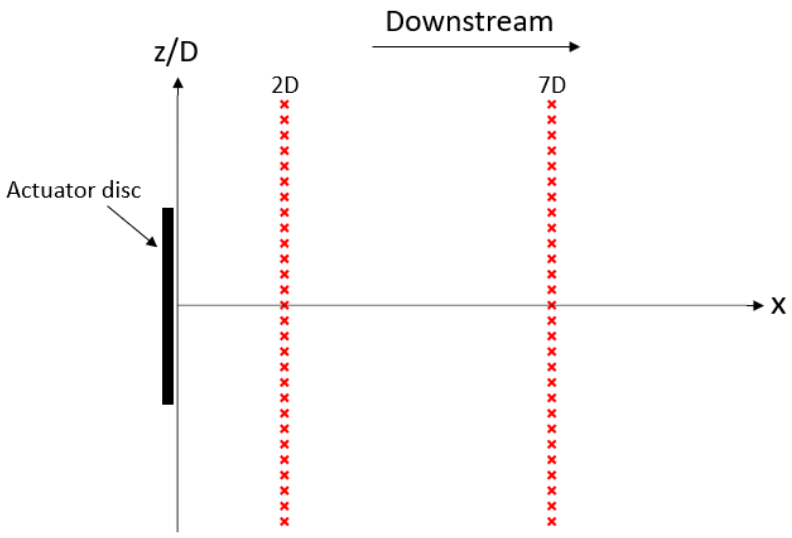

Figure 21: Illustration of measurement procedure for vertical velocity profiles of the AD20 (seen from the side). The red crosses in the figure illustrate where measurements were conducted.

3.3 Data processing

Data-processing was performed in MATLAB for all experiments conducted in the MarinLab towing tank, i.e., both force measurements and velocity measurements.

3.3.1 Force data post-processing

Axial force measurement data from the load cells were recorded via the National Instruments Compact Data Acquisition (cDAQ) system into a LabView script with a sampling frequency of 2 kHz.

Cutting the time series

The time series of the load cell force measurements was cut off at the start and end to remove the acceleration and deceleration region of the measurement series. This is illustrated in figure 22. Only the stable region of the measurement series, illustrated by a red line in figure 22, is utilised for calculation of the mean axial force.

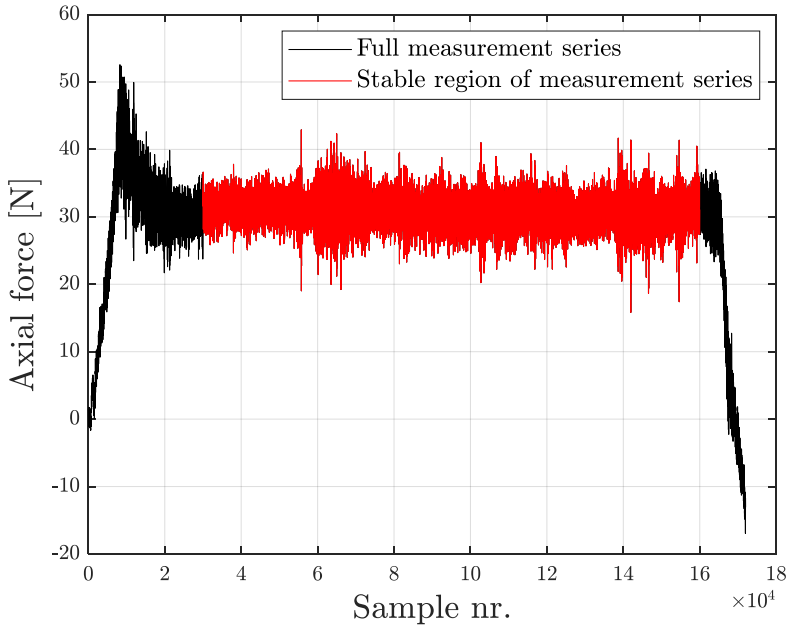

Figure 22: Cutting the axial force measurements time series. The full measurement series and the stable region of the series are illustrated by the black and red lines, respectively.

In the measurement example shown in figure 22, the start and end cuts for the measurements are at sample numbers 30,000 and 160,000, respectively, thus giving a measurement series length of 65 seconds for this mean axial force calculation.

Mean axial force and thrust coefficient

The mean axial force, F_{mean}, from a measurement series is given by

$$F_{mean} = \frac{1}{N}\sum_{i=1}^{N} F_i \tag{3.8}$$

where N is the number of measurements in the series and F_i is a measured force at a specific time.

The above equation yields the mean axial force of one measurement series. Every towing test with axial force measurements was, as previously mentioned (see chapter 3.2.1), conducted between three and five times. Therefore, the mean value of these three to five measurements series was used as the thrust force at the associated towing velocity. For the AD70, the measured tower drag was then subtracted from the total drag force on the disc and tower, which yields the drag force on the disc, referred to as thrust force in this thesis.

Finally, the thrust coefficients of the two actuator discs were calculated for each of the tested towing velocities by rearranging equation (2.14) and inserting the measured thrust force values.

3.3.2 Velocity data post-processing

Velocity measurements from the ADV Vectrino+ were recorded with a sampling frequency of 200 Hz.

Cutting of the time series

The time series of the velocity data was cut off in the same manner as for the force data explained in chapter 3.3.1, removing both the acceleration and deceleration region of the measurement series. The stable region of the measurement series is shown with a red line in figure 23.

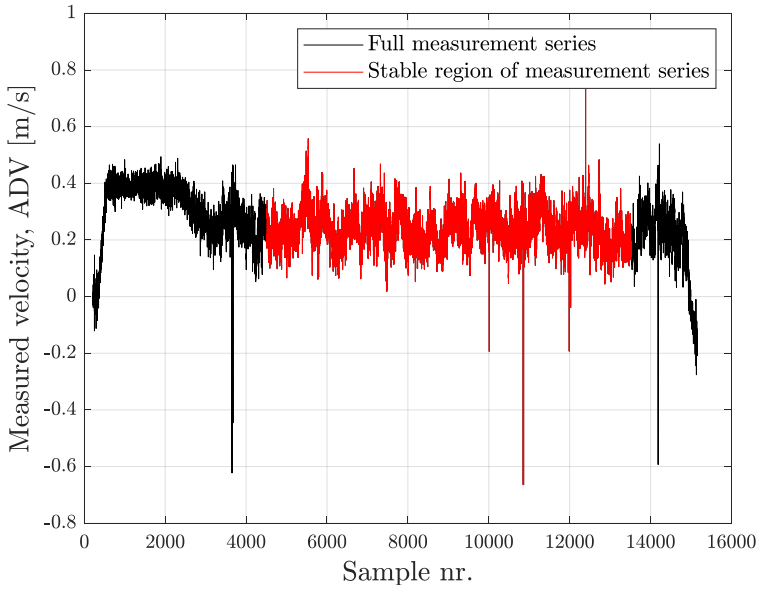

Figure 23: Cutting the ADV measurements time series. The full measurement series and the stable region of the series are illustrated by the black and red lines, respectively.

Figure 23 represents a measurement of streamwise velocity near the disc centreline (y/D=0) at a downstream distance of 4D. In this region of the wake, velocity fluctuations, as shown in figure 23, are expected. However, a stable region of the measurement series was identified and used in further data analysis. The start and end cuts for this measurement series is set to sample numbers 4,300 and 13,300, respectively, i.e., a measurement series of 45 seconds.

Figure 23 shows that the velocity accelerates from 0 to 0.4 m/s (the set towing velocity) shortly after the towing carriage starts to move and the data recording is started. Measurements are steady at 0.4 m/s until approximately sample nr. 2,500, where the ADV enters the wake of the actuator disc. At the end of the measurement series, the velocity decelerates as the towing carriage reaches the set end position in the towing tank.

The selection of start and end cuts was dependent on the downstream distance where the velocities were measured. When quantifying the far wake, the required distance between the two carriages, where the disc and ADV were mounted, implied that the distance of the towing run could not be as large as for the near wake measurements. In addition, the ADV requires more time at the start of each towing run to enter the wake of the disc when measuring the far wake compared to the near wake.

Therefore, the start and end cuts were set manually, see figure 23, for each downstream distance. Considering that this could introduce human error as an uncertainty, the sensitivity of the results due to the cutting of the time series was investigated through a sensitivity analysis in chapter 3.5.

Hampel filter

A hampel filter was applied in the data analysis on the ADV measurements in MATLAB. This filter removes unwanted spikes in the data, as illustrated in figure 24. These spikes occur when the signal from the ADV transmitter fails to hit any particles in the water, thus the signal is not reflected to the receiver arms. The hampel filter was set to remove any data points deviating more than three standard deviations from the average value of the 200 most adjacent data points. With an ADV sample frequency of 200 Hz, this means removing data points deviating from an average over one second. Only the filtered data were taken through further analysis.

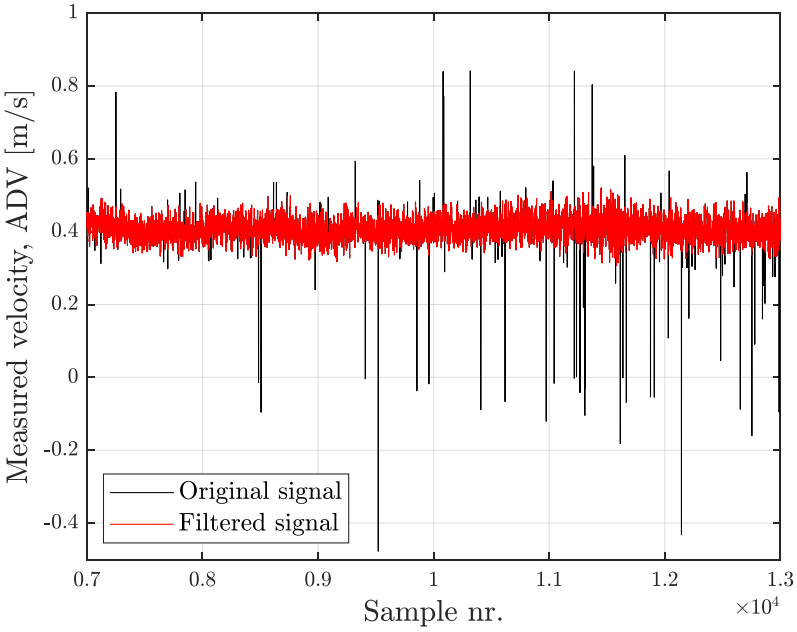

Figure 24: Velocity signal (streamwise direction) from ADV before and after addition of the hampel filter, illustrated by the black and red lines, respectively.

ADV temperature correction

The temperature sensor on the ADV probe is broken. The sensor shows a constant water temperature of -7 ℃, whereas the actual temperature in the MarinLab tank is approximately 16 ℃. As shown in equation (3.4), the ADV utilises the speed of sound in water to estimate fluid velocities. The speed of sound in water varies with temperature, resulting in a mismatch between the ADV velocity measurements and the set carriage towing velocity.

Therefore, a correction factor must be added to account for the non-functional temperature sensor. A calibration procedure, calibrating the ADV against the set towing carriage velocity, was conducted in 2021 by Bjørnsen [31]. This calibration showed mismatch between the ADV velocity measurements and the set carriage towing velocity. However, by implementing a correction factor in the MATLAB velocity data post-processing, agreement was achieved between the temperature corrected ADV velocity measurements and the set carriage towing velocity. Therefore, the same temperature correction factor was applied for the experiments regarded in this thesis. The inclusion of this temperature correction factor means that the free stream velocity, U_0, could be defined as equal to the set carriage towing velocity, i.e., 0.4 m/s, for the velocity data post-processing.

Velocity deficit

The mean velocity, U_{mean}, from a measurement series is given by

$$U_{mean} = \frac{1}{N}\sum_{i=1}^{N} U_i \tag{3.9}$$

where N is the number of measurements in the series and U_i is the measured velocity at a specific time.

The results of this thesis are presented as the non-dimensional parameter velocity deficit, $\Delta U/U_0$, defined as

$$\frac{\Delta U}{U_0} = 1 - \frac{U_{mean}}{U_0} \tag{3.10}$$

Thus, if the measured U_{mean} is equal to the free stream velocity, U_0, the velocity deficit is 0.

Turbulence kinetic energy

The turbulence kinetic energy (TKE) in the wake of the two actuator discs is found by applying equation (2.25). The TKE is commonly normalised to make the parameter independent of the incoming flow velocity. This is done by dividing the TKE by the square of the incoming flow velocity, i.e., the free stream velocity, U_0. Thus, the turbulence can be described by the non-dimensional parameter TKE/U_0^2. This is how the turbulence development in the wake of the two actuator discs will be described in this thesis.

Curve fitting and interpolation

Two types of curve fitting, as well as one interpolation method, were applied in the data post-processing in MATLAB for the measurement points from the wake investigations of this thesis.

For all the TKE profiles, an interpolation function called makima was applied to the data. By using makima, or modified Akima interpolation, a spline interpolation with low-degree polynomials is performed in each of the defined intervals and the polynomial pieces are chosen to fit smoothly together [48].

When analysing the velocity deficit profiles, the data points from the ADV were least-squares fitted with a polynomial curve to make the evaluation of the data easier and less susceptible to potentially bad measurement points. The axial velocity deficit profiles were fitted with a 7-term polynomial. All transverse and vertical velocity deficit profiles were fitted with a 12-term polynomial curve, except the vertical velocity deficit profile of the AD70 at 7D downstream. For this profile, the wake could not be sufficiently quantified due to water surface proximity, which is further explained in chapter 4.4.1. Thus, fitting a 6-term polynomial curve was more suitable for this profile.

The transverse velocity deficit profiles were also fitted with a best-fit Gaussian curve to see if the shape of these profiles follow a Gaussian curve, in accordance with theory presented in chapter 2.3.2 regarding the far wake region of a turbine. The Gaussian curves, given by equation (2.23), were fitted to the data points by using a MATLAB function provided by David Roger Lande-Sudall. The process used for fitting the Gaussian curves to the data points is clearly described by Lande-Sudall [9].

3.4 Measurement uncertainty

There are several sources of error to be aware of when conducting laboratory experiments. Due to these sources of error, there will be uncertainty associated with the measurements. Measurement errors can be split into two main categories: systematic errors and random errors [49].

Systematic errors

Systematic errors cause a shift of the measurement values away from the "true" or "accepted" value [49]. Thus, these errors influence the accuracy of the measurements, i.e., how close the measurements are to the "true" or "accepted" value. Systematic errors are typically caused by flawed calibration of instruments, imperfect experimental setup or changes in experimental conditions. The impact of these errors can be minimised through a carefully planned experimental design, and by applying proper techniques and instruments both during experiments and calibrations.

Uncertainties will be associated with the experimental setup for the experiments of this thesis, as everything is mounted by hand. Potential inaccuracies regarding the depths at which the discs and ADV are located or the distance between the discs and the ADV could influence the results.

The depth of the ADV for the vertical velocity profiles was adjusted manually. An aluminium ruler with millimetre resolution was fixed to the ADV construction for reference when adjusting the depths of the ADV. Consequently, these adjustments could, in theory, be made with millimetre precision as for the positioning of the ADV for the transverse velocity profiles using the traverse. However, the element of human error is involved in the depth adjustments, as this is done manually.

The ADV, actuator discs and load cells must be perfectly aligned with the towing direction in the MarinLab tank to avoid decomposition of both the force and velocity vector. The actuator discs should be mounted with both a yaw and tilt angle of 0°. A deviation in yaw angle will deflect the wake horizontally, whereas a tilt angle will cause a vertical deflection of the wake. In addition, the axial force on the disc will be decomposed and thus reduced in the axial direction. This effect will, however, have minimal influence on the results. If, for instance, the actuator disc was mounted with a yaw angle of 3°, the axial force measured by the load cell, $F_{T,\,red}$, would be given by

$$F_{T,red} = F_T \cos 3° = 0.99863 F_T \quad (3.11)$$

where F_T is the axial force on a disc if it was mounted with a yaw angle of 0°. Thus, a yaw angle of 3° causes the measured axial force to decrease by 0.137% compared to a disc mounted with a yaw angle of 0°. The same relation as described in equation (3.11) applies if the disc is mounted with a tilt angle of 3°.

As explained in chapter 3.1.6, particles must be suspended in the water for the ADV to provide good quality measurements. Although the suspended particles were supposed to be neutrally buoyant, the particles tended to sink slowly towards the tank bottom. Therefore, when deemed necessary, waves were applied from the wave generator for particle mixing. The degree of particle mixing could not be measured directly, however the signals from the ADV provided an indication of whether the mixing was sufficient or not. Considering that all measurements conducted through this thesis could not be performed on the same day under the exact same conditions, the data quality varied according to the seeding that was achieved on the time of recording.

Random errors

Random errors are caused by unpredictable fluctuations in the environmental conditions or in the measuring instrument [49]. These errors influence the precision of the measurements. Precision is a measure of how closely several measurement values agree, when the measurements are performed under the same conditions. Random errors are present in in every experiment and can never be eliminated. The impact of these errors can be minimised by increasing the sample size or by repeating measurements and using the mean value of these measurements.

There are unpredictable fluctuations in the environmental conditions during the experiments in the MarinLab towing tank. The particles suspended in the water, which are essential to the quality of the ADV measurements, are in continuous movement, and will therefore not be present at the same location during each run. As such, the experimental conditions will not be identical for any of the measurements. In addition, the towing carriage may experience vibrations or choppy movements as it is towed through the tank due to the wiring system. These irregular motions could transfer to the rest of the experimental setup, which is mounted on the carriage, and thus effect the measurements. Measurements are also affected to some extent by random noise, as the towing carriage and measuring equipment with associated electronics are

not built to prevent random noise. The influence from random errors is reduced in this thesis by using mean values of measurement series for both force and velocity measurements. In addition, force measurements are repeated several times, and the mean is used, to further reduce the effects of these errors.

3.4.1 Uncertainty of load cells

The two load cells utilised for the axial force measurements on the AD70 and AD20 were investigated in terms of error bar plots to get an indication of the precision of these measurements. Measurements were conducted three times at towing velocities from 0.1 m/s to 0.3 m/s, whereas at velocities from 0.4 m/s to 0.6 m/s, measurements were conducted five times.

100 N load cell for AD70

The precision of the axial force measurements on the AD70 rig will be considered for the measurements conducted on the entire rig, i.e., the total drag from the disc and tower. Finding the standard deviations of the thrust force on the disc is not possible, as this force was found by subtracting the measured tower drag from the measured total drag. Figure 25 shows the error bar plot for the axial force measurements on the disc and tower of the AD70 rig at various towing velocities.

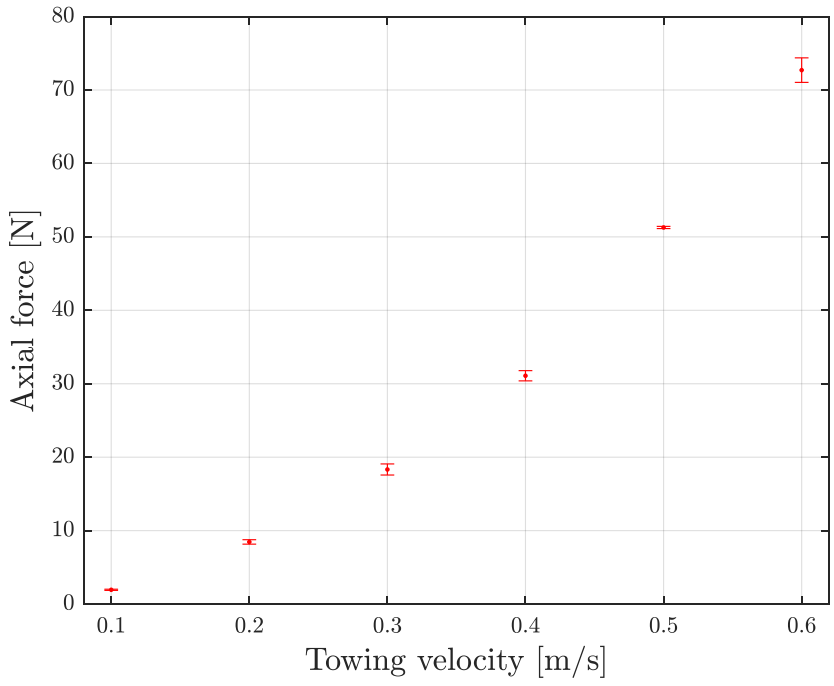

Figure 25: Axial force measurement error bar plot for the disc and tower of the AD70 rig at various towing velocities. Error bars represent the standard deviation of the measurements.

The results from figure 25 can be studied in detail in table 6, which shows the relative standard deviations of the axial force measurements.

Table 6: Relative standard deviations of the axial force measurements on the disc and tower of the AD70 rig at various towing velocities.

Tow velocity, U [m/s]	**Mean disc & tower drag [N]**	**Relative standard deviation, σ [%]**
0.1	1.94	4.16
0.2	8.46	3.56
0.3	18.33	4.12
0.4	31.09	2.24
0.5	51.28	0.29
0.6	72.71	2.30

The relative standard deviations of the axial force measurements from the 100 N load cell show that there is a relatively high uncertainty to be associated with these measurements. Results vary between runs, and the largest relative standard deviations are experienced at the lowest towing velocities. This reflects the relatively high degree of non-linearity and hysteresis observed during calibration (see chapter 3.1.5) and will also be apparent from the axial force measurement results from the AD70 presented in chapter 4.1.1.

10 N load cell for AD20

The precision of the axial force measurements on the AD20 will be investigated by studying the standard deviations of the C_T values obtained from the experiments. In figure 26, the error bar plot for the C_T values from the axial force measurements on the AD20 is shown.

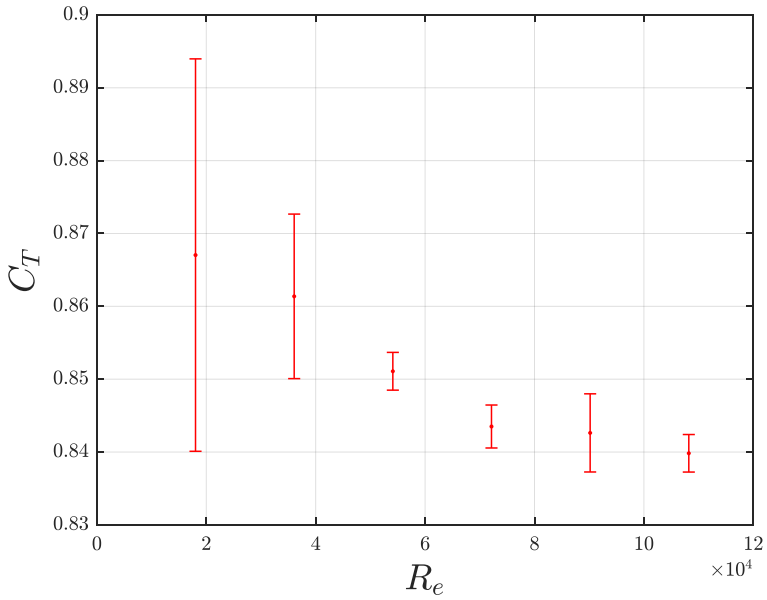

Figure 26: Error bar plot for the C_T values from axial force measurements on the AD20 with various Reynolds numbers. Error bars represent the standard deviation of the measurements.

The results from figure 26 can be studied in detail in table 7, which shows the relative standard deviations of the C_T values from the axial force measurements on the AD20.

Table 7: Relative standard deviations of the C_T values from axial force measurements on the AD20 at various towing velocities.

Tow velocity, U [m/s]	**Re**	**Mean disc thrust force [N]**	**Mean C_T**	**Relative standard deviation of C_T, σ [%]**
0.1	$1.803 \cdot 10^4$	0.14	0.87	3.11
0.2	$3.607 \cdot 10^4$	0.54	0.86	1.31
0.3	$5.410 \cdot 10^4$	1.20	0.85	0.30
0.4	$7.214 \cdot 10^4$	2.12	0.84	0.35
0.5	$9.017 \cdot 10^4$	3.31	0.84	0.64
0.6	$1.082 \cdot 10^5$	4.74	0.84	0.31

As for the 100 N load cell measurements on the AD70, the 10 N load cell experiences largest relative standard deviations at the lowest towing velocities. At towing velocities 0.1 m/s and 0.2 m/s, relative standard deviations are 3.11% and 1.31%, respectively. Standard deviations are significantly smaller at towing velocities between 0.3 m/s and 0.6 m/s, varying from 0.30% to 0.64%.

Notably, the standard deviations are smaller for the 10 N load cell compared to the 100 N load cell. This agrees with load cell calibrations, as presented in chapter 3.1.5, and is also reflected when comparing the results from the axial force measurements on the AD70 and AD20 in chapter 5.1.

3.4.2 Uncertainty of ADV

The precision of the ADV measurements is not constant throughout the wake. For example, the precision is not the same if the measurement point is behind the centre of the disc or behind the edges of the disc. In addition, the precision varies with the downstream distance from the disc. Bjørnsen [31] and Aasnæs [47] conducted experiments in the MarinLab towing tank investigating the precision of the streamwise velocity measurements from the ADV in the wake. Both Bjørnsen and Aasnæs conducted measurements behind the disc centre point, and at two different positions located behind the edges of the disc. Measurements were repeated multiple times for each measurement point so that the precision of the ADV measurements could be calculated for each point. The results from these experiments are relevant for this thesis, as the exact same ADV is used for wake measurements.

Bjørnsen [31] performed measurements in the wake of an array consisting of three trapezoidal holed actuator discs with diameters of 0.2 m and solidities of 57%. Measurements were taken in the near wake, at a downstream distance of 2.5D, and resulted in relative standard deviations varying from 2.60% to 9.85%. Aasnæs [47] conducted experiments in the wake of a small wind farm setup consisting of seven trapezoidal holed actuator discs with diameters of 0.2 m and solidities of 57%. However, these measurements were taken at 8D downstream of the discs, i.e., in the far wake. The measurements performed by Aasnæs resulted in relative standard deviations varying from 0.11% behind the disc centre point to 1.86% behind the edge of the disc.

The results from Bjørnsen [31] and Aasnæs [47] indicate that the uncertainty of the ADV measurements is related to the level of turbulence at the point of measuring. The relative standard deviations found by Bjørnsen at 2.5D downstream were considerably larger than those found by Aasnæs at 8D downstream, where the turbulence level is significantly lower. In addition, the results from Aasnæs showed that the relative standard deviations were largest behind the edges of the disc, which are the areas in the wake with the highest turbulence levels.

As such, there are indications that the uncertainty of the ADV measurements increases as the level of turbulence increases.

3.5 Effects of time series cutting on ADV measurements

The length of the measurement series for the wake investigations in the MarinLab towing tank were limited due to the length of the towing tank (50 m), in addition to the acceleration and deceleration time for the towing carriage and the stabilization time for the ADV measurements. Results from the wake investigations of this thesis were averaged over measurements series ranging from 28 to 50 seconds, depending on the downstream distance where the velocities were measured. Longer measurements series would be preferable, as it reduces the sensitivity of the results to the cutting of the time series, i.e., the region of the measurement series on which the analysis is to be based.

Therefore, the sensitivity of the results due to the cutting of the time series was investigated through a sensitivity analysis. The analysis studies the deviations in the measured mean streamwise velocity, U_{avg}, and TKE, at 1D and 7D downstream of the AD70, from the value of the originally selected time series length when the time series is shortened. The time series was shortened by changing the start cut for the measurement series, whilst maintaining the same end cut.

Mean streamwise velocity

The deviation in measured mean streamwise velocity between the originally selected time series length and various shortened time series lengths from measurements at 1D and 7D downstream of the AD70 are presented in figures 27 and 28, respectively.

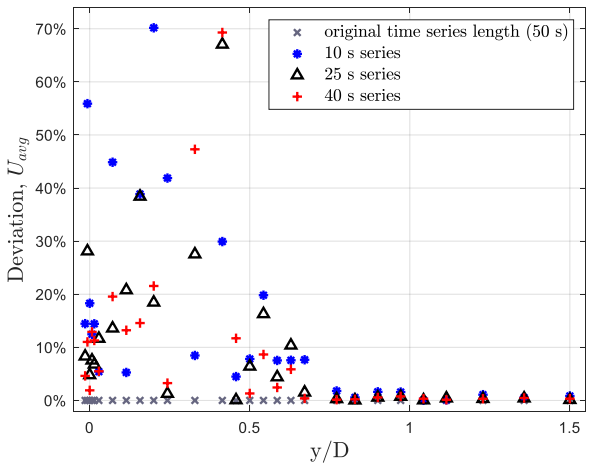

Figure 27: Deviation in U_{avg} with various time series lengths, 1D downstream of the AD70.

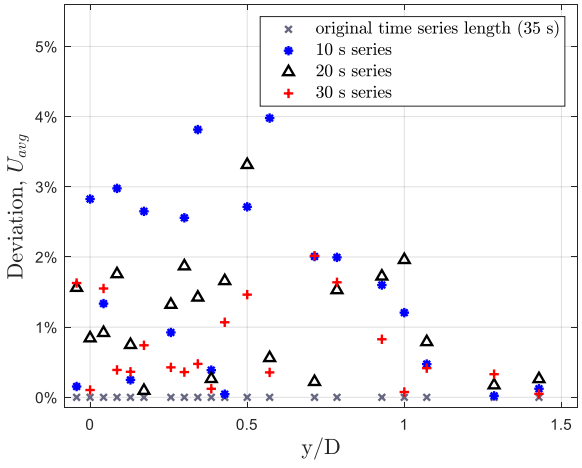

Figure 28: Deviation in U_{avg} with various time series lengths, 7D downstream of the AD70.

The above figures shows that the cutting of time series has significantly more impact on the results when conducting measurements in the near wake of the disc compared to the far wake. The maximum deviation in measured mean streamwise velocity at 1D and 7D were found to be 70.2% and 4.0%, respectively. In addition, the deviation in U_{avg} is clearly shown to be greater within the wake of the disc than outside the wake.

Turbulence kinetic energy

Figures 29 and 30 presents the deviation in measured mean TKE between the originally selected time series length and various shortened time series lengths from measurements at downstream distances of 1D and 7D, respectively.

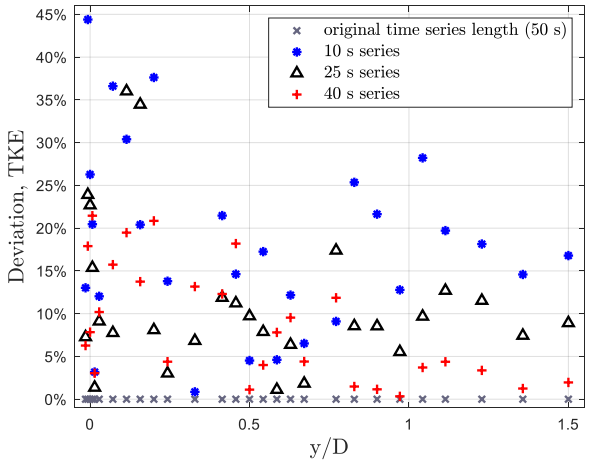

Figure 29: Deviation in TKE with various time series lengths, 1D downstream of the AD70.

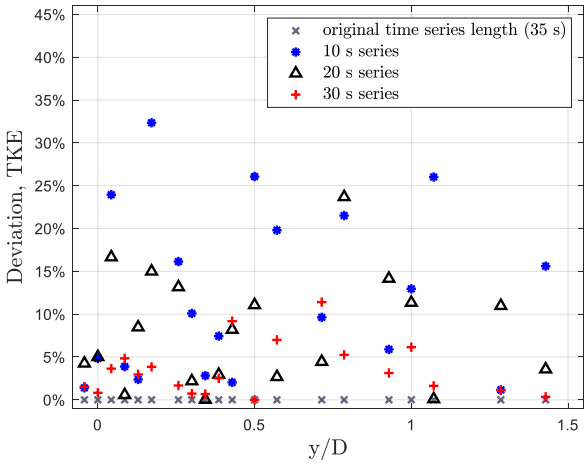

Figure 30: Deviation in TKE with various time series lengths, 7D downstream of the AD70.

The results from this analysis are not as conclusive as the sensitivity analysis on U_{avg}. The deviation in TKE appeared to be relatively similar at the two selected downstream distances. The maximum deviation in measured mean TKE at 1D and 7D were found to be 44.4% and 32.4%, respectively. The turbulence levels at 1D are significantly higher compared to the turbulence levels at 7D. As this analysis investigates the deviation in TKE relative to the measured value at each point with the original time series length, a small difference in TKE will have a significant impact on the deviation in regions where the TKE values are low, i.e., outside the wake or in the far wake. Thus, the deviations in TKE appear to be relatively high at both downstream distances, whether measurement points are located within the wake or outside the wake.

4 Results

Results from the experiments in the MarinLab towing tank are presented in this chapter. The experiments include measurement (A) - axial force measurements, (B) - axial velocity profiles, (C) - transverse velocity profiles and (D) - vertical velocity profiles, for both the AD70 and the AD20. Furthermore, measurements of transverse velocity profiles were conducted for the rig of the AD70 without the disc mounted on the nacelle. Notably, the transverse velocity measurements were only performed on one half of the wake and mirrored around y/D=0, as explained in chapter 3.2.3.

For the transverse velocity profiles of both actuator discs, the turbulence kinetic energy level was measured to approximately $8 \cdot 10^{-4}$ $m^2 s^{-2}$ at all measurement points located outside the wake of the discs. This turbulence level is insignificantly small in relation to the scale, and it is a reasonable approximation for the inflow turbulence level for all the experiments conducted through this thesis. As such, all experiments are considered to be performed under laminar inflow conditions.

4.1 Measurement (A) - Axial force measurements

4.1.1 A-1: Actuator disc 70 cm diameter

As shown in equation (2.14), the axial force on the disc is dependent on the square of the incoming fluid velocity. Therefore, by doubling the towing velocity, the axial force should, in theory, be quadrupled. This theory was reflected by the results from the axial force measurements on the AD70, as shown in figure 31.

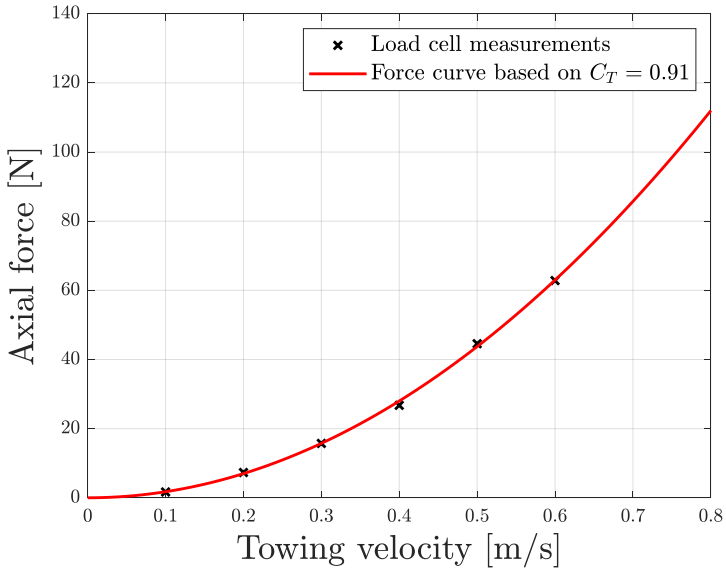

Figure 31: Measured axial force on the AD70 as a function of towing velocity.

In figure 31, the measured axial forces at different towing velocities are presented with a theoretical thrust force curve, applying equation (2.14), for an actuator disc based on a thrust coefficient of 0.91 (displayed as a red line). This thrust coefficient was chosen based on the average thrust coefficient from the experiments on the AD70. As shown in table 8, C_T values for the AD70 at different towing velocities ranged from 0.87 to 0.95, resulting in an average thrust coefficient of 0.91.

The thrust coefficient was shown to be independent of Reynolds number, as illustrated in figure 32. This supports the theory presented in chapter 2.2.2, stating Reynolds independence for drag coefficients approximately when Re>1000.

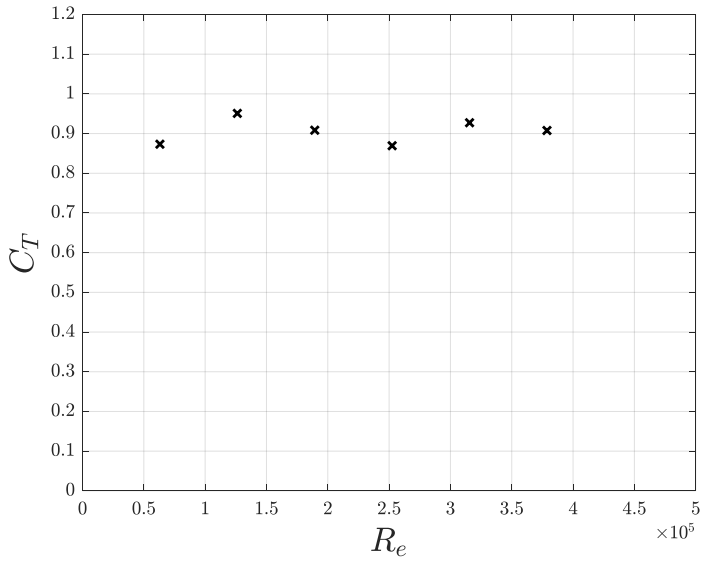

Figure 32: C_T values from axial force measurements on the AD70 as a function of Reynolds number.

The results from the axial force measurements on the AD70 are summarised in table 8.

Table 8: Axial force measurements on the AD70.

Tow velocity, U [m/s]	Re	Disc & tower drag [N]	Tower drag [N]	Disc thrust force [N]	Disc, C_T
0.1	$6.312 \cdot 10^4$	1.94	0.26	1.68	0.87
0.2	$1.262 \cdot 10^5$	8.46	1.15	7.31	0.95
0.3	$1.894 \cdot 10^5$	18.33	2.61	15.72	0.91
0.4	$2.525 \cdot 10^5$	31.09	4.35	26.74	0.87
0.5	$3.156 \cdot 10^5$	51.28	6.71	44.57	0.93
0.6	$3.787 \cdot 10^5$	72.71	9.89	62.82	0.91

4.1.2 A-2: Actuator disc 20 cm diameter

The results from the axial force measurements on the AD20 are presented in figure 33. As for the AD70, the axial force on the AD20 was shown to be dependent on the square of the incoming fluid velocity.

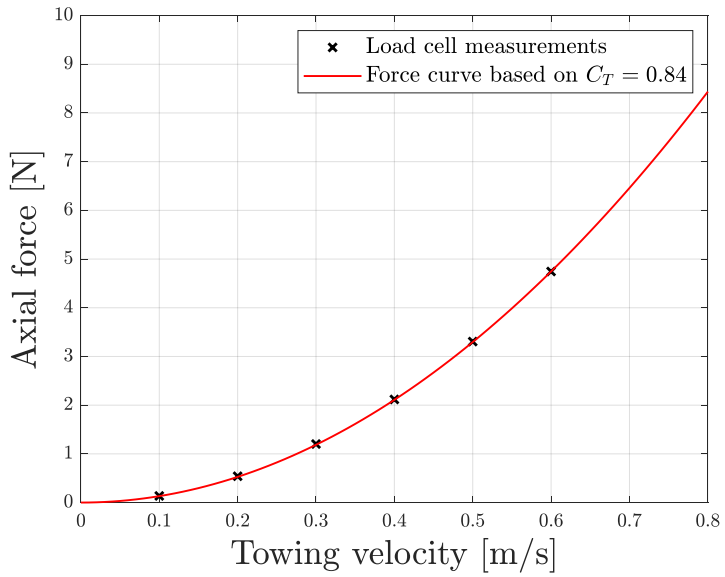

Figure 33: Measured axial force on the AD20 as a function of towing velocity.

The measured axial forces on the AD20 at different towing velocities are presented in figure 33 with a theoretical thrust force curve based on a thrust coefficient of 0.84 (displayed as a red line). Thrust coefficients at different towing velocities for this disc were found to be ranging from 0.84 to 0.87. See table 9.

By plotting the C_T values against Reynolds number, see figure 34, it was shown that the thrust coefficient of the disc is independent of Reynolds number at towing velocities of 0.4 m/s or above, i.e., Re $\geq 7.214 \cdot 10^4$. The thrust coefficient of the disc was constant at 0.84 when Reynolds independence was achieved. Measurements conducted in the region without Reynolds independence, i.e., at towing velocities below 0.4 m/s, produced slightly higher C_T values. Towing velocities of 0.1, 0.2 and 0.3 m/s resulted in C_T values of 0.87, 0.86 and 0.85, respectively.

In figure 33, a theoretical thrust force curve based on the Reynolds independent C_T of 0.84 was used for comparison with the measured axial forces, as this C_T value was considered the best estimate for the thrust coefficient of the AD20.

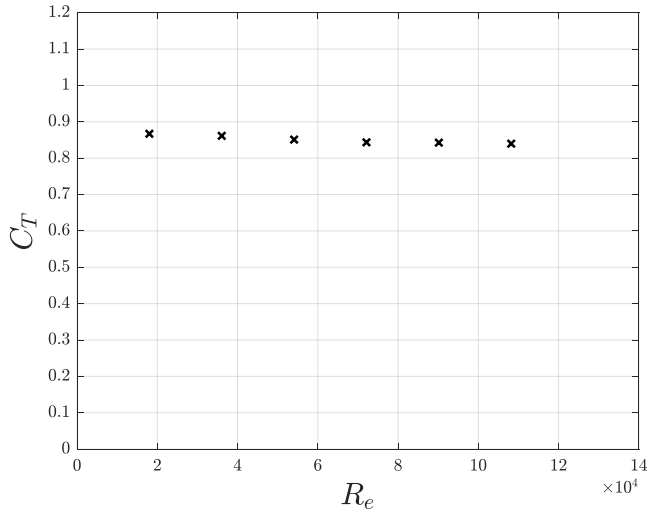

Figure 34: C_T values from axial force measurements on the AD20 as a function of Reynolds number.

In table 9, the results from the axial force measurements on the AD20 are summarised.

Table 9: Axial force measurements on the AD20.

Tow velocity, *U* [m/s]	**Re**	**Disc thrust force [N]**	**Disc, C_T**
0.1	$1.803 \cdot 10^4$	0.14	0.87
0.2	$3.607 \cdot 10^4$	0.54	0.86
0.3	$5.410 \cdot 10^4$	1.20	0.85
0.4	$7.214 \cdot 10^4$	2.12	0.84
0.5	$9.017 \cdot 10^4$	3.31	0.84
0.6	$1.082 \cdot 10^5$	4.74	0.84

4.2 Measurement (B) - Axial velocity profiles

4.2.1 B-1: Actuator disc 70 cm diameter

Velocity deficit

The measured axial velocity deficit in the wake of the AD70, from 1-10D downstream, is shown in figure 35, with a 7-term polynomial least-squares fitted curve.

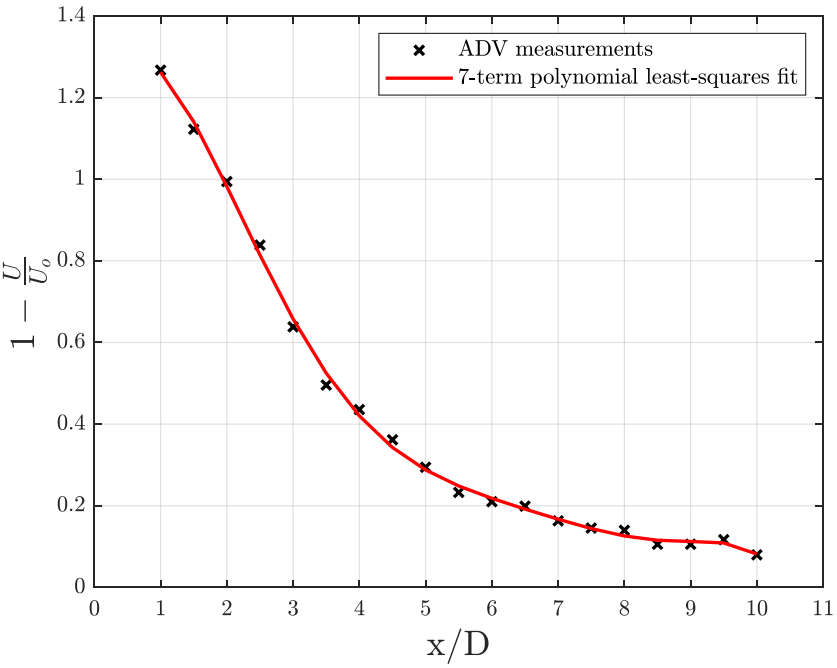

Figure 35: Axial velocity deficit profile for the AD70.

Figure 35 illustrates the wake recovery downstream of the AD70 along the disc centreline. The velocity deficit is largest at 1D downstream, with a velocity deficit of 126.7%. A velocity deficit above 100% means that there are regions of reversed flow in the wake. The measurements show that reversed flow occurs along the centreline in the wake of the AD70 when x<2D. As the ADV is moved further downstream of the disc, the velocity in the wake increases towards the free stream velocity, i.e., the velocity deficit decreases towards 0. At a downstream distance of 10D, the flow has almost regained free-stream velocity, with a velocity deficit of 8.0%. If measurements were taken further than 10D downstream of the disc, the velocity deficit is expected to continue decreasing.

Turbulence kinetic energy

In figure 36, the axial non-dimensional TKE profile in the wake of the AD70 is shown with a makima interpolation curve fitted to the measurement points.

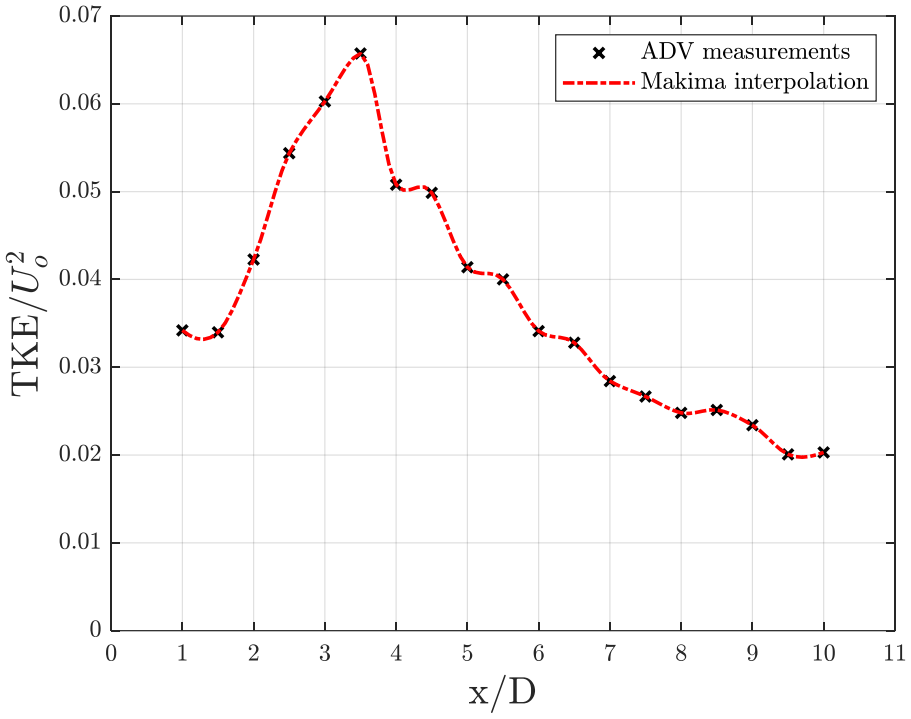

Figure 36: Axial non-dimensional turbulence kinetic energy (TKE/U_0^2) profile for the AD70.

Figure 36 shows that the TKE increases downstream along the disc centreline from 1D and peaks at 3.5D. Then, the TKE decreases towards the ambient turbulence level as the measurements are conducted further downstream of the disc. The TKE is expected to continue decreasing if measurements were taken further than 10D downstream of the disc.

4.2.2 B-2: Actuator disc 20 cm diameter

Velocity deficit

In figure 37, the measured axial velocity deficit in the wake of the AD20, from 1-10D downstream, is presented with a 7-term polynomial curve least-squares fitted to the measurement points.

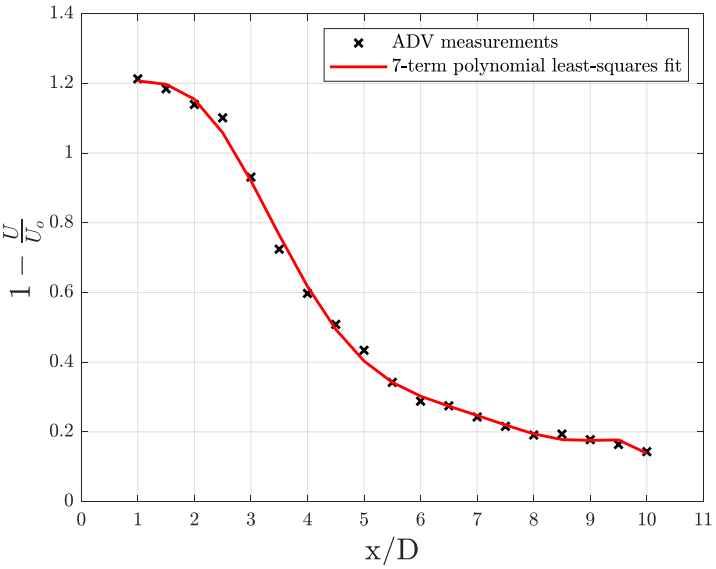

Figure 37: Axial velocity deficit profile for the AD20.

Reversed flow is observed between 1D and 2.5D downstream of the AD20 along the disc centreline, with a maximum velocity deficit of 121.3% measured at 1D. The velocity deficit in the wake decreases as the ADV is moved further downstream of the disc. A velocity deficit of 14.3% was measured at 10D downstream. The velocity in the wake will continue recovering towards the free stream velocity further downstream.

Turbulence kinetic energy

The axial non-dimensional TKE profile in the wake of the AD20 is presented in figure 38 with a makima interpolation curve fitted to the data points.

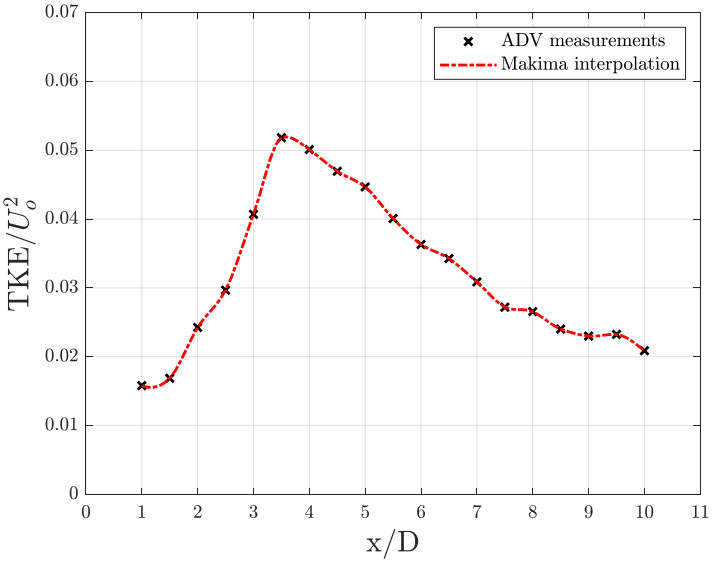

Figure 38: Axial non-dimensional turbulence kinetic energy (TKE/U_0^2) profile for the AD20.

As shown in figure 38, the lowest level of turbulence along the disc centreline occurred at 1D downstream of the AD20. This would perhaps not be the case if measurements were extended to more than 10D downstream, considering that the TKE is shown to be on a decreasing trajectory at 10D. The TKE increases with downstream distance from 1D to 3.5D, where the peak value occurs. From 3.5-10D, the TKE is shown to decrease with downstream distance.

4.3 Measurement (C) - Transverse velocity profiles

4.3.1 C-1: Actuator disc 70 cm diameter

Velocity deficit

The transverse velocity deficit profiles from the towing tests on the AD70 are presented in figure 39. The velocity measurements from the ADV are presented with a 12-term least-squares fitted polynomial curve and a best-fit Gaussian curve.

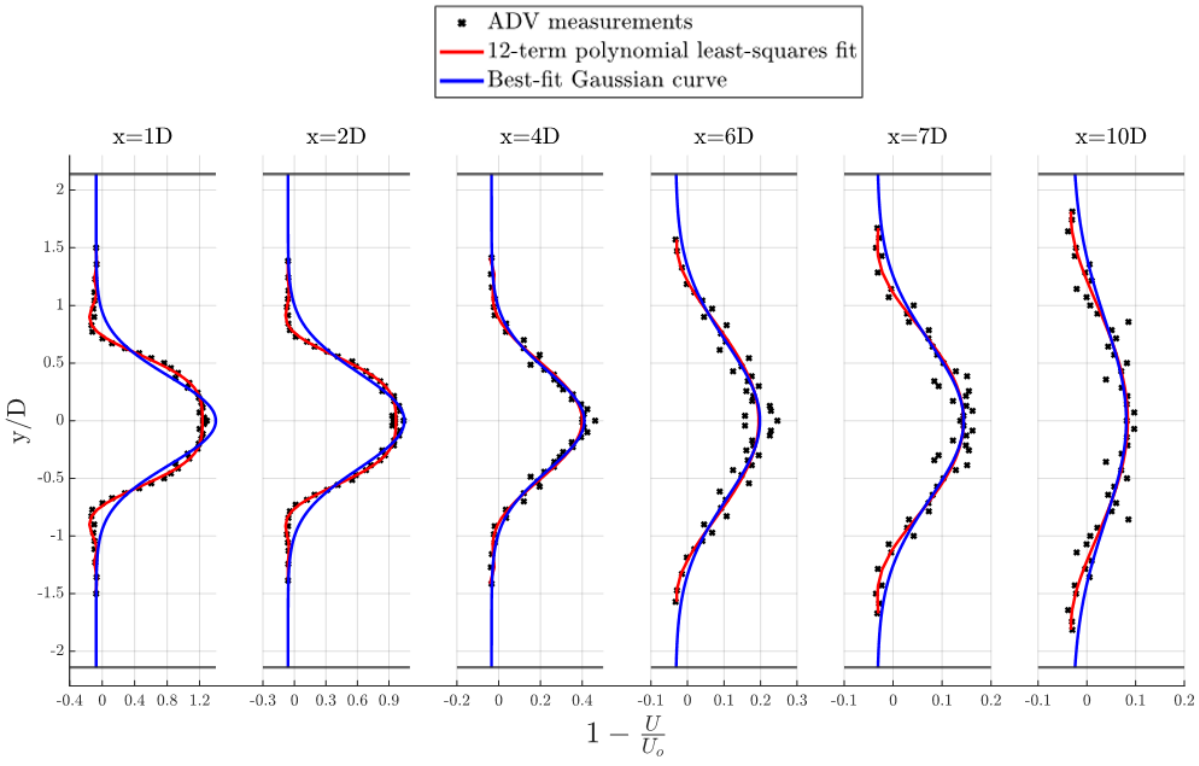

Figure 39: Transverse velocity deficit profiles for the AD70. The grey horizontal lines at y/D=2.14 and y/D=-2.14 marks the tank side walls.

The results show that a Gaussian curve does not represent the velocity deficit profiles successfully at 1D and 2D downstream of the disc. However, from 4D and further downstream, the wake can effectively be represented by a Gaussian curve. This agrees with theory presented in chapter 2.3.2, stating that the far wake velocity distribution follows a Gaussian profile. As such, the wake appears to be fully developed at 4D, meaning that the far wake region can be defined from 4D. Transverse profiles were not recorded at downstream distances between 2D and 4D, thus the exact downstream position where the near wake ends could not be determined.

In the near wake of the actuator disc, the wake is narrow and there is a large velocity deficit. Both at 1D and 2D downstream, regions of reversed flow were detected near the disc centreline. This can be observed in the figure 39 where $1 - \frac{U}{U_0} > 1$.

In the far wake, however, the wake is wider, and the velocity deficit is smaller compared to the near wake. Thus, the transverse velocity deficit profiles demonstrate wake recovery and expansion. The wake expansion of the AD70 will be analysed in chapter 5.3 and compared with the AD20.

The transverse velocity deficit profiles show an increased velocity (relative to the free stream velocity) outside the wake, i.e., a bypass velocity, due to the blockage from the disc. This bypass velocity can be observed in figure 39 where $1 - \frac{U}{U_0} < 0$.

Table 10 presents the maximum relative velocity deficit, $\Delta U_{max}/U_0$, and bypass velocity, $U_{b,max}/U_0$, from the transverse velocity deficit profiles of the AD70. The table values represent the ADV measurement points. The measurements show a significant increase in the flowing velocity around the disc in the near wake region with an increased velocity of 13.2% relative to the free stream velocity at 1D downstream. In the far wake, from 4-10D, the increase in velocity outside the wake is less significant, varying from 3.2-3.9%.

Table 10: Maximum relative velocity deficit, $\Delta U_{max}/U_0$, and bypass velocity, $U_{b,max}/U_0$, from the transverse velocity deficit profiles of the AD70. Values represent the ADV measurement points.

Downstream distance	$\frac{\Delta U_{max}}{U_0}$	$\frac{U_{b,max}}{U_0}$
1D	1.289	1.132
2D	1.040	1.072
4D	0.462	1.037
6D	0.246	1.032
7D	0.162	1.035
10D	0.097	1.039

Turbulence kinetic energy

The transverse non-dimensional TKE profiles for the AD70 are shown in figure 40 with makima interpolation curves fitted to the measurement points.

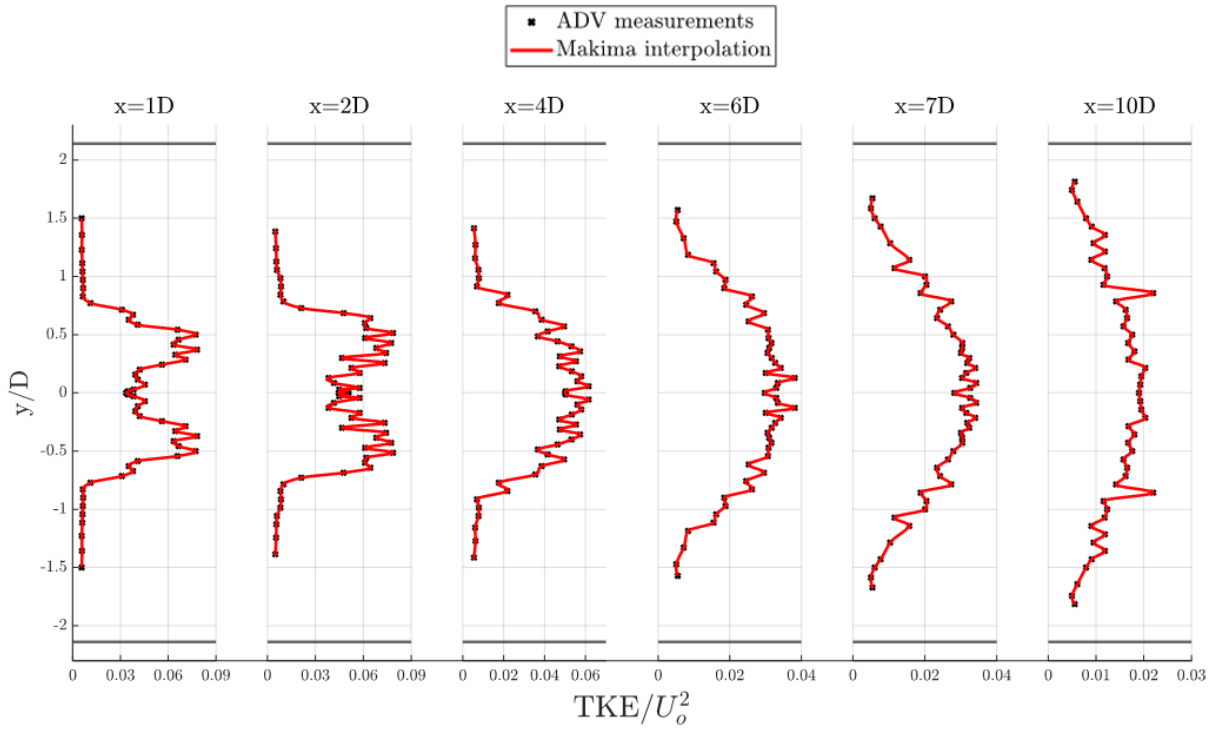

Figure 40: Transverse non-dimensional turbulence kinetic energy (TKE/U_0^2) profiles for the AD70. The grey horizontal lines at y/D=2.14 and y/D=-2.14 marks the tank side walls.

Figure 40 shows that the TKE peaks behind the edges of the disc, i.e., at y/D=±0.5D, in the near wake, at 1D and 2D downstream. The TKE profiles in the near wake have M-shaped curves,

which is characteristic for turbines due to tip vortices and for actuator discs due to vortices that are created at the disc edges. Because of turbulent mixing, the vortices break down and the curve ceases to be M-shaped further downstream, which is apparent from the TKE profiles between 4-10D. As the wake recovers with downstream distance, the TKE is shown to decrease.

In addition, wake expansion is demonstrated by the TKE profiles in figure 40. The width of the region with increased TKE is shown to increase as the distance downstream of the disc increases.

Velocity deficit from nacelle and tower

Experiments investigating the impact of the nacelle and tower on the transverse and axial velocity profiles of the AD70 was conducted by towing the actuator disc rig through the tank without the disc mounted on the nacelle. The resulting transverse velocity deficit profiles from these towing experiments are shown in figure 41. Notably, D was defined as the diameter of the AD70, i.e., 0.7 m, for these measurements. The diameter of the tower is 50 mm (0.071D).

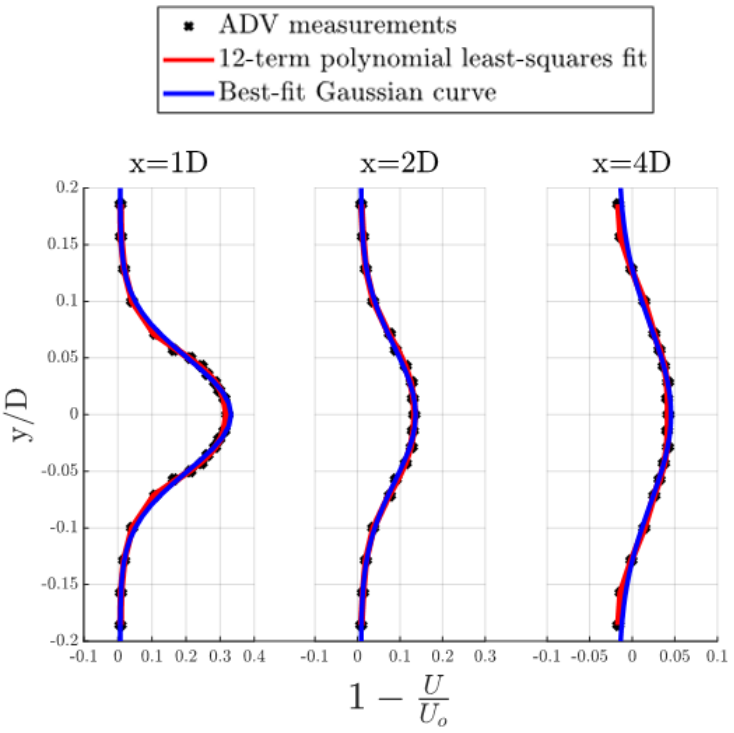

Figure 41: Transverse velocity deficit profiles for the nacelle and tower of the AD70.

The transverse velocity deficit profiles from figure 41 show that the nacelle and tower could have a significant impact on the velocity deficit profiles of the AD70 near the centre of the disc both at 1D and 2D, with maximum velocity deficits of 32.1% and 13.4%, respectively. At 4D,

however, the velocity in the wake has almost recovered to the free stream velocity, with a maximum velocity deficit of 4.3%. The contribution from the nacelle and tower to the velocity deficit profiles of the AD70 is not of the same magnitude as those presented in figure 41. When the disc is mounted on the nacelle, the disc is the first obstruction to the flow, and will therefore be the main contributor to velocity deficit in the wake. Thus, the contribution from the nacelle and tower are significantly reduced compared to the case without the disc mounted on the nacelle. The impact from the nacelle and tower on the velocity deficit in the wake of the AD70 becomes apparent when comparing the axial velocity deficit profiles of the AD70 and AD20 in chapter 5.2.

Turbulence kinetic energy from nacelle and tower

The transverse non-dimensional TKE profiles for the nacelle and tower of the AD70 are shown in figure 42 with makima interpolation curves fitted to the data points.

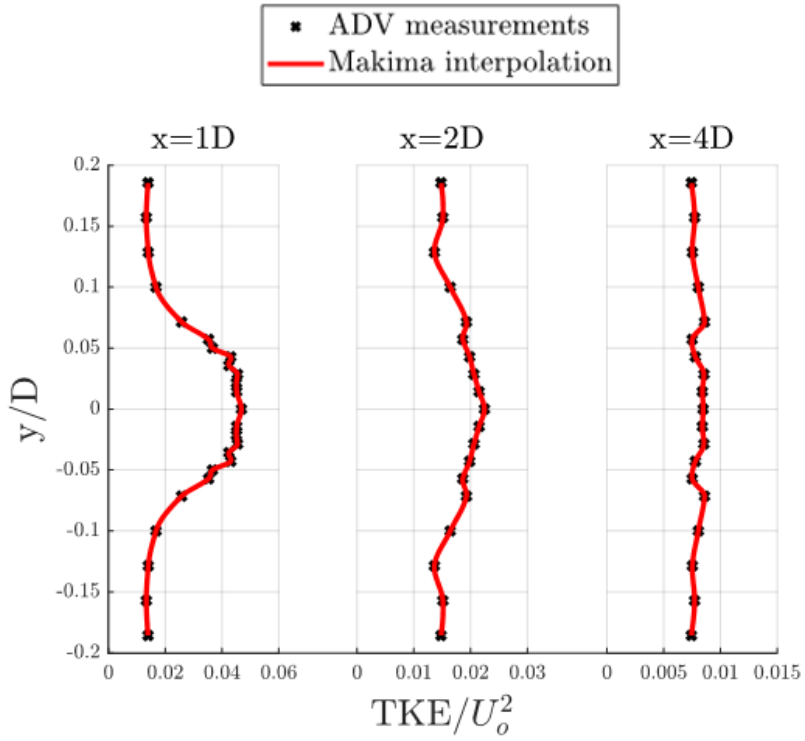

Figure 42: Transverse non-dimensional turbulence kinetic energy (TKE/U_0^2) profiles for the nacelle and tower of the AD70.

Figure 42 shows that the TKE in the wake peaks at the centreline of the nacelle (y/D=0) both at 1D and 2D, with maximum TKE/U_0^2 values of 0.047 and 0.022, respectively. At all

downstream distances, measurements were conducted from the nacelle centreline to y/D=0.186 and mirrored around y/D=0.

In the transverse position furthest from the nacelle centreline, i.e., y/D=±0.186, TKE/U_0^2 values were found to be 0.014, 0.015 and 0.007 at 1D, 2D and 4D, respectively. However, from the transverse TKE profiles of the AD70 shown in figure 40, the TKE/U_0^2 values were found to be approximately 0.005 in the areas outside the wake at all downstream distances. This suggests that the transverse velocity profiles of the nacelle and tower were not measured to a sufficient transverse distance from the nacelle centreline to fully quantify the areas of increased turbulence induced by the tower and nacelle.

Measurements were not taken at a further transverse distance (y/D) from the nacelle centreline as the velocity deficit profiles at all downstream distances (see figure 41) indicated that the entire wake was quantified. Conducting measurements to a further transverse distance (y/D) would be interesting in order to see whether the turbulence decreases or remains at an elevated level.

The TKE profiles of the nacelle and tower, indicate that the impact of the nacelle and tower on the TKE profiles of the AD70 could be significant at downstream distances of 1D and 2D. At 4D, however, these effects are expected to be less apparent. The turbulence contribution from the nacelle and tower is clearly reflected in the results when comparing the axial, transverse and vertical TKE profiles of the AD70 and AD20 in chapters 5.2, 5.3 and 5.4, respectively.

4.3.2 C-2: Actuator disc 20 cm diameter

Velocity deficit

In figure 43, the transverse velocity deficit profiles from the experiments on the AD20 are presented with 12-term least-squares fitted polynomial curves and best-fit Gaussian curves.

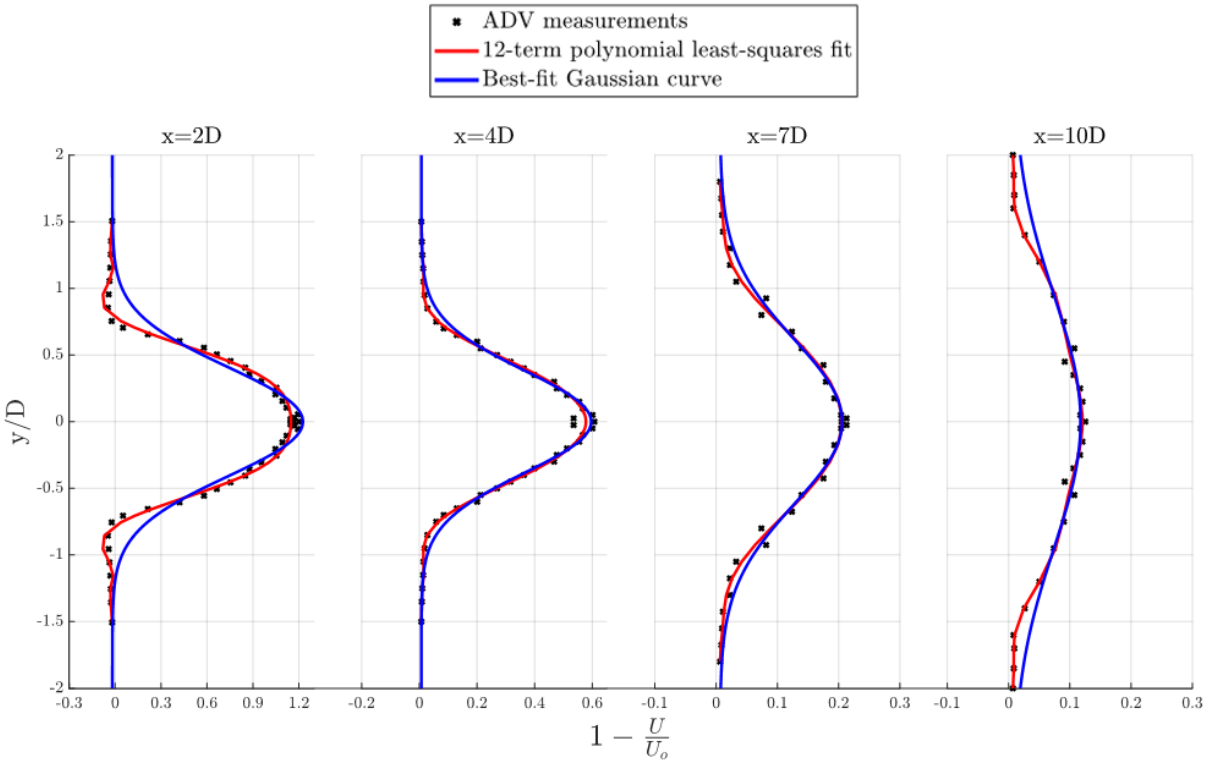

Figure 43: Transverse velocity deficit profiles for the AD20.

As shown in figure 43, the velocity distribution in the wake of the AD20 is effectively represented by a Gaussian curve at downstream distances of 4D, 7D and 10D. Therefore, the wake is considered fully developed at 4D, i.e., the far wake region is considered from 4D and further downstream. The exact end of the near wake region could not be defined as transverse profiles were not recorded between 2D and 4D downstream.

The largest velocity deficit occurred in the near wake, with regions of reversed flow observed near the disc centreline at 2D downstream. The velocity deficit in the wake decreased with increasing downstream distance, reflecting the wake recovery. Wake expansion could also be observed as the width of the wake was larger in the far wake compared to the near wake. This will be analysed in chapter 5.3, where the development of the half-wake width with downstream distance is compared for the AD70 and AD20.

The maximum relative velocity deficit, $\Delta U_{max}/U_0$, and bypass velocity, $U_{b,max}/U_0$, from the transverse velocity deficit profiles of the AD20 are presented in table 11. A maximum increase in fluid velocity of 4.8% relative to the free stream velocity was observed around the AD20 at 2D downstream. From 4-10D, however, the bypass velocity was in fact between 0.6-0.7% lower than the defined free stream velocity of 0.4 m/s. This could be consequence of not measuring the wake to a transverse position with a sufficient distance from the disc centreline in order for

the measurement point to be outside the wake, i.e., all measurement points are within the wake and therefore experiences reduced flowing velocities. Another explanation could be that there is a mismatch between the set towing velocity of the carriage and the velocity measurements from the ADV. However, the results indicate that the bypass velocity of the AD20 is approximately equal to the free stream velocity. This is reasonable considering that the blockage ratio of the AD20 is only 0.5%.

Table 11: Maximum relative velocity deficit, $\Delta U_{max}/U_0$, and bypass velocity, $U_{b,max}/U_0$, from the transverse velocity deficit profiles of the AD20. Values represent the ADV measurement points.

Downstream distance	$\frac{\Delta U_{max}}{U_0}$	$\frac{U_{b,max}}{U_0}$
2D	1.202	1.048
4D	0.607	0.993
7D	0.213	0.994
10D	0.125	0.993

Turbulence kinetic energy

Figure 44 shows the transverse non-dimensional TKE profiles for the AD20 with makima interpolation curves fitted to the data points.

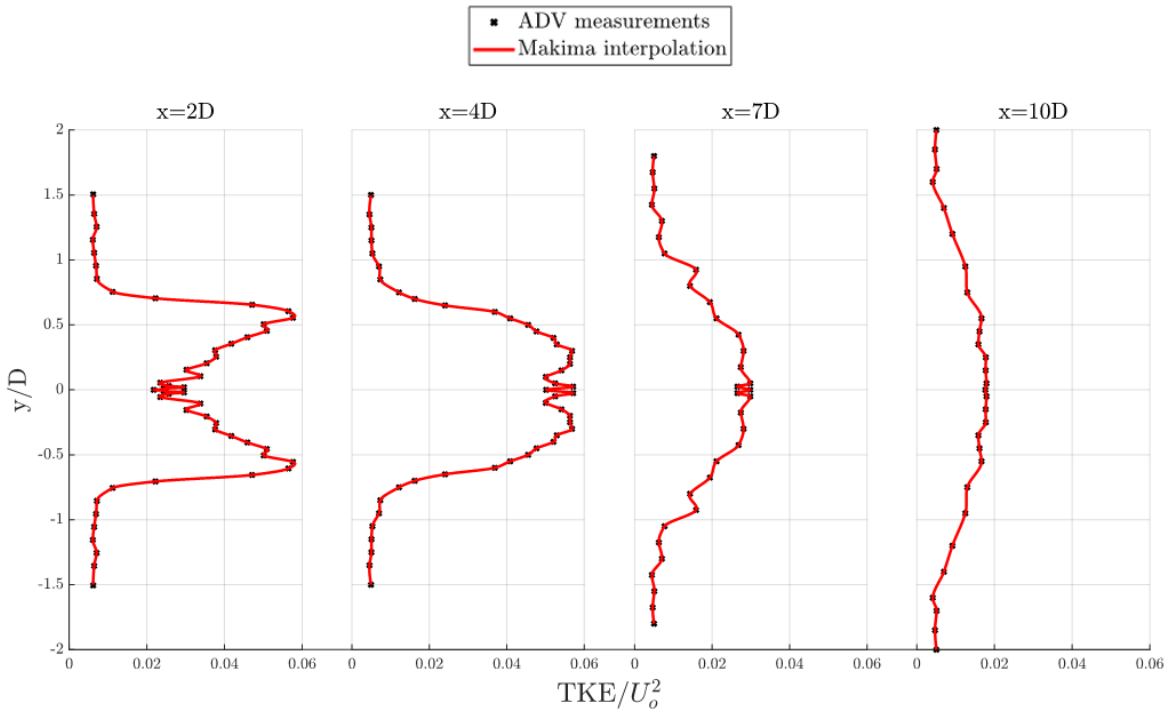

Figure 44: Transverse non-dimensional turbulence kinetic energy (TKE/U_0^2) profiles for the AD20.

The TKE at 2D downstream of the AD20 peaks behind the edges of the disc, i.e., at y/D=±0.5D, thus forming the characteristic M-shaped turbulence curve from turbines and actuator discs. Further downstream, turbulent mixing causes the vortices created at the disc edges to break down. However, at 4D downstream, these vortices are not completely broken down, and the M-shape of the TKE curve can still be detected. At 7D and 10D downstream, the TKE curve is no longer M-shaped, and the turbulence level is significantly lower compared to the near wake. In the far wake region, the measurements show an increasing wake width and a decreasing level of turbulence as the wake recovers with downstream distance.

4.4 Measurement (D) - Vertical velocity profiles

4.4.1 D-1: Actuator disc 70 cm diameter

Velocity deficit

The vertical velocity deficit profiles from the towing tests on the AD70 are presented in figure 45 with least-squares fitted polynomial curves. As explained in chapter 3.2.4, the vertical velocity profiles could not be assumed symmetric around the disc axis. Thus, the measurements could not be mirrored around z/D=0, and the vertical velocity deficit profiles could not be effectively represented by Gaussian curves.

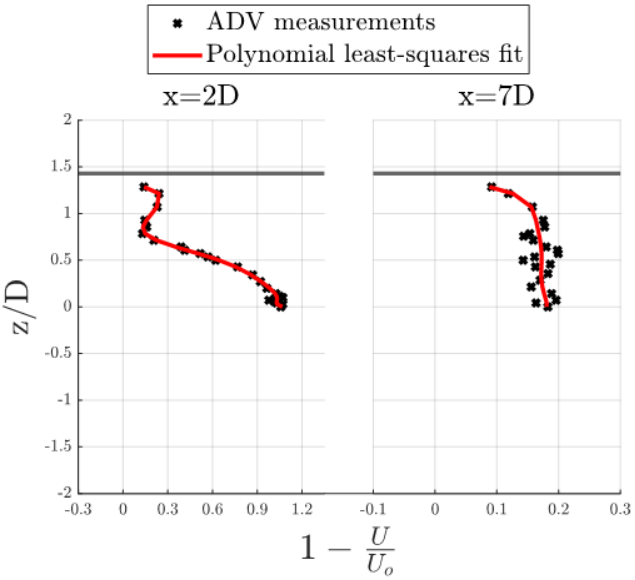

Figure 45: Vertical velocity deficit profiles for the AD70. The grey horizontal lines at z/D=1.43 marks the free water surface. The 2D and 7D measurement points are least-squares fitted with a 12-term polynomial curve and 6-term polynomial curve, respectively.

The vertical velocity deficit profiles from figure 45 show that the half of the wake closest to the free water surface, i.e., where z/D>0, is affected by the tower. This becomes apparent by studying the velocity deficit profile at 2D downstream. When measurements are conducted outside the wake of the disc during vertical velocity profiles, the measurement point is still in the wake of the tower. Therefore, the velocity deficit does not stabilise approximately at 0 when measurements are conducted outside of the wake of the disc. In chapter 5.5.1, when comparing the vertical and transverse velocity deficit profiles of the AD70, the impact from the tower on the velocity deficit profiles will be more apparent.

As shown in figure 45, the upper half of the wake at 7D was not quantified sufficiently, i.e., all the measurement points at 7D were taken within the wake of the disc. The explanation for this was the limited distance to the free water surface. Measurements were taken up to a minimum water depth of 10 cm, i.e., z/D=1.29. If, for instance, the wake was to be quantified to 1.5D from the disc centre point, the ADV would have to measure at 5 cm above the water surface.

The maximum relative velocity deficit, $\Delta U_{max}/U_0$, from the vertical velocity deficit profiles of the AD70 at 2D and 7D downstream were 1.072 and 0.199, respectively. As such, reversed flow was observed in the near wake at 2D.

Turbulence kinetic energy

In figure 46 the vertical non-dimensional TKE profiles for the AD70 are presented with makima interpolation curves fitted to the data points.

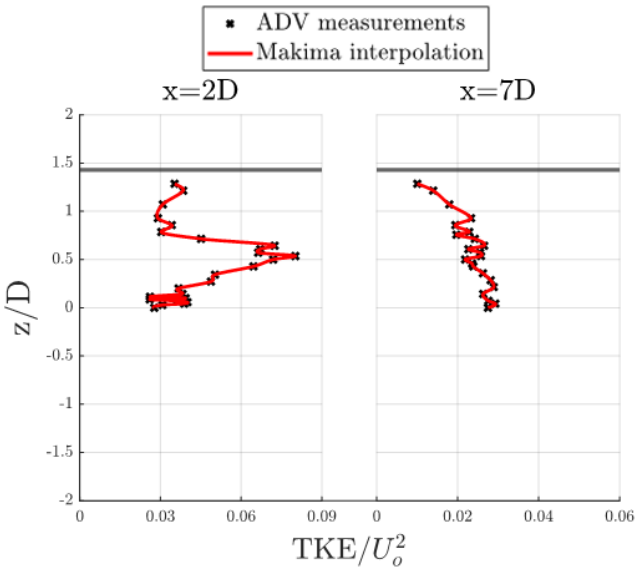

Figure 46: Vertical non-dimensional turbulence kinetic energy (TKE/U_0^2) profiles for the AD70. The grey horizontal lines at z/D=1.43 marks the free water surface.

At 2D downstream, peak TKE is observed behind the disc edge, i.e., at z/D=0.5. Thus, if the TKE profile had been mirrored around z/D=0, the TKE curve would have the characteristic M-shaped turbulence curve. The impact of the tower on the wake can be observed in the TKE profile at 2D in the regions closest to the free water surface, which is marked with grey horizontal lines in figure 46. Despite measurements being conducted outside the wake of the disc, the measurement points were still within the wake of the tower, meaning that the turbulence in the tower wake was measured. The impact of the tower on the TKE profiles will be more apparent when the vertical and transverse TKE profiles of the AD70 are compared in chapter 5.5.1.

4.4.2 D-2: Actuator disc 20 cm diameter

Velocity deficit

Figure 47 presents the vertical velocity deficit profiles for the AD20 with 12-term least-squares fitted polynomial curves. Notably, measurements are not mirrored around z/D=0, as the vertical velocity profiles are not assumed to be symmetric around the disc axis. Accordingly, Gaussian curves will not effectively represent these profiles.

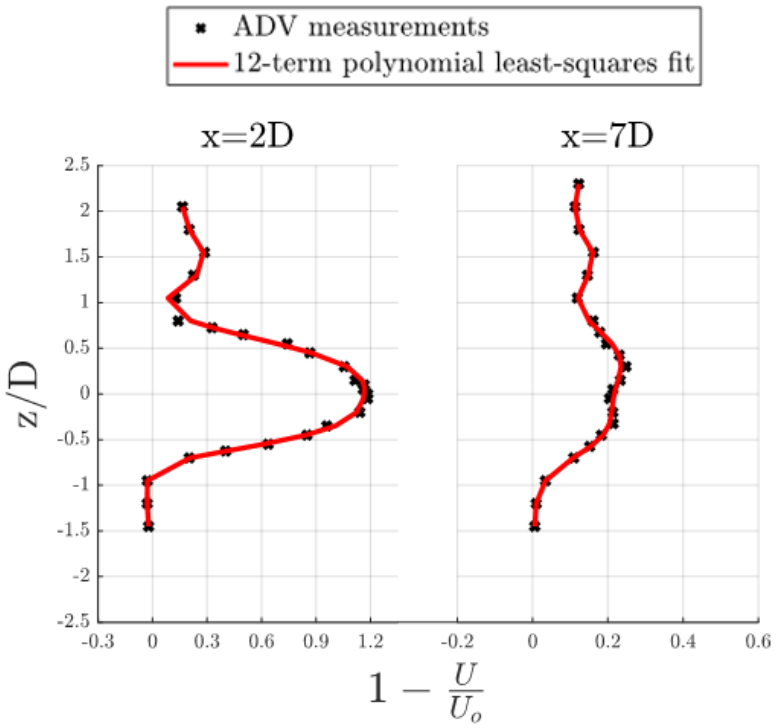

Figure 47: Vertical velocity deficit profiles for the AD20.

By studying the vertical velocity deficit profiles both at 2D and 7D downstream, the profiles are clearly shown not to be symmetric around z/D=0. The lower half of the wake, i.e., z/D<0, is not affected by the tower, and thus the velocity deficit both at 2D and 7D stabilises around 0 for the measurement points located at a sufficient depth to be outside the wake of the disc.

The upper half of the wake, i.e., the half closest to the water surface where z/D>0, is shown in figure 47 to be affected by the tower at both downstream distances. This is easily observed as a significant velocity deficit occurs both at 2D and 7D even when measurements are conducted outside the disc wake, owing to the tower wake. As such, the half of the wake which is unaffected by the tower is more likely to resemble the transverse velocity deficit profiles of the disc. This will be investigated in chapter 5.5.2.

The maximum relative velocity deficit, $\Delta U_{max}/U_0$, from the vertical velocity deficit profiles of the AD20 at 2D and 7D downstream were 1.185 and 0.248, respectively. Thus, reversed flow occurred in the near wake at 2D.

Turbulence kinetic energy

The vertical non-dimensional TKE profiles for the AD20 are shown in figure 48 with makima interpolation curves fitted to the measurement points.

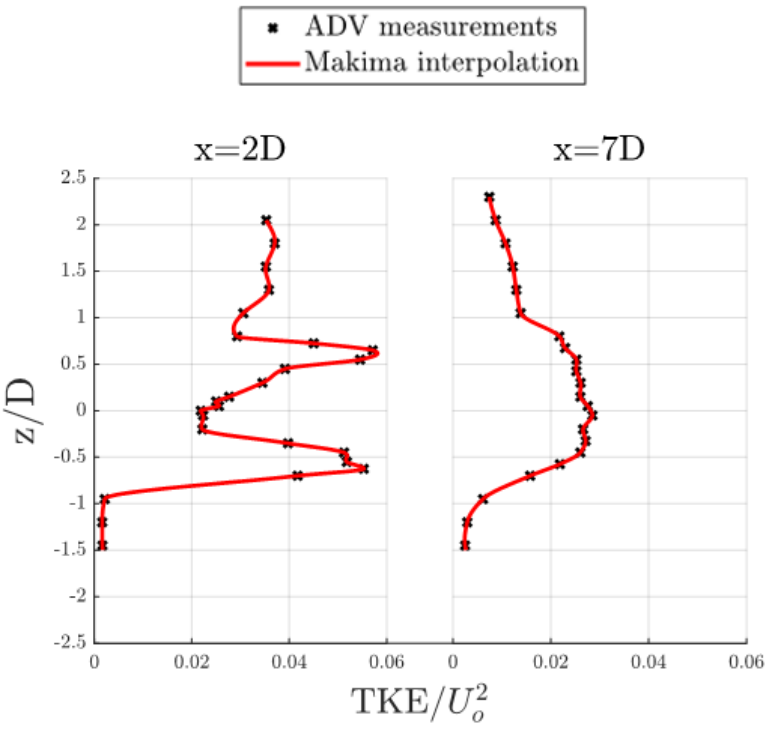

Figure 48: Vertical non-dimensional turbulence kinetic energy (TKE/U_0^2) profiles for the AD20.

At 2D downstream, the TKE is shown to peak behind the edges of the disc, i.e., at z/D=±0.5, thus forming the characteristic M-shaped turbulence curve. At 7D, however, the TKE profile is no longer M-shaped as turbulent mixing has broken down the edge vortices.

Due to the presence of a tower in the upper half of the wake (closest to the water surface), i.e., where z/D>0, the vertical TKE profiles are clearly shown not to be symmetric around the disc axis (z/D=0). This is easily observed in figure 48 for the measurement points located at a sufficient vertical distance from the disc axis to be outside the wake of the disc. In the upper half of the wake (z/D>0), these measurement points are still within the wake of the tower and therefore have a significantly higher level of turbulence compared to the lower half of the wake (z/D<0) where no tower is present. The impact of the tower on the TKE profiles will be further investigated in chapter 5.5.1 when comparing the vertical and transverse TKE profiles of the AD20.

5 Discussion

This chapter will discuss the experimental results of this thesis by comparing the results from the AD70 and AD20. Furthermore, the results will be considered in relation to theory presented in chapter 2, as well as existing experimental and numerical turbine and actuator disc investigations.

5.1 Measurement (A) - Axial force measurements

The results from the axial force measurements on the AD70 and the AD20 are presented in table 12 for comparison.

Table 12: Axial force measurements on the AD70 and AD20.

Tow velocity, U [m/s]	Re_{AD70}	Re_{AD20}	$C_{T_{AD70}}$	$C_{T_{AD20}}$
0.1	$6.312 \cdot 10^4$	$1.803 \cdot 10^4$	0.87	0.87
0.2	$1.262 \cdot 10^5$	$3.607 \cdot 10^4$	0.95	0.86
0.3	$1.894 \cdot 10^5$	$5.410 \cdot 10^4$	0.91	0.85
0.4	$2.525 \cdot 10^5$	$7.214 \cdot 10^4$	0.87	0.84
0.5	$3.156 \cdot 10^5$	$9.017 \cdot 10^4$	0.93	0.84
0.6	$3.787 \cdot 10^5$	$1.082 \cdot 10^5$	0.91	0.84

For all experiments regarded in this thesis, the Reynolds number should, in theory, be sufficiently high for the thrust coefficients of the discs to be independent of the Reynolds number. As explained in chapter 2.2.2, Reynolds independence for drag coefficients is achieved approximately when Re>1000. The C_T values of the AD70 were shown to be independent of Reynolds number for all the experiments of this thesis, with $Re=6.312 \cdot 10^4$ as the minimum Reynolds number for the tests. For the AD20, however, Reynolds independence was only achieved for towing velocities $U \geq 0.4$ m/s, i.e., $Re \geq 7.214 \cdot 10^4$.

The uncertainty associated with the axial force measurements on the AD70 was, as described in chapter 3.4.1, larger compared to the measurements on the AD20. This was reflected in the results, as the C_T values varied significantly more for the AD70 than the AD20. As shown in

table 12, C_T values for the AD70 and the AD20 were calculated to be 0.87-0.95 and 0.84-0.87, respectively, from the axial force measurements conducted in this thesis. The best estimates for the thrust coefficients of the AD70 and AD20 based on these measurements were 0.91 and 0.84, respectively. This was explained in chapter 4.1. Although the C_T for the AD70 varied through the experiments, there is a clear indication that the thrust coefficient is higher for the AD70 than the AD20. This could be caused by blockage from a confined channel, as described in chapter 2.4.

Equation (2.28) shows that C_T increases with increasing blockage ratio. The blockage ratios of the AD70 and AD20 are B_{AD70} = 5.8% and B_{AD20} = 0.5%, respectively. Applying the additional thrust term due to the influence of channel boundaries, from equation (2.28), yields the theoretical increase of C_T when increasing the blockage ratio from 0.5% to 5.8%:

$$\frac{(1+B)}{(1-B)^2} = \frac{(1+(B_{AD70}-B_{AD20}))}{(1-(B_{AD70}-B_{AD20}))^2} = 1.176 \tag{5.1}$$

Thus, the thrust coefficient is expected to be 17.6% higher for the AD70 compared to the AD20 based on theory. The experiments of this thesis, however, resulted in an 8.33% higher C_T for the AD70 compared to the AD20.

Notably, the thrust coefficients of the two actuator discs were measured using two different methods. Axial force measurements on the AD70 were performed at the base of the tower, whereas the forces of the AD20 were measured directly behind the disc. Although tower drag was subtracted from the measurements on the AD70 rig, this method is not ideal. The measured tower drag from the experiments without the disc mounted on the nacelle will, in theory, be slightly overestimated as the tower would be partly within the wake of the disc during towing runs with the disc mounted on the nacelle. The velocity deficit in the wake of the disc reduces the axial force on the tower. Thus, the thrust coefficient of the AD70 could be slightly higher than the calculated value from the measurements of this thesis.

Huang et al. [50] conducted experiments in a wind tunnel on a circular porous plate with uniformly distributed square holes and a porosity of 44%, and found a thrust coefficient of 0.92. Huang et al. also compared their results with several thrust coefficient measurements conducted by other authors on actuator discs of various porosities and showed that the thrust coefficients decrease with increasing disc porosity, i.e., decreasing disc solidity. Both discs regarded in this thesis have solidities of 57%, thus a porosity of (100−57) %=43%. The wind tunnel experiments performed by Helvig et al. [12], as described in chapter 2.2.1, resulted in a thrust coefficient of

approximately 1.10 for the 60% solidity (40% porosity) trapezoidal holed disc. Hansen et al. [18] experimentally investigated a disc identical to the AD20 in the MarinLab towing tank and found a thrust coefficient of 0.88. The thrust coefficients of the AD70 and AD20 obtained through the measurements of this thesis, i.e., 0.91 and 0.84, respectively, are therefore of reasonable magnitude in relation to experimental investigations performed by other authors.

5.2 Measurement (B) - Axial velocity profiles

Velocity deficit

The axial velocity deficit profiles of the AD70 and AD20 are presented in figure 49, with 7-term polynomial least-squares fitted curves.

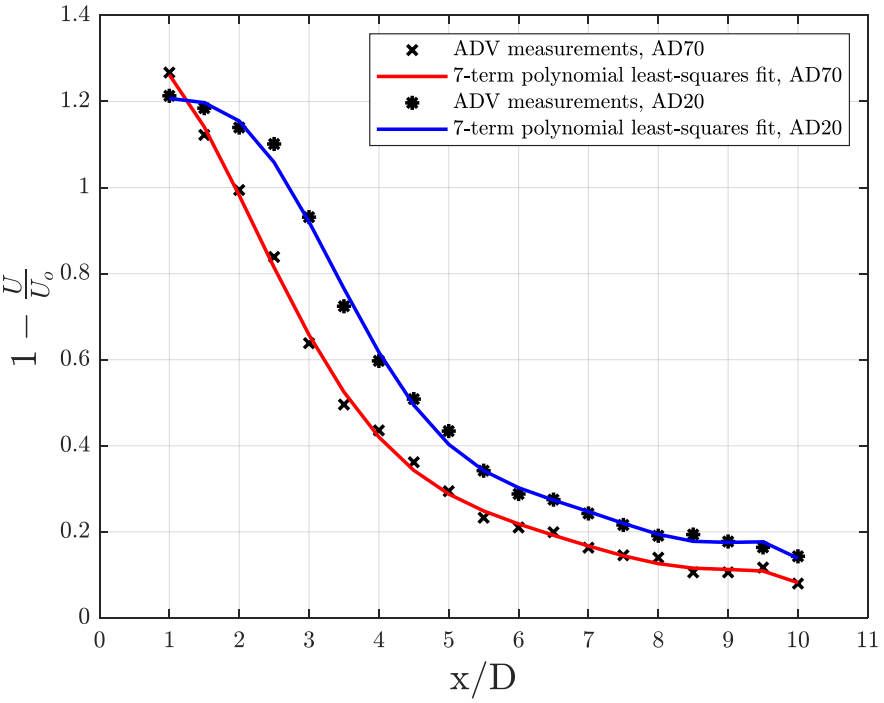

Figure 49: Axial velocity deficit profiles for the AD70 and AD20.

The axial velocity deficit in the wake of the two discs is shown in figure 49 to have similar development with downstream distance, except in the near wake from 1D to 2D. In this region of the wake, the geometry of the disc setups greatly influences the wake. Thus, the differences between the two disc setups, primarily the nacelle for the AD70, causes discrepancies between the wakes from 1D to 2D.

Both discs are shown to have recirculation regions in the near wake, a phenomenon that does not occur in the wake of a turbine. The observed recirculation regions in the wake of the two discs also differ from experiments conducted by Helvig et al. [12] as presented in chapter 2.2.1. Helvig et al. observed a recirculation region in the wake of the 60% solidity trapezoidal holed disc, however, this region was only present less than 1D downstream of the disc. As shown in figure 49, the AD70 experiences reversed flow at 1D and 1.5D downstream, whereas the recirculation region is observed between 1D and 2.5D downstream of the AD20. Aasnæs [47] conducted experiments in the MarinLab tank, investigating the wake of small wind farm setups consisting of five to seven actuator discs (which are identical to the AD20), and observed reversed flow in the wake of the front row discs at 2D downstream. As such, the measurements performed by Aasnæs agree with the results of this thesis.

The results from figure 49 show that the velocity deficit for the AD70 is larger compared to the AD20 at the disc centreline (y/D=0) at 1D downstream. A reasonable explanation for this is the nacelle of the AD70. The nacelle has a length of 0.525 m (see figure 10). For measurements at 1D, i.e., 0.7 m downstream of the disc, the ADV measurement point is located only 0.175 m downstream of the end point of the nacelle. As such, the nacelle greatly influences this measurement and causes a large velocity deficit. This is reasonable considering the results from the transverse velocity deficit profiles of the nacelle and tower presented in chapter 4.3.1 which show that a significant velocity deficit occurs at 1D downstream.

At downstream distances of 1.5-10D, the velocity deficit is smaller for the AD70 compared to the AD20. This does not correspond with wind turbine studies by Magnusson and Smedman [51] and Vermeer et al. [52], which state that increasing thrust coefficient leads to larger velocity deficit in the wake. Furthermore, an experimental study by Zhang et al. [53] observed an increase in the wake velocity deficit of a turbine associated with increasing blockage ratio. As shown in chapter 5.1, the thrust coefficient of the AD70 was found experimentally to be 8.3% higher than the AD20, owing to the higher blockage ratio of the AD70. As such, the wake velocity deficit is expected to be higher for the AD70 than the AD20 based solely on the thrust coefficients. However, a reasonable explanation for observing a smaller velocity deficit in the wake of the AD70 compared to the AD20 can be found by comparing the TKE profiles of the two discs.

Turbulence kinetic energy

In figure 50, the axial non-dimensional TKE profiles for the AD70 and AD20 are shown with makima interpolation curves fitted to the data points.

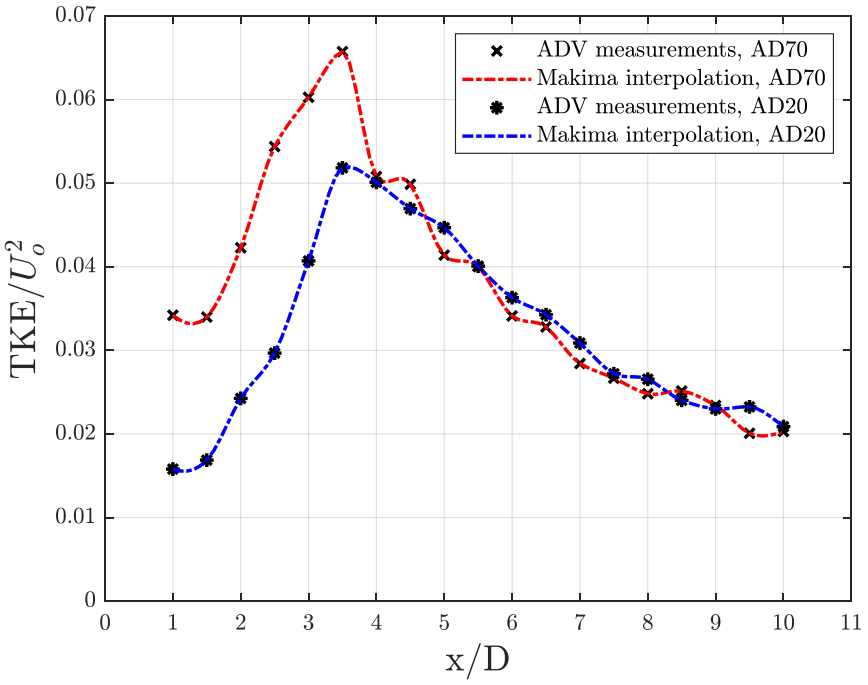

Figure 50: Axial non-dimensional turbulence kinetic energy (TKE/U_0^2) profiles for the AD70 and AD20.

Figure 50 shows that the axial TKE profiles generally have similar shapes for the two actuator discs. Both profiles show that the TKE increases from 1D and peaks at 3.5D downstream of the discs. From 3.5-10D, the TKE decreases for both discs, a development that is expected to continue if measurements were taken further downstream of the discs.

The TKE of the AD70 is significantly higher compared to the AD20 in the near wake of the discs along the centreline, from 1-3.5D downstream. In this region of the wake, the TKE of the AD70 was found to be 26.8-116.6% higher than the AD20. From downstream distances of 4-10D, however, the TKE of the AD70 and the AD20 are nearly identical. These observations can be associated with additional turbulence induced by the nacelle of the AD70. The transverse TKE profiles for the nacelle and tower of the AD70 presented in chapter 4.3.1 show that a significant level of turbulence occurred at 1D and 2D downstream, whereas at 4D, the induced turbulence was less apparent.

As explained in chapter 2.3.1, turbulent mixing plays a key role in wake recovery. It has been shown through several laboratory scale turbine investigations, such as studies by Talavera and

Shu [54] and Medici and Alfredsson [55], that higher turbulence levels in the incoming flow of a turbine causes higher turbulence in the wake and therefore a faster wake recovery.

All experiments of this thesis are conducted under laminar inflow conditions. Mechanical turbulence induced by the nacelle causes significantly higher turbulence in the near wake of the AD70 compared to the AD20. This increased turbulence means increased turbulent mixing, hence a faster wake recovery for the AD70 compared to the AD20, which is reflected by the axial velocity deficit profiles presented in figure 49. The additional turbulence induced by the nacelle is shown in figure 50 to decay relatively fast, which agrees with theory presented in chapter 2.3.1.

A study by Wang et al. [56] investigated the impact of the tower and nacelle on turbine wakes through large eddy simulations (LES) and model experiments in a wind tunnel, and found that the tower and nacelle generate substantial amounts of turbulence in the near wake, and thus enhance turbulent mixing in the wake. Wang et al. do, however, suggest that tower and nacelle effects observed in their study might be more pronounced for the model turbine compared to a full scale turbine as the tower and nacelle were relatively larger for the model compared to full scale. This should also be considered for the results of this thesis, with the nacelle of the AD70 being relatively larger compared to that of a full scale device, as stated in chapter 3.1.3. Another numerical study conducted by Yang & Sotiropoulos [57] showed that the nacelle of a turbine significantly increases TKE in the near wake.

5.3 Measurement (C) - Transverse velocity profiles

Velocity deficit

The transverse velocity deficit profiles from the towing tests on the AD70 and AD20 are presented in figure 51. As explained in chapter 4.3, the transverse velocity deficit profiles of both actuator discs are effectively represented by Gaussian curves at downstream distances from 4-10D. At 2D, however, the Gaussian curves are not representative of the velocity deficit profiles, and the measurements are more accurately described by 12-term polynomial least-squares fitted curves. Therefore, when comparing the transverse velocity deficit profiles of the two discs in figure 51, the measurements at 2D are shown as 12-term polynomial least-squares fitted curves, whereas the measurements from 4-10D are presented as best-fit Gaussian curves.

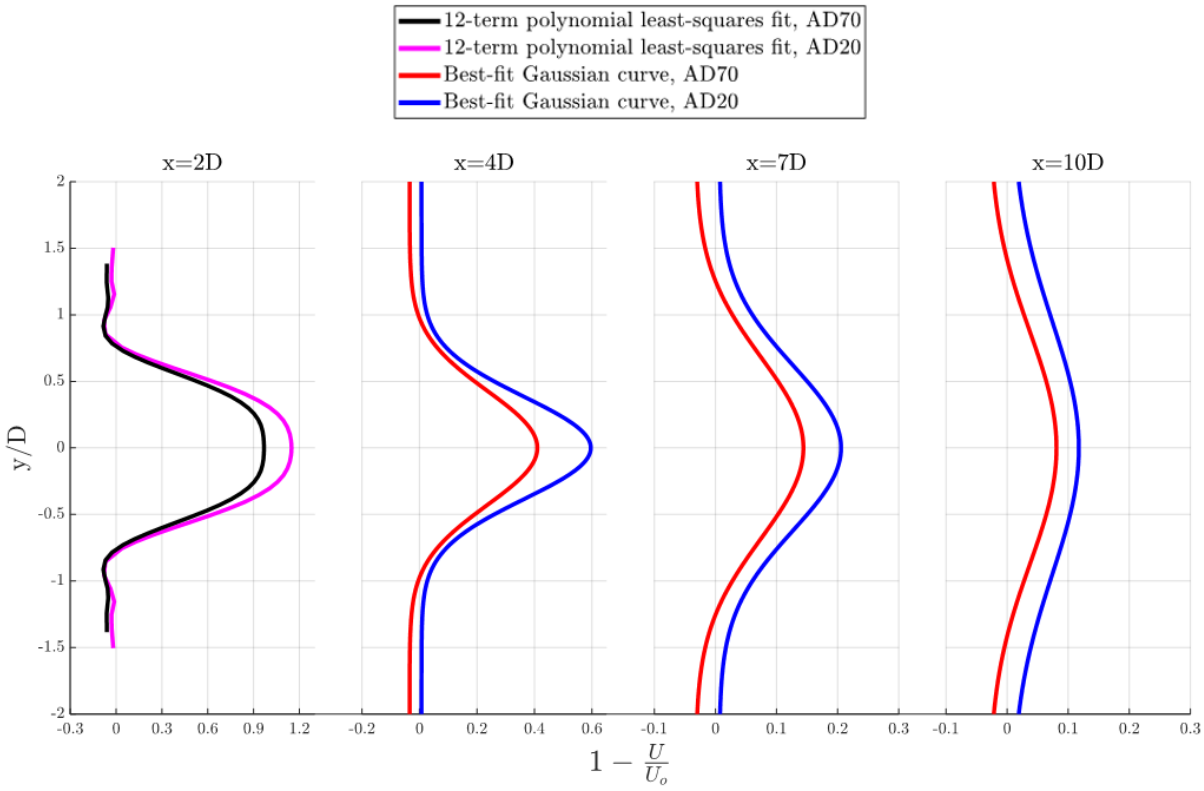

Figure 51: Transverse velocity deficit profiles for the AD70 and AD20.

The transverse velocity deficit profiles show that the velocity deficit in the wake of the AD20 is larger compared to the AD70 for all the downstream distances compared in figure 51, i.e., 2D, 4D, 7D and 10D. These results agree with the axial velocity deficit profiles presented in figure 49. The explanation can be found in the transverse non-dimensional TKE profiles of the two discs, which show a significantly higher level of turbulence in the near wake of the AD70 compared to the AD20. Reversed flow is observed for both discs at 2D downstream.

The maximum relative velocity deficit, $\Delta U_{max}/U_0$, and bypass velocity, $U_{b,max}/U_0$, from the transverse velocity deficit profiles of the AD70 and AD20 are presented in table 13. Values from table 13 represent the ADV measurement points and will be used in further comparisons of the two discs.

Table 13: Maximum relative velocity deficit, $\Delta U_{max}/U0$, and bypass velocity, $U_{b,max}/U_0$, from the transverse velocity deficit profiles of the AD70 and AD20. Values represent the ADV measurement points. In the table, N/A=not available.

Downstream distance	**AD70**		**AD20**	
	$\frac{\Delta U_{max}}{U_0}$	$\frac{U_{b,max}}{U_0}$	$\frac{\Delta U_{max}}{U_0}$	$\frac{U_{b,max}}{U_0}$
1D	1.289	1.132	N/A	N/A
2D	1.040	1.072	1.202	1.048
4D	0.462	1.037	0.607	0.993
6D	0.246	1.032	N/A	N/A
7D	0.162	1.035	0.213	0.994
10D	0.097	1.039	0.125	0.993

Increased flow velocity around the disc can be observed both for the AD70 and AD20 at 2D, with increases in velocities of 7.2% and 4.8%, respectively, relative to the free stream velocity, U_0. In the far wake, from 4-10D, increased bypass velocity is only observed for the AD70, with increases varying from 3.2-3.9%. For the AD20, the bypass velocity was in fact measured as 0.6-0.7% lower than the defined free stream velocity of 0.4 m/s. Possible explanations for this was discussed in chapter 4.3.2. However, these results show that the higher blockage ratio of the AD70 (5.8%) compared to the AD20 (0.5%) causes a larger increase in the bypass velocity for the AD70, thus reflecting blockage theory presented in chapter 2.4.

The blockage theory from chapter 2.4 also states that blockage could limit wake expansion. The relative half-wake width, $y_{1/2}/R$, from the transverse velocity deficit profiles in the far wake of the two discs is plotted as a function of downstream distance in figure 52. The half-wake widths were found from the best-fit Gaussian curves, and the disc radius is denoted by R. The far wake of both discs is considered to start at 4D downstream.

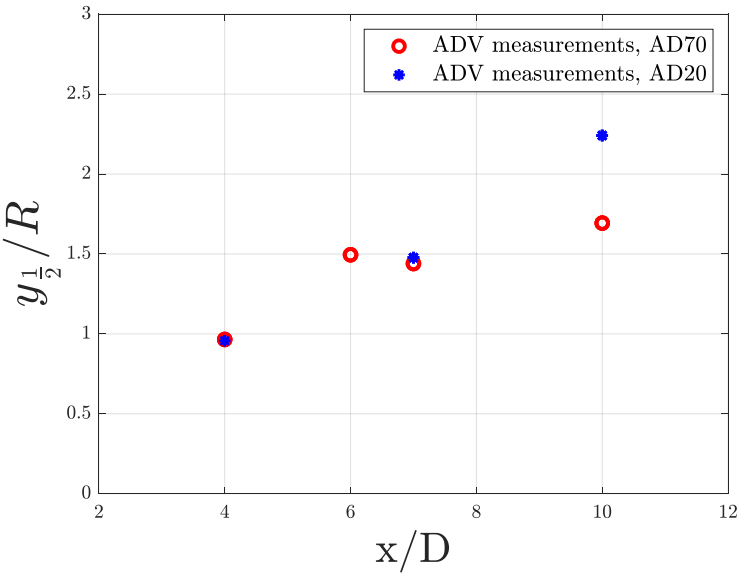

Figure 52: Half-wake width from the transverse velocity deficit profiles for the AD70 and AD20 as a function of downstream distance.

By studying figure 52, the half-wake widths of the two discs are in good agreement at 4D and 7D. This indicates that the higher blockage ratio if the AD70 compared to the AD20 has no significant impact on wake expansion when x≤7D. However, at 10D downstream, the half-wake width of the AD20 is shown to be 32.4% larger compared to the AD70. The reason for this is that the wake expansion of the AD70 is constrained by the side walls of the MarinLab tank, which are located at y/D=±2.14 for the AD70. As such, the results demonstrate blockage effects due to a confined channel, as described in chapter 2.4. The results from figure 52 can be studied in detail in table 14.

Table 14: Maximum relative half-wake width, $y_{1/2}/R$, from the transverse velocity deficit profiles of the AD70 and AD20. Values are found from the best-fit Gaussian curves. In the table, N/A=not available.

Downstream distance	**AD70** $\frac{y_{1/2}}{R}$	**AD20** $\frac{y_{1/2}}{R}$
4D	0.965	0.957
6D	1.495	N/A
7D	1.440	1.477
10D	1.693	2.241

As explained in chapter 2.3.2, the velocity deficit, ΔU, in the far wake of a turbine follows a self-similar Gaussian curve. The transverse velocity deficit profiles in the far wake of the AD20 and AD70 were compared with a self-similar Gaussian profile to determine if the velocity distributions were representative of a turbine wake. The self-similar Gaussian profiles shown in figures 53 and 54 were fitted to the measurement points from 4D downstream of the AD20 and AD70, respectively. For the AD20, the far wake has self-similar behaviour, as shown in figure 53.

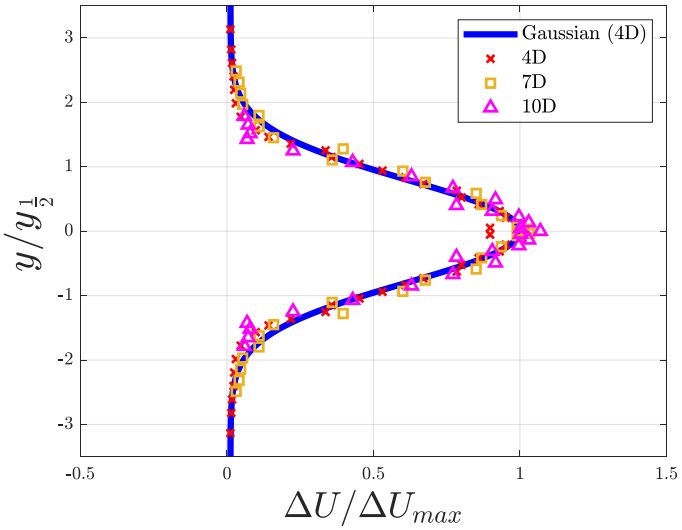

Figure 53: Transverse profile of normalised velocity for the AD20 at x=4D, 7D and 10D with self-similar Gaussian profile. The Gaussian profile is fitted to the measurement points at x=4D.

The far wake of the AD70 did not show the same degree of self-similarity as the AD20. This is clearly demonstrated in figure 54.

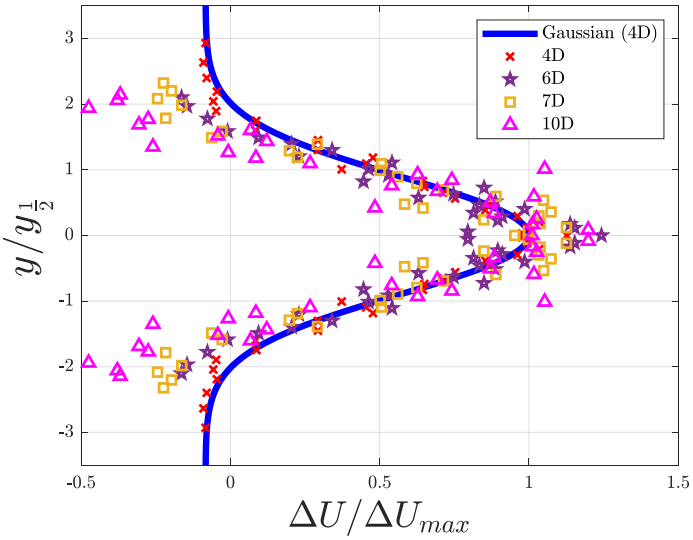

Figure 54: Transverse profile of normalised velocity for the AD70 at x=4D, 6D, 7D and 10D with self-similar Gaussian profile. The Gaussian profile is fitted to the measurement points at x=4D.

By studying figure 54, the wake of the AD70 is not self-similar in the regions closest to the tank side walls. The lowest degree of self-similarity is observed at 10D, where the wake is, as shown by the half-width profiles from figure 52, constrained by bounding surfaces. Accordingly, the results of this thesis show that velocity deficit in the far wake of porous actuator discs follows a self-similar Gaussian curve if the disc wake is unconstrained by bounding surfaces.

Turbulence kinetic energy

Figure 55 shows the transverse non-dimensional TKE profiles for the AD70 and AD20 with makima interpolation curves fitted to the data points.

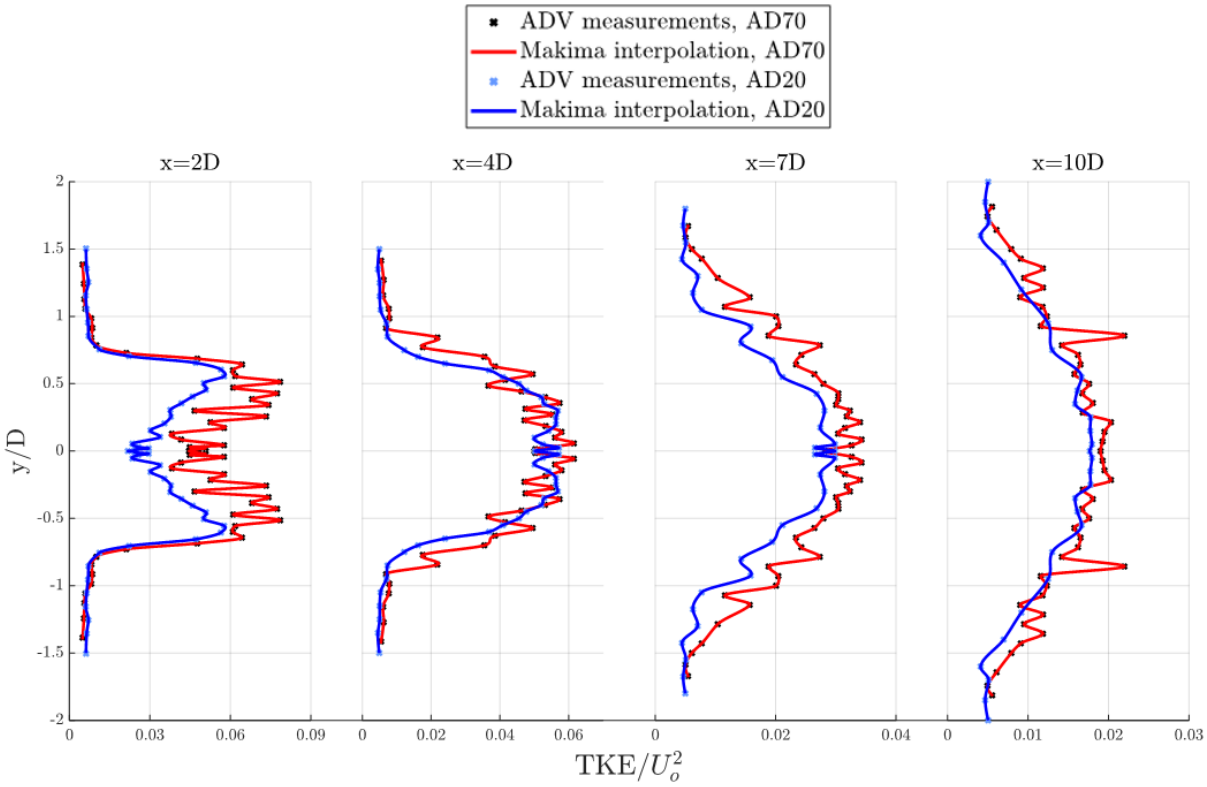

Figure 55: Transverse non-dimensional turbulence kinetic energy (TKE/U_0^2) profiles for the AD70 and AD20.

Figure 55 shows that the TKE in the wake of the AD70 is significantly higher at 2D downstream compared to the AD20. At 2D, the maximum TKE of the AD70 was found to be 36.3% higher than the peak TKE value of the AD20. At distances further downstream of the discs, the difference in TKE is less apparent. Generally, the TKE in the far wake of the AD70, from 4-10D, is shown to be slightly higher than the AD20.

A higher turbulence level in the near wake of the AD70 compared to the AD20 is expected near the disc centreline (y/D=0) due to the nacelle. However, the transverse TKE profiles from figure 55 show that a higher turbulence level occurs over large parts of the wake of the AD70. A possible explanation is found in the transverse TKE profiles of the nacelle and tower of the AD70, presented in chapter 4.3.1, which indicate that the nacelle and tower also induce turbulence in areas with no velocity deficit, i.e., areas believed to be outside the wake of the nacelle and tower. As explained in chapter 4.3.1, the areas of increased turbulence in the tower and nacelle wake were not sufficiently quantified. The transverse position (y/D), where the induced turbulence from the nacelle and tower is no longer significant to the AD70 wake, could therefore not be determined.

Notably, in figure 55, the TKE values appear to fluctuate more significantly in the wake of the AD70 compared to the AD20. The reasons for this observation are somewhat unclear, but it could be associated with varying signal quality from the ADV or the size of the ADV measurement volume relative to the size of the fluid motions occurring in the disc wakes (larger fluid motions for the AD70 owing to its larger dimensions).

Another interesting observation from figure 55 is that the TKE profile of the AD20 preserves its M-shape to a distance further downstream compared to the AD70. This becomes apparent by studying the TKE profiles of the two discs at 4D downstream. At 4D, the M-shape of the TKE profile can still be detected for the AD20, whereas the TKE profile of the AD70 has completely lost its characteristic near wake shape. An M-shaped TKE profile is, as explained in chapter 4.3.1, characteristic of the near wake of turbines and actuator discs due to vortices created at the blade tips and disc edges, respectively. Turbulent mixing causes these vortices to break down at a certain downstream distance, and so the TKE curve ceases to be M-shaped. The significantly higher level of turbulence in the near wake of the AD70 compared to the AD20 causes the edge vortices to break down at a shorter downstream distance. This indicates a faster wake recovery for the AD70 compared to the AD20.

5.4 Measurement (D) - Vertical velocity profiles

Factors such as the ADV cable length and interaction from the free water surface, as discussed in chapter 3.1.3, mean that the comparison of vertical velocity profiles for the two actuator discs could not be done to the same extent as for the transverse velocity profiles. However, the vertical profiles provide interesting observations which will be discussed in the present chapter, as well as in chapter 5.5.

Velocity deficit

In figure 56, the vertical velocity deficit profiles from the towing experiments on the AD70 and AD20 are presented with polynomial least-squares fitted curves.

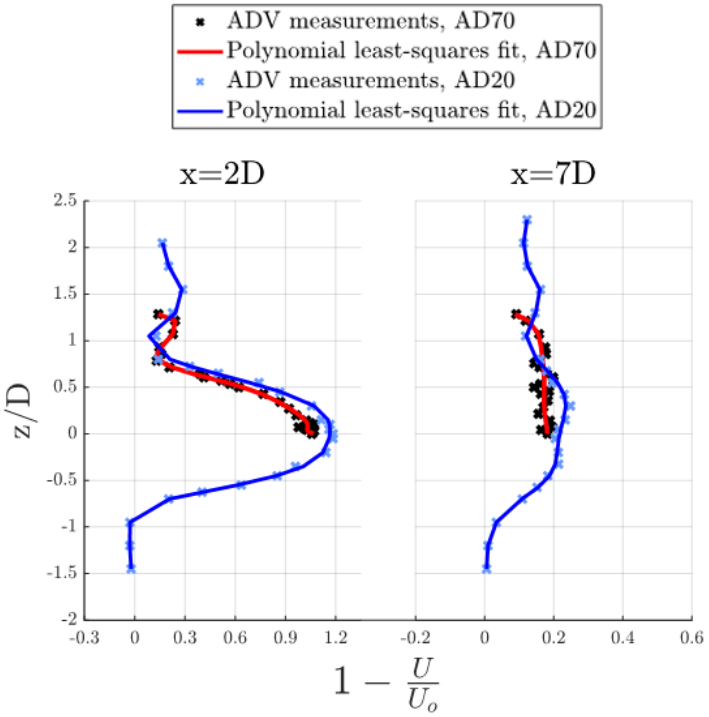

Figure 56: Vertical velocity deficit profiles for the AD70 and AD20. All measurement points are least-squares fitted with a 12-term polynomial curve, except the profile of the AD70 at 7D which is fitted with a 6-term polynomial curve.

The impact of the tower on the vertical velocity deficit profiles of the two discs is clearly shown in figure 56. The tower is only present in the upper half of the wake, i.e., the half closest to the free water surface where z/D>0. Due to the tower wake, significant velocity deficits occur in the wake of both discs despite measurements being conducted at a far vertical distance from the disc centreline.

It is difficult to compare the two discs at 7D downstream considering that the wake of the AD70 could not be quantified sufficiently. However, at 2D downstream, similarities can be found between the velocity distributions in the wake of the two discs. Reversed flow was observed in the wake of both discs at 2D. As for the axial and transverse velocity deficit profiles, the AD70 generally has a smaller velocity deficit at 2D and 7D downstream compared to the AD20, owing to the higher level of turbulence in the near wake of the AD70, which can be observed from the vertical TKE profiles in figure 57.

For some of the measurement points of the AD70 located at a far vertical distance from the disc axis (z/D=0), larger velocity deficits are observed compared to the AD20. This does not correspond with the transverse velocity deficit profiles shown in figure 51. Interaction between the wake of the AD70 and the free water surface is a probable explanation for these results. The centre point of the AD70 and AD20 are located at distances of 1.43D and 3.5D, respectively, from the free water surface. As such, the wake of the AD70 is more susceptible to surface effects.

Turbulence kinetic energy

The vertical non-dimensional TKE profiles for the AD70 and AD20 are presented in figure 57 with makima interpolation curves fitted to the measurement points.

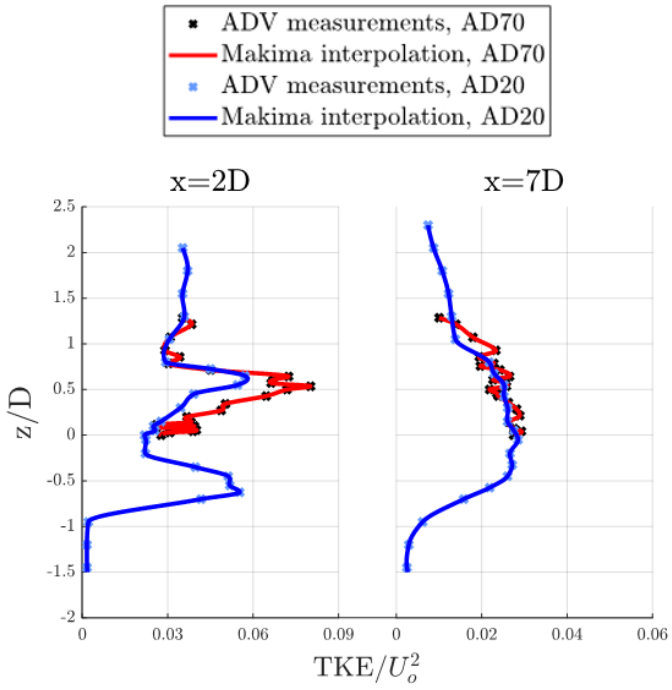

Figure 57: Vertical non-dimensional turbulence kinetic energy (TKE/U_0^2) profiles for the AD70 and AD20.

As shown in figure 57, the two actuator discs have similar turbulence distributions both at 2D and 7D downstream. The TKE in the wake of both discs are shown to peak behind the disc edges at 2D due to edge vortices. These vortices have broken down for both discs at 7D due to turbulent mixing. At 2D, the TKE in the wake of the AD70 is significantly higher compared to the AD20, whereas at 7D, the TKE of the two discs are approximately of similar magnitude. These results agree both with the axial and transverse velocity profiles.

Measurement points located at a far vertical distance from the disc centrelines are shown to have relatively high levels of turbulence in the upper half of the wake, i.e., where z/D>0, for both discs. These measurement points are within the tower wake despite being outside the wake of the disc, and so the turbulence level is of significant magnitude.

5.5 Comparing transverse and vertical velocity profiles

Quantifying the wakes both in terms of transverse and vertical velocity profiles provides a more accurate representation of the fluid flow downstream of the discs. In this chapter, the transverse and vertical velocity profiles are compared both for the AD70 and AD20.

5.5.1 Actuator disc 70 cm diameter

Velocity deficit

Figure 58 shows the transverse and vertical velocity deficit profiles from the towing tests on the AD70 with polynomial least-squares fitted curves.

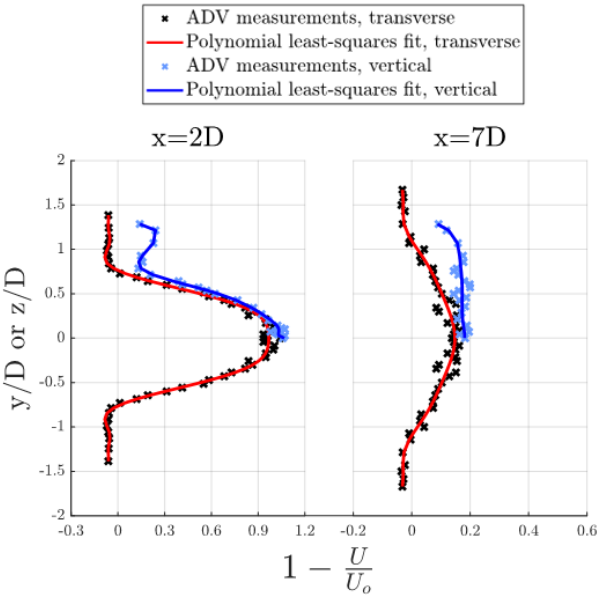

Figure 58: Transverse and vertical velocity deficit profiles for the AD70. All measurement points are least-squares fitted with a 12-term polynomial curve, except the vertical profile at 7D which is fitted with a 6-term polynomial curve.

The transverse and vertical velocity deficit profiles from figure 58 show that the tower affects the vertical profiles, causing dissimilarities between the transverse and vertical profiles. These dissimilarities will be discussed in the following paragraphs.

At 2D, the vertical profile agrees well with the transverse profile for large parts of the wake, approximately when 0<z/D<0.8. A slightly larger velocity deficit is observed for the vertical profile in this region owing to the tower. When z/D>0.8, the velocity deficit of the vertical profile is significantly higher compared to the transverse profile. In this region of the wake, the measurements points are outside the wake of the disc, and so a bypass flow is observed for the transverse profiles, whereas the vertical profiles are still affected by the tower wake.

As previously explained, the vertical profile at 7D could not be fully quantified, and the free water surface is likely to have constrained the wake in the vertical direction. As such, the transverse and vertical velocity deficit profiles at 7D do not agree to the same extent as was shown at 2D. The vertical profile shows a significantly larger velocity deficit compared to the transverse profile, and the velocity distribution for the vertical profile has few similarities with the Gaussian shaped curve of the transverse profile. At the disc axis (y/D=0 or z/D=0), the velocity deficit of the vertical profile was 33.1% larger than that of the transverse profile. These two measurement points should have the exact same position in the wake, and so the velocity deficit should, in theory, be identical. There could be several explanations for this deviation, such as the measurement uncertainty of the ADV (see chapter 3.4.2), uncertainty related to the

cutting of the time series (see chapter 3.5) or possibly a misplacement of the ADV in terms of downstream distance to the disc (se chapter 3.4).

As explained in chapter 2.3.2, both numerical and experimental investigations of turbines have shown that the point of maximum velocity deficit is usually shifted towards the tower [21, 23]. This phenomenon was observed by Pierella and Sætran [58] through experimental turbine investigations in a wind tunnel. The experiments of Pierella and Sætran showed that the presence of the turbine tower wake created a net unbalance in the vertical momentum transport, and that this was the reason for the observed shift in the vertical velocity deficit profiles.

The points of maximum velocity deficit for the vertical profiles of the AD70 at 2D and 7D were found at z/D=0.10 and z/D=0.57, respectively. As such, the point of maximum velocity deficit is shifted more towards the tower in the far wake compared to the near wake. This agrees with results presented by Crespo et al. [59] from both a numerical model (UPM computer code) and experimental results from turbine investigations conducted in the wind tunnel at TNO (the Netherlands Organisation for applied scientific research), which show that the shift of the maximum velocity deficit increases with downstream distance.

Turbulence kinetic energy

In figure 59, the transverse and vertical non-dimensional TKE profiles of the AD70 are shown with makima interpolation curves fitted to the data points.

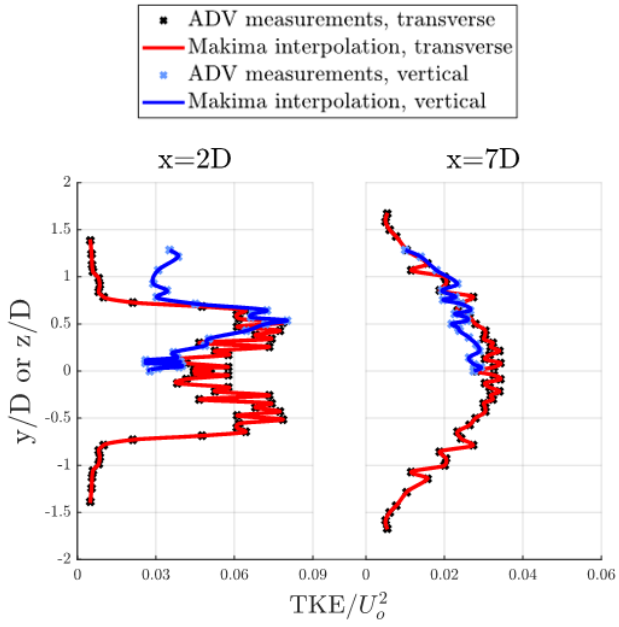

Figure 59: Transverse and vertical non-dimensional turbulence kinetic energy (TKE/U_0^2) profiles for the AD70.

The vertical TKE profiles of the AD70 agree well with the transverse TKE profiles both at 2D and 7D, except for measurement points located at z/D>0.8 or y/D>0.8 at a downstream distance of 2D. These measurement points are outside the wake of the disc. For the vertical profiles, these measurement points are still in the wake of the tower, and so the turbulence level is significantly higher for the vertical profiles compared to the transverse profiles. As explained in chapter 4.4.1, the vertical profile at 7D could not be measured to a sufficient vertical distance from the disc axis for the measurement points to be in a region only affected by the tower wake. Therefore, the tower effect is less apparent for the vertical profile at 7D compared to the profile at 2D.

5.5.2 Actuator disc 20 cm diameter

Velocity deficit

The transverse and vertical velocity deficit profiles from the experiments on the AD20 are presented in figure 60 with 12-term polynomial least-squares fitted curves.

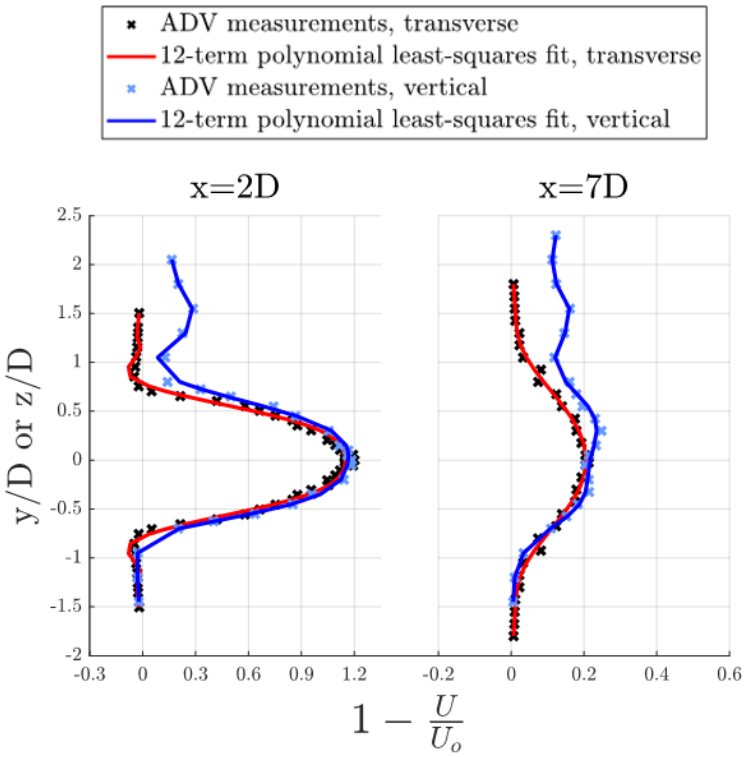

Figure 60: Transverse and vertical velocity deficit profiles for the AD20.

Figure 60 shows agreement between the transverse and vertical velocity deficit profiles both at 2D and 7D where z/D<0 or y/D<0, i.e., the half of the wake without presence of a tower for the

vertical profiles. On the other half of the wake (z/D>0 or y/D>0), the presence of a tower for the vertical profiles causes a larger velocity deficit for these profiles compared to the transverse profiles.

At 2D, the point of maximum velocity deficit for the vertical profile occurred at z/D=0.00. As such, the point of maximum velocity deficit was not shifted towards the tower at this downstream distance. This result deviates from numerical and experimental turbine investigations which usually show a shift towards the tower [21, 23]. A possible explanation for this could be measurement uncertainty, as discussed in chapter 3.4. At 7D, however, a shift of the velocity deficit towards the tower was observed for the vertical profile, with the point of maximum velocity deficit occurring at z/D=0.30.

Turbulence kinetic energy

Figure 61 shows the transverse and vertical non-dimensional TKE profiles for the AD20 with makima interpolation curves fitted to the measurement points.

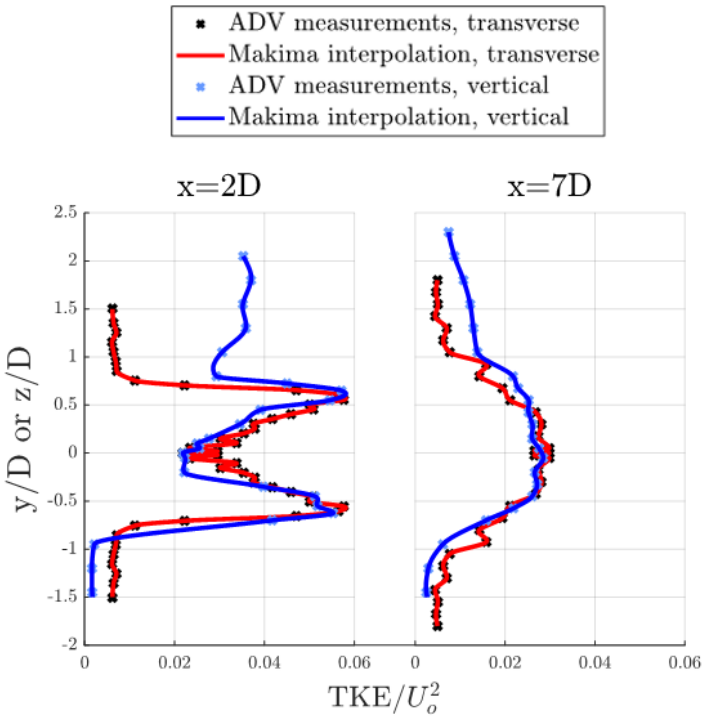

Figure 61: Transverse and vertical non-dimensional turbulence kinetic energy (TKE/U_0^2) profiles for the AD20.

The vertical TKE profiles of the AD20 are shown in figure 61 to agree relatively well with the transverse TKE profiles for large parts of the wake. Clear distinctions between the transverse and vertical profiles are found at both downstream distances in the region where the tower is

the dominant source of turbulence for the vertical profiles. This is the case when measurements are conducted at a sufficient vertical distance from the disc axis for the measurement points to be outside or in the outer parts of the disc wake. At 2D and 7D, this occurs approximately when $z/D>0.8$ and $z/D>1.0$, respectively. Due to the tower wake, the turbulence level of the vertical profiles is significantly higher compared to the transverse profiles in these regions.

In the half of the wake where no tower is present for the vertical profiles ($z/D<0$), the turbulence is shown to stabilise at a lower TKE value for the vertical profiles compared to the transverse profiles for the measurement points located outside the disc wake. As stated in chapter 3.2.4, the centre point of AD20 was located at a water depth of 1.0 m for the transverse profiles, whereas for the vertical profiles, the disc centre point was located at a depth of 0.7 m. This could be an explanation for the difference in turbulence level.

Both numerical and experimental wind turbine investigations have shown that the point of maximum turbulence intensity is usually found above the turbine axis [21, 23]. Relating these observations to the experiments of this thesis, the point of maximum turbulence should be observed in the vertical profiles in the half of the wake where no tower is present ($z/D<0$). This phenomenon was not observed when comparing the transverse and vertical TKE profiles of the AD20. The peak TKE values from these profiles were almost identical. In fact, for the vertical profile at 2D, the peak TKE was found in the tower-affected half of the wake ($z/D>0$). This observation indicates that there are some characteristics of a turbine wake that are not perfectly represented by using an actuator disc.

6 Conclusion

Experimental investigations of two 57% solidity trapezoidal holed actuator discs with diameters of 0.7 m (AD70) and 0.2 m (AD20) have been performed in the MarinLab towing tank at HVL under laminar inflow conditions. The disc setups were different, with the AD70 being mounted on a relatively large nacelle compared to a full scale turbine, whereas the AD20 was mounted without a nacelle. Tower, nacelle and potential blockage effects are investigated by measuring the wake flow and thrust coefficient of these two setups. In addition, the measurements are used to assess how well the wake of actuator discs represent the wake of a turbine.

The axial force measurements indicate that blockage effects should be accounted for when the blockage ratio is 5.8% or above. The thrust coefficients of the AD70 and the AD20 were found to be 0.91 and 0.84, respectively. Thus, the thrust coefficient of the disc was increased by 8.3% when the blockage ratio was increased from 0.5% (AD20) to 5.8% (AD70). The results therefore indicate that the thrust increases with increasing blockage ratio. Thrust coefficients were shown to be independent of Reynolds number when $Re \geq 6.312 \cdot 10^4$.

The higher blockage ratio of the AD70 compared to the AD20 also caused a larger increase in the bypass velocity for the AD70. Recirculation regions were observed in the near wake of both actuator discs, which does not correspond with the wake of a turbine. The transverse velocity deficit profiles show that a Gaussian curve does not represent the velocity deficit profiles successfully at 1D and 2D downstream of the discs. However, from 4-10D, the velocity deficit profiles of both discs were effectively represented by Gaussian curves. Thus, the far wake region was defined from 4D for both discs. The vertical velocity profiles were shown not to be symmetric around the disc axis, as expected due to the presence of a tower. The results of this thesis indicate that the far wake region of a rotating turbine can be effectively represented by using actuator discs.

The experiments showed that the velocity deficit was larger in the wake of the AD70 compared to the AD20 at 1D downstream, most likely due to the nacelle of the AD70. At downstream distances of 1.5-10D, however, the velocity deficit of the AD20 was larger compared to the AD70. A reasonable explanation for this was found in the TKE profiles of the two discs. The TKE profiles showed a significantly higher turbulence level in the near wake of the AD70 compared to the AD20. This was likely caused by the nacelle of the AD70. The results indicate that the significantly higher level of turbulence in the near wake of the AD70 compared to the

AD20 leads to a faster wake recovery for the AD70. In the near wake of the discs, peak TKE values were found behind the disc edges due to vortex shedding from the disc edges. These vortices were shown to break down at a shorter downstream distance for the AD70 compared to the AD20, owing to the higher turbulence level in the wake of the AD70. The faster wake recovery of the AD70 compared to the AD20 was apparent both from the smaller velocity deficit and the faster breakdown of the disc edge vortices in the wake of the AD70.

Blockage effects on wake expansion were demonstrated through the half-wake width development downstream of the discs. The half-wake width of the AD70 and AD20 were similar at downstream distances of 4D and 7D. However, at 10D, a 32.4% larger half-wake width was observed for the AD20 compared to the AD70, as the wake expansion of the AD70 was constrained by the tank side walls.

Self-similar behaviour was shown for both actuator discs, except in the regions closest to the tank side walls for the AD70. The results of this thesis therefore indicate that velocity deficit in the far wake of actuator discs follows a self-similar Gaussian curve if the disc wake is unconstrained by bounding surfaces.

7 Suggestions for Further Work

The results of this thesis have demonstrated several important aspects regarding the wake flow and loadings of turbines, such as tower, nacelle and blockage effects. These effects should also be considered for the 0.7 m diameter hydrokinetic turbine which is under development at HVL. The rig designed for the AD70 was shown to be adequate in terms of functionality and strength requirements and could therefore also be applied for the HVL turbine. After completion of the turbine, it would be interesting to conduct experiments, similar to those presented in this thesis, on the turbine. The results from the turbine tests could then be compared with the results from the experiments on the AD70 to see the extent to which the actuator disc is able to represent the 0.7 m diameter turbine. This information is valuable for future laboratory scale investigations of turbines using actuator discs.

The wake flow of the actuator discs has been investigated through single point measurements from an acoustic Doppler velocimeter (ADV) in this thesis. These measurements could alternatively be conducted using an optical measurement technique called particle image velocimetry (PIV) [60]. PIV enables the velocity field of an entire region within a flow to be measured simultaneously, such that flow structures can be visualised. Accordingly, vortices formed in the disc wakes could be visually observed, and the effects of the nacelle on the near wake flow structure could be investigated in further detail. PIV measurements could be used to confirm the observations of this thesis. Specifically, the significantly higher turbulence level in the near wake of the AD70 compared to the AD20, which appeared to enhance wake recovery, could be further investigated.

Furthermore, the experimental data from this thesis should be used for validation of analytical wake models and numerical modelling tools, such as computational fluid dynamics (CFD) and blade element momentum (BEM). Identifying deviations between model predictions and experimental data could contribute to improving these models such that turbine loads and flows around turbines can be predicted more accurately.

References

[1] "The Paris Agreement." United Nations. https://www.un.org/en/climatechange/paris-agreement (accessed May 10, 2022).

[2] "Global energy co2 status report 2019." IEA. https://www.iea.org/reports/global-energy-co2-status-report-2019 (accessed May 10, 2022).

[3] "Green Energy Choices: The benefits, risks and trade-offs of low-carbon technologies for electricity production," United Nations Environment Programme, 2016.

[4] "Renewables 2019 Global Status Report," REN21, 2019.

[5] E. Konstantinidis and P. Botsaris, "Wind turbines: current status, obstacles, trends and technologies," *IOP Conference Series: Materials Science and Engineering*, vol. 161, 2016.

[6] "Wind energy." International Renewable Energy Agency (IRENA). https://www.irena.org/wind (accessed May 11, 2022).

[7] "Renewables 2021 Global Status Report," REN21, 2021.

[8] "Global Wind Report 2022." Global Wind Energy Council. https://gwec.net/global-wind-report-2022/ (accessed May 11, 2022).

[9] D. R. Lande-Sudall, "Co-located Offshore Wind and Tidal Stream turbines," PhD thesis, The University of Manchester, 2017.

[10] L. G. Salgado, "Experiments in the wind turbine far wake for the evaluation of analytical wake models," MSc thesis, NTNU, 2017.

[11] G. S. Payne, T. Stallard, and R. Martinez, "Design and manufacture of a bed supported tidal turbine model for blade and shaft load measurement in turbulent flow and waves," *Renewable Energy*, vol. 107, pp. 312-326, 2017.

[12] S. Helvig, M. Vinnes, A. Segalini, N. Worth and R. Hearst, "A comparison of lab-scale free rotating wind turbines and actuator disks," *Journal of Wind Engineering and Industrial Aerodynamics*, vol. 209, no. 104485, 2021.

[13] S. McTavish, D. Feszty, and F. Nitzsche, "An experimental and computational assessment of blockage effects on wind turbine wake development," *Wind Energy*, vol. 17, pp. 1515-1529, 2014.

[14] H. Sarlak, T. Nishino, L. A. Martínez-Tossas, C. Meneveau, and J. N. Sørensen, "Assessment of blockage effects on the wake characteristics and power of wind turbines," *Renewable Energy,* vol. 93, pp. 340-352, 2016.

[15] T. Y. Chen and L. R. Liou, "Blockage corrections in wind tunnel tests of small horizontal-axis wind turbines," *Experimental Thermal and Fluid Science,* vol. 35, pp. 565-569, 2011.

[16] J. F. Manwell, J. G. McGowan and A. L. Rogers, *Wind energy explained: theory, design and application*, 2 ed. Chichester: John Wiley & Sons, 2009.

[17] T. Burton, D. Sharpe, N. Jenkins and E. Bossanyi, *Wind Energy Handbook*. Chichester: John Wiley & Sons, 2001.

[18] M. Hansen, C. Leikvoll and M. Vikse, "Multirotor wind turbine - drag," BSc thesis, HVL, 2021.

[19] S. F. Hoerner, *Fluid-dynamic drag*. Bakersfield: Hoerner Fluid Dynamics, 1965.

[20] F. Porté-Agel, M. Bastankhah, and S. Shamsoddin, "Wind-Turbine and Wind-Farm Flows: A Review," *Boundary-Layer Meteorology,* vol. 174, no. 1, pp. 1-59, 2020.

[21] A. Crespo, J. Hernández, S. Frandsen, "Survey of modelling methods for wind turbine wakes and wind farms," *Wind Energy,* vol. 2, pp. 1-24, 1999.

[22] T. Stallard, T. Feng, and P. K. Stansby, "Experimental study of the mean wake of a tidal stream rotor in a shallow turbulent flow," *Journal of Fluids and Structures,* vol. 54, pp. 235-246, 2015.

[23] B. Sanderse, "Aerodynamics of wind turbine wakes Literature review," 2009.

[24] I. Neunaber, M. Hölling, R. J. A. M. Stevens, G. Schepers, and J. Peinke, "Distinct Turbulent Regions in the Wake of a Wind Turbine and Their Inflow-Dependent Locations: The Creation of a Wake Map," *Energies,* vol. 13, no. 20, 2020.

[25] S. B. Pope, *Turbulent flows*. Cambridge Univeristy Press, 2000.

[26] H. Glauert, "Airplane Propellers," in *Aerodynamic Theory: A General Review of Progress Under a Grant of the Guggenheim Fund for the Promotion of Aeronautics*, W. F. Durand Ed. Berlin, Heidelberg: Springer Berlin Heidelberg, 1935, pp. 169-360.

[27] B. F. R. Ewald, "Wind Tunnel Wall Corrections," AGARD AG-336, 1998.

[28] R. F. Mikkelsen and J. N. Sørensen, "Modelling of wind tunnel blockage," in *Global Windpower Conference*, Paris, France, 2002.

[29] C. Garrett and P. Cummins, "The efficiency of a turbine in a tidal channel," *Journal of Fluid Mechanics*, vol. 588, pp. 243-251, 2007.

[30] J. Whelan, J. Graham, and J. Peiro, "A free-surface and blockage correction for tidal turbines," *Journal of Fluid Mechanics*, vol. 624, pp. 281-291, 2009.

[31] J. R. Bjørnsen, "Lab-scale measurements of blockage and wake flow on a setup of three laterally spaced wind turbine rotors," MSc thesis, UiB, 2021.

[32] "General Modelling and Scaling Laws." NTNU. https://pdf4pro.com/view/general-modelling-and-scaling-laws-iv-ntnu-5b3107.html (accessed Apr. 15, 2022).

[33] J. M. J. Journée and W. W. Massie, *Offshore Hydromechanics*, 1 ed. Delft University of Technology, 2001.

[34] M. O. L. Hansen, *Aerodynamics of wind turbines*, 3 ed. London: Routledge, 2015.

[35] J. I. Whelan and T. Stallard, "Arguments for modifying the geometry of a scale model rotor," in *Proceedings of the 9th European Wave and Tidal Energy Conference*, Southampton, UK, 2011.

[36] F. Berger, L. Kröger, D. Onnen, V. Petrović, and M. Kühn, "Scaled wind turbine setup in a turbulent wind tunnel," *Journal of Physics: Conference Series*, 2018.

[37] T. Javaherchi, N. Stelzenmuller, J. Seydel, and A. Aliseda, "Experimental and Numerical Analysis of Scale-Model Horizontal Axis Hydrokinetic Turbine," in *Proceedings of the 2nd Marine Energy Technology Symposium*, Seattle, United States, 2014.

[38] A. Robertson *et al.*, "Summary of Conclusions and Recommendations Drawn From the DeepCwind Scaled Floating Offshore Wind System Test Campaign," in *Proceedings of the ASME 2013 32nd International Conference on Ocean, Offshore and Arctic Engineering*, Nantes, France, 2013.

[39] L. P. Chamorro, R. E. A. Arndt, and F. Sotiropoulos, "Reynolds number dependence of turbulence statistics in the wake of wind turbines," *Wind Energy*, vol. 15, no. 5, pp. 733-742, 2012.

[40] "MarinLab." HVL. https://www.hvl.no/marinlab (accessed Nov. 16, 2021).

[41] R. Kumar, S. Chhabra, A. S. Verma and A. Gupta, "Analysis of load cell," *International Journal of Applied Engineering Research,* vol. 13, no. 6, pp. 274-277, 2018.

[42] "Measuring circuits for strain." OMEGA. https://www.omega.co.uk/literature/transactions/volume3/strain2.html (accessed Mar. 25, 2022).

[43] J. P. Bentley, *Principles of Measurement Systems*, 4 ed. Harlow: Pearson Education Limited, 2005.

[44] "The Comprehensive Manual for Velocimeters." Nortek. https://support.nortekgroup.com/hc/en-us/articles/360029839351-The-Comprehensive-Manual-Velocimeters (accessed Feb. 22, 2022).

[45] "Factors of Safety." The Engineering ToolBox. https://www.engineeringtoolbox.com/factors-safety-fos-d_1624.html (accessed Mar. 30, 2022).

[46] M. Mohammed, A. Messerman, B. Mayhan, and K. Trauth, "Theory and Practice of the Hydrodynamic Redesign of Artificial Hellbender Habitat," *Herpetological Review,* vol. 47, pp. 586-591, 2016.

[47] C. H. Aasnæs, "Experimental investigation of wind farm flow effects," MSc thesis, UiB, 2022.

[48] "makima." MathWorks. https://se.mathworks.com/help/matlab/ref/makima.html#mw_e8ee1c8c-2cc3-46c4-90c4-c3208804ff4e (accessed Mar. 29, 2022).

[49] "Systematic Error." ScienceDirect. https://www.sciencedirect.com/topics/engineering/systematic-error (accessed Apr. 17, 2022).

[50] M. Huang, C. Ferreira, A. Sciacchitano, and F. Scarano, "Wake scaling of actuator discs in different aspect ratios," *Renewable Energy,* vol. 183, pp. 866-876, 2022.

[51] M. Magnusson and A. S. Smedman, "Air flow behind wind turbines," *Journal of Wind Engineering and Industrial Aerodynamics,* vol. 80, no. 1, pp. 169-189, 1999.

[52] N.-J. Vermeer, J. Sørensen, and A. Crespo, "Wind turbine wake aerodynamics," *Progress in Aerospace Sciences - PROG AEROSP SCI,* vol. 39, pp. 467-510, 2003.

[53] Y. Zhang *et al.*, "Experimental investigation into effects of boundary proximity and blockage on horizontal-axis tidal turbine wake," *Ocean Engineering,* vol. 225, 2021.

[54] M. Talavera and F. Shu, "Experimental study of turbulence intensity influence on wind turbine performance and wake recovery in a low-speed wind tunnel," *Renewable Energy,* vol. 109, pp. 363-371, 2017.

[55] D. Medici and P.-H. Alfredsson, "Measurements on a wind turbine wake: 3D effects and bluff body vortex shedding," *Wind Energy,* vol. 9, pp. 219-236, 2006.

[56] J. Wang, D. McLean, F. Campagnolo, T. Yu, and C. Bottasso, "Large-Eddy Simulation of Waked Turbines in a Scaled Wind Farm Facility," *Journal of Physics: Conference Series,* vol. 854, 2017.

[57] X. Yang and F. Sotiropoulos, "A new class of actuator surface models for wind turbines," *Wind Energy,* vol. 21, no. 5, pp. 285-302, 2018.

[58] F. Pierella and L. Sætran, "Wind tunnel investigation on the effect of the turbine tower on wind turbines wake symmetry," *Wind Energy,* vol. 20, pp. 1753-1769, 2017.

[59] A. Crespo, J. Hernandez, E. Fraga, and C. Andreu, "Experimental validation of the UPM computer code to calculate wind turbine wakes and comparison with other models," *Journal of Wind Engineering and Industrial Aerodynamics,* vol. 27, no. 1, pp. 77-88, 1988.

[60] "Particle Image Velocimetry." ScienceDirect. https://www.sciencedirect.com/topics/engineering/particle-image-velocimetry (accessed May 22, 2022).